Jül-4364

Institut für Energie- und Klimaforschung
Nukleare Entsorgung und Reaktorsicherheit (IEK-6)

2nd Annual Workshop Proceedings, 7th EC FP – SKIN

21st – 22nd November 2012
Villigen PSI – Switzerland

JÜLICH
FORSCHUNGSZENTRUM

2nd Annual Workshop Proceedings, 7th EC FP – SKIN

21st – 22nd November 2012
Villigen PSI – Switzerland

Berichte des Forschungszentrums Jülich; 4364

ISSN 0944-2952
Institut für Energie- und Klimaforschung
Nukleare Entsorgung und Reaktorsicherheit (IEK-6)
Jül-4364

Zu beziehen durch:
Forschungszentrum Jülich GmbH
Zentralbibliothek, Verlag
52425 Jülich
Bundesrepublik Deutschland

Tel.: +49 2461 61-5220
Fax: +49 2461 61-6103
E-Mail: zb-publikation@fz-juelich.de

FOREWORD

The present document is the proceedings of the 2nd Annual Workshop of the Euratom FP7 Collaborative Project SKIN (Slow processes in close-to-equilibrium conditions for radionuclides in water/solid systems of relevance to nuclear waste management). The project started in Januaray 2011 and has three years duration. The workshop was hosted by PSI-Ost (Paul Sherrer Institute) and held in Villigen (Switzerland) 21st – 22nd November 2012. Annual workshops bring together, partners, associated group and external interested groups. The present proceedings will be followed by the last proceedings corresponding to the third annual workshop to be held in 2013 in Barcelona (AMPHOS 21, Spain).

The proceedings aim to be available to a broad scientific community on the outcome of the SKIN project through the scientific-technical contributions. The proceedings give information about the project structure and the different activities around the project with the on-going documentation of the project. Exhaustive information about the project can be found under *http://www.emn.fr/z-subatech/skin/index.php/Main_Page*

All the scientific-technical papers submitted have been reviewed for the proceeding by the End-User Group (EUG) the work progress and dissemination strategies in the light of the needs of the IGD-TP strategic research agenda as well as of their national programmes for implementation of geological disposal. EUG is a specific group including members of the *IGD-TP platform*, of waste management and regulators TSO organizations.

Thanks are due to all the authors of the submitted Scientific and Technical papers for review and to the workpackage leaders who provided an overview of the workpackage for the proceedings. We would like to aknowledge especially the reviewers, members of the EUG, who provided comments and recommandations for the papers and for the proceeding. Their active participation to the workshop allows to ensure the progress of the project.

TABLE OF CONTENT

THE PROJECT

SKIN (01/01/2011 – 31/12/2013 - 3 years) is a European Project accepted within the 7th Framework Programme of the European Atomic Energy Community (FP7 Euratom) for nuclear research and training activities. It is a collaborative project including 9 European countries and 1 Asian country: ARMINES/SUBATECH (France), Karlsruhe Institute of Technology (Germany), Forschungszentrum Jülich (Germany), Svensk Kärnbränslehantering AB (Sweden), AMPHOS 21 (Spain), Chalmers University of Technology (Sweden), Stockholm University (Sweden), Paul Scherrer Institute (Switzerland), Loughborough University (United Kingdom) and Peking University (China).

The objective of SKIN is to assess the relevant individual processes in the near-field and far-field to allow the development of robust methodologies for performance and safety assessment. In fact, due to the slow groundwater movement in confined deep geological formations, the system "radionuclides – minerals – engineered barrier materials – water" will be close to chemical equilibrium. These systems, controlling radionuclide mobility, have been studied for many years, but only a little attention has been given to the fact that, due to the long disposal time, individual very slow processes can have a significant impact on the mobility of radionuclides, despite achievement of local equilibrium states being achieved. The results would integrate and complete the FP7 Euratom Programme for the implementation of geological disposal of radioactive waste.

The work program is structured along 4 RTD work packages (WP2-5). They cover near-field and far field aspects to assess the slow processes close-to-equilibrium which results will be implemented in Performance Assessment/Safety Case. Experimental programs are performed in WP2 and WP3: WP2 focuses on the formation and on slow processes close-to-equilibrium of solid solutions in aqueous environments under waste repository near-field and far field aspects as well as cement related systems; WP3 focuses on the understanding of the kinetics of alteration of oxides form primary solids, as well as the secondary solid phases expected to form under repository conditions after the eventual release of the radionuclides present in the different waste. WP4 assesses the experimental results by geochemical thermodynamic modeling and its new partial-equilibrium approach and by the affinity law and its validity close to equilibrium. WP5 performs a synthesis of results of experimental, modeling and safety assessment approaches in the context of a full assessment of the literature, and inclusion of literature data. Specific work packages on knowledge management, education and training (WP6) and administrative management issues (WP1) are also included in the project.

The present proceedings document the outcome of the 2nd Annual Project Workshop and give an overview of the outcome of the two years project.

THE SECOND ANNUAL WORKSHOP

OBJECTIVES

The Workshop combines different activities and meetings with the following objectives:

- Informing about the scientific progress
- Informing about the administrative status
- Discussing various topics of interest
- Informing/agreeing upon forthcoming reportings
- Agreeing upon the forthcoming work program

Emphasis was on scientific-technical topics with administrative issues kept to the minimum necessary.

RTD SESSIONS

Two days of plenary sessions were programmed where the results from the different work packages were presented. Next to an overview of the achievements within the respective WP conducted by the WP leader, scientific highlights were presented. The following presentations were given within the project under the validation by the End User Group. A post-SKIN-workshop GEM-Selecktor v3 code training has been held at PSI-Ost the following day, open to participants (mainly from Swiss universities and research centers) outside the SKIN project.

WP2: Experimental Programme 1: Study of solid-solution formation for selected host solids (carbonates, sulfates, silicates, cements) and radionuclides of interest in the near/far field of a radioactive waste repository

1. J. Hincliff, N. Evans, M. Felipe-Sotelo (LU): *Cement*
2. F. Brandt, M. Klinkenberg, K. Rozov, U. Breuer, D. Bosbach (FZJ): *Sulfates*
3. F. Heberling (KIT): *Carbonates*
4. N. Torapava (CHT) : *Radium-Barium*
5. T. Suzuki (SUBATECH/Armines): *Silicates*

WP3: Experimental Programme 2: Assessment of the kinetics of dissolution of tetravalent oxides under quasi-equilibrium conditions, and the impact of major factors on the rate of retention and release of radionuclides

1. N. Evans, J. Hinchliff (LU): *Tc studies*
2. J. Vandenborre (SUBATECH/Armines):*ThO_2 synthesis and characterization*
3. M. Grivé, E. Colàs and L. Duro (Amphos 21): *Fe(III)-U(VI) EXAFS studies*
4. D. Cui (SU): *The influence of clay slurry invasion on the dissolution of spent nuclear fuel under reductive repository environments*

WP4: Modeling and Theory: Development of a new partial equilibrium approach to geochemical modeling of the slow uptake of radionuclides in host solid solutions, applied to the experimental and literature data

1. B. Thien, D. Kulik, E. Curti (PSI): *Adding uptake kinetics and surface entrapment to geochemical models*
2. E. Curti (PSI): *Modelling Ra uptake in barite*
3. B. Grambow, T. Suzuki, S Ribet (SUBATECH/Armines): *Solubility*

Invited lecture: Prof. B. Fritz, University of Strasbourg: *Geochemical modeling of nucleation and growth of mineral particles in water-rock interaction processes: the code Nanokin*

WP5: Synthesis and Safety Assessment: Overall synthesis of the project results together with previous studies and its impact on the uncertainties for safety assessment

A. Valls, E. Colàs, L. Duro (Amphos 21): *Impact of uncertainties in safety assessment*

WP6: Dissemination activities

1. C. Ekberg (CTH): *Cooperation in education In Nuclear CHemistry*
2. T. Suzuki, L. Duro (SUBATECH/Armines/Amphos 21): *Dissemination*

STRUCTURE OF THE PROCEEDINGS

The proceedings present individual scientific and technical contributions.

WP OVERVIEW

OVERVIEW WP2: CALCITE, BARITE, CLAYS, CEMENT

D. Bosbach
Forschungszentrum Jülich (FZJ)
d.bosbach@fz-juelich.de

Objectives of this WP

WP2 addresses the uptake of radionuclides for selected solid solutions which occur in the near-field, and the far-field as well as cement related systems. The following tasks were studied in detail:

- The applicability of $Ra_xBa_{1-x}SO_4$ solid solution - aqueous solution thermodynamics to a specific scenario: Ra exchange with barite
- Identification of the substitution scheme for complex metal ion substitutions: calcite and selenite
- Identification of metal ion binding - precipitation, co-precipitation, surface uptake - in complex cement related systems
- The reversibility of solid/solution interaction with clays: Cs on illite frayed edges

Five different partners work together within this working package: Karlsruhe Institute of Technology (KIT) works on carbonates. Forschungszentrum Jülich (FZJ), KIT and Chalmers University of Technology (CHT) together work on sulfates. ARMINES works on clays and Loughborough University (LU) on cements.

Summary of reported work

Carbonates (WP2-1):

- Heberling et al. (KIT) *A thermodynamic entrapment model for the description of selenium (IV) coprecipitation with calcite* – Crystal growth experiments were carried out with calcite and selenite. A combination of spectrocscopic methods and theoretical calculations was applied to achieve a comprehensive process understanding of the SeO_3^{2-} uptake by calcite. A new thermodynamic entrapment model was developed providing a framework to understand the Se(IV) coprecipitation with calcite, Se(IV) adsorption at calcite and calcite growth inhibition in the presence of Se(IV).

Sulfates (WP2-2):

- Brandt et al. (FZJ) *Recrystallization of Barite in the presence of Radium* – Recrystallization experiments at close to equilibrium conditons were carried out to investigate the ^{226}Ra uptake by barite. The temporal evolution of the ^{226}Ra concentration was studied at ambient conditions and 90 °C as well as the ^{226}Ra uptake. Detailed SEM and ToF-SIMS investigations were conducted and combined with thermodynamic modeling to unravel the mechanism of ^{226}Ra uptake. A homogeneous uptake of ^{226}Ra into the solid was observed. The highly efficient uptake can be described using a thermodynamic model with a Guggenheim interaction parameter of 0.6 and a solubility product logK($RaSO_4$) of -10.41.

- Torapava et al. (CTH) *Recrystallization of 223-radium with barite* – Combined ^{223}Ra and ^{133}Ba uptake experiments with barite were performed at close to equilibrium conditions. In addition, the coprecipitation of Sr, Ba and ^{223}Ra sulfates was examined with respect to the activation energy of solid solution formation. The activation energies of radium, barium, and strontium sulfates decreases in the order Sr > Ra > Ba which may be correlated to the ionic size of the cation.

Silicates (WP2-3):

- Suzuki-Muresan et al. (Armines) *Effect of temperature on the Dissolution of clayey materials* – The dissolution of clay materials (illite/smectite, illite, Callovo-Oxfordian argillite) has been analyzed at different temperatures to reach conditions close to equilibrium. In addition to the aqueous solution, the solids were characterized. The results presented here include the preparation of the clay mineral phases and of the ^{29}Si radiotracer which will be used during the experiments later on.

Cement (WP2-4):

- Hinchliff et al. (LU): *Diffusion and advection in cementitious media* – Within this WP, experimental methods were developed for the investigation of diffusive and advective transport of radioactive isotopes through cementitious media. In the diffusion experiments the effect of cellulosese degradation products on the mobility of Sr was investigated and an illustration of isotope exchange as a mechanism of Ca migration was described. A new advection experiment was designed and preliminary results for ^{3}H, ^{90}Sr and ^{45}Ca are presented.

OVERVIEW WP3: OXIDES

Lara Duro
AMPHOS 21 (Spain)
lara.duro@amphos21

The global objective of this WP is the assessment of the dissolution processes of oxides of relevance for the safety assessment of the repository in close to equilibrium conditions. To this aim, the following specific investigations were defined from the onset of the projet:

- Study of the nature and long term kinetics of the interaction between actinides and major near field components, linking short-term sorption and long-term coprecipitation processes and their study through specific solid spectroscopy.
- Study of the kinetics of dissolution of tetravalent oxides under conditions close to equilibrium, with special focus on the study of the solid-liquid interface, including monitoring of the composition of the surface through isotopic exchange techniques.
- Study of the effect of near field materials on the kinetics of dissolution of tetravalent oxides and the potential of bentonite colloids as drivers for dissolution enhancement.

6 different partners work within this workpackage: ARMINES, Loughborough University (LU) Stockholm University (SU) and SKB work on the study of the dissolution of tetravalent actinides under quasi equilibrium conditions. To this aim, ARMINES works with ThO_2, LU works with TcO_2, and SU and SKB work with UO_2 and with ThO_2 as a proxy for UO_2 in order to avoid unwanted oxidation of UO_2 to U(VI). Amphos 21, SU and the University of Beijing (PKU) work on the influence of major systems present in the repository on the rate of dissolution of matrix-related material and the retention/release of radionuclides.

In this second annual workshop proceedings, most partners of WP3 have presented a Scientific and Technical contribution showing some of the advances in the results:

- Grivé et al. (Amphos 21) *Interaction between Uranium and Iron(III) oxides*. Coprecipitated U(VI)-Fe(III) solid phases of different aging time have been analysed by means of EXAFS and m-XRF. The conclusions indicate a regrouping of the uranium in the solid forming a schoepite-like structure with time, and also support the role of Iron(III) as seed for the concentration and precipitation of uranyl in the system.

- Vandenborre et al. (ARMINES) *Thorium oxide solubility behavior v. the surface crystalline state*. In this work, the different crystallinity of ThO_2 solid phases obtained by different methods is highlighted. This has an important impact for the solubility process what has been manifested through isotopic exchange experiments.

- Cui et al. (SU and SKB) *On slow UO_2(s) oxidation-dissolution process at different repository conditions*. In this work the results on the study of the dissolution process of

UO_2(s) both under oxidizing and anoxic conditions are shown. The particularity is that, from a combination of methods involving isotopic exchange, the thickness of the surface layer involved in the dissolution process has been estimated.

- Zheng et al. (PKU) *Decomposition of U(VI)-Arsenazo III complex by Fenton reaction induced by Gamma irradiation*. In this contribution the conclusions from the effect of g-radiation on the analyses of U(VI) in the presence of iron and arsenazo(III) are presented and developed. According to the results, irradiation of the system can increase the yield of the Fenton reaction and, thus, the decomposition of Arsenazo(III), what produces changes in the signal of the spectra which are important to consider prior to draw conclusions from the analytical methods.

More detailed development of the work, results and conclusions are shown in the individual contributions and in the periodic reports of the project.

OVERVIEW WP4: THEORY AND MODELLING

Dmitrii A. Kulik
Paul Scherrer Institut (Switzerland)
dmitrii.kulik@psi.ch

Task objectives to date:

4.1. To review existing models of time-dependent trace element uptake in host minerals; To find a generalized approach suitable for implementation in geochemical modelling codes; To perform initial tests of routines implementing the generalized approach in the GEM-Selektor code.

4.2. To collaborate with partners involved in WP2 Task 2.1, in order to interpret experimental data on barite recrystallization kinetics and on the uptake of radium in the barite structure.

4.3. To review the literature data for some typical mineral rates expressed as function of the chemical affinity.

Summary of reported work:

4.1. Chemical thermodynamics alone is usually not sufficient to predict trace element partitioning in host minerals, as evidenced by the growth-rate dependency of trace element partitioning occurring in many water-rock systems like nuclear waste repositories. In this context, three uptake kinetic models were tested and unified for implementation in geochemical modelling codes. The new unified model, tested as a script in the GEM-Selektor code, is also able to predict the effects of variation in solution composition on trace element partitioning. This is not directly possible in the three 'parent' models.

4.2. The experimental data produced at FZJ on Ra uptake during the recrystallization of two commercial barites (Sachtleben and Aldrich) were modelled using a combined kinetic and thermodynamic approach. The evaluation shows two-step kinetics. After a first step (120-180 days) with kinetics similar to that observed in previous experiments, the growth rate increases to values of up to 400 $\mu m\ m^{-2}d^{-1}$. This suggests a sudden nucleation of a new Ra-barite phase. In contrast to previously published experiments, the data indicate formation of solid solutions close to ideality or even with negative interaction parameters. In order to reduce uncertainties in the modelling, a review of published data on the solubility product of $RaSO_4$ has been carried out. The review shows that the currently used value is sufficiently precise and accurate ($\log K^0_{sp}=-10.26 \pm 0.1$).

S+T CONTRIBUTIONS

A THERMODYNAMIC ENTRAPMENT MODEL FOR THE DESCRIPTION OF SELENIUM(IV) COPRECIPITATION WITH CALCITE

Frank Heberling[1*], Victor Vinograd[2], Robert Polly[1], Stephanie Heck[1], Jörg Rothe[1]

[1] Institute for Nuclear Waste Disposal- Karlsruhe Institute of Technology (FRG)

[2] Institute of Energy and Climate Research (IEK – 6) Nuclear Waste Management and Reactor Safety, Forschungszentrum Jülich (GER)

* Corresponding author: Frank.Heberling@kit.edu

Abstract

Selenium is on the one hand an essential nutrient for animals and humans. On the other hand, above certain concentration limits it is toxic. In the context of nuclear waste disposal, the radioisotope ^{79}Se is of special concern due to its long half live ($1.1 \cdot 10^6$ a) and the expected high mobility. Due to the high reactivity of its surface and its tendency to tolerate considerable variation in its chemical composition, calcite is often considered as a mineral phase with a high potential for the sequestration of toxic metals.

Here we present the experimental part of a joint experimental and theoretical study, investigating the incorporation of selenite ($Se(IV)O_3^{2-}$) into calcite. The structural environment of selenite in calcite is studied by means of polarization dependent EXAFS spectroscopy. Results confirm that selenite is structurally incorporated into calcite. Quantitative results from coprecipitation experiments indicate a considerable incorporation of selenite into calcite, at a constant partition coefficient, $D = 0.015 \pm 0.013$, over a large range of selenite concentration. This result is opposed to atomistic calculations on the stability of selenite doped calcite, which predict that the incorporation of selenite into calcite should be very unlikely, $D = 2.7 \cdot 10^{-9}$. These contradictory results in combination with calculations on the stability of selenite incorporated into the calcite surface, growth rates from coprecipitation experiments, adsorption experiments, and literature data, lead us to the formulation of a thermodynamic entrapment model.

According to this model concept selenite may be incorporated spontaneously into the calcite surface monolayer, forming a surface solid solution, characterized by the stability of a hypothetical surface endmember. For this surface solid solution to be overgrown, i.e. for the surface solid solution to be transformed into a energetically much less favourable bulk solid solution, an energy barrier (entrapment energy) must be overcompensated by the driving force for solid solution growth – supersaturation.

Introduction

Selenium is on the one hand an essential nutrient for animals and humans. On the other hand above certain concentration limits it becomes toxic. In the context of nuclear waste disposal, the radioisotope ^{79}Se is of special concern due to its long half live ($1.1 \cdot 10^6$ a (Jiang et al. 1997)) and the expected high mobility. It is created in nuclear reactors by the fission of ^{235}U. E.g. the Belgian nuclear waste management organization ONDRAF/NIRAS comes to the conclusion that ^{79}Se is a potentially critical radionuclide that might within a relevant timeframe (10^4 – 10^5 a) diffuse through the geological barrier (Boom Clay) and increase the radiotoxicity in adjacent aquifers ***(Ondraf/Niras 2001)***.

Sorption reactions with surrounding mineral phases may have an essential impact on the mobility and bioavailability of the oxidized selenium species in soils and sediments. Numerous sorption mechanisms have been observed and characterized on a molecular scale within the past decades. Besides the pure surface reactions: outer-sphere and inner-sphere adsorption, or ion exchange, especially structural incorporation into mineral phases as a consequence of coprecipitation or recrystallization (dissolution/reprecipitation) has a big potential to immobilize toxic trace elements, such as selenium, in soils and aquifers.

Calcite is the most common polymorph of calcium carbonate and the thermodynamically most stable at standard conditions (room temperature and atmospheric pressure). It is abundant in many environmental settings and plays a key role in controlling the geochemical milieu (pH, alkalinity) of soils and ground water. In the surroundings of potential nuclear waste disposals calcite is e.g. present as a mineral constituent in clay formations (up to 20 % in some cases), as fracture filling material in granitic rocks, or as a corrosion product of concrete based materials in the technical barrier. Due to the high reactivity of its surface and its tendency to tolerate considerable variation in its chemical composition, calcite has often been considered as a mineral phase with a high potential for the sequestration of toxic metals. Wang and Liu (2005) ***(Wang and Liu 2005)*** could show that calcite has significant impact on the mobility of selenium in soils.

Cowan et al. (1990) ***(Cowan et al. 1990)*** published an investigation of selenite adsorption at calcite. They found decreasing adsorption with increasing pH in the pH range from 7 to 9. They propose a thermodynamic model for selenite adsorption at calcite based on surface ion-exchange reactions. The assumption of a surface ion-exchange mechanism for selenite sorption at calcite was confirmed by an x-ray standing wave study ***(Cheng et al. 1997)***.

Recent studies showed that upon coprecipitation with calcite from highly supersaturated solutions (0.5 M Ca^{2+} and CO_3^{2-}) ***(Aurelio et al. 2010)*** and at elevated temperatures and pressures (30–90 °C, 25–90 bar) ***(Montes-Hernandez et al. 2011)*** selenite can be incorporated into calcite. Results from EXAFS Se K-edge spectroscopy and Neutron scattering experiments are used in these studies to characterize the structural environment of selenite in calcite and the influence of selenite incorporation on the calcite lattice. The authors present a DFT based theoretical investigation of the structural environment of selenite in calcite. Based

on these results it is proposed that selenite substitutes carbonate in the calcite structure ***(Aurelio et al. 2010)***.

In the study presented here the structural incorporation of selenite into calcite is investigated. Coprecipitation experiments at room temperature are used to prepare selenite doped calcite samples. The structural environment of selenite in calcite is characterized using on the one hand Se-K-edge EXAFS spectroscopy measured on selenite doped calcite powder and on the other hand polarization dependent Se-K-edge EXAFS measured on a selenite doped calcite single crystal.

Selenite incorporation into calcite is quantified at various selenite concentrations (10^{-12} M to 10^{-3} M) at surface controlled growth conditions (Mixed Flow Reactor (MFR) experiments at low supersaturation) and at various calcite supersaturation conditions (SI[1](calcite): 0 – 0.9). Experimental results are compared to DFT-single defect calculations ***(Vinograd et al. 2009; Kulik et al. 2010)*** on Se(IV) incorporation into calcite. As a conclusion a thermodynamic entrapment model, capable of describing selenite coprecipitation with calcite, is presented.

1. Experimental Details

1.1 Synthesis of Se(IV) doped calcite

Various methods are applied in order to investigate Se(IV) incorporation into calcite over a range of Se(IV) concentrations and calcite supersaturation, expressed as SI(calcite).

1.1.1 SI = 0, Adsorption experiments

Adsorption experiments are performed in solutions in equilibrium with calcite and atmospheric CO_2, at three different pH values 7.5, 8.3 and 9.6. The initial Se(IV) concentration are $3.4 \cdot 10^{-13}$ mol/L. The radioisotope ^{75}Se is used for the experiments and concentrations are measured using gamma-counting.

1.1.2 SI = 0.14, Aragonite recrystallization

Synthetic Aragonite is contacted with 0.1 mM Se(IV) solution. Due to the higher solubility of aragonite compared to calcite ($\log_{10}$(K(aragonite))= -8.34, $\log_{10}$(K(calcite))= -8.48), aragonite is expected to dissolve and calcite should precipitate at SI(calcite) = 0.l4. The progress of the reaction is monitored by powder x-ray diffraction of the solid. The reaction rate of the experiment in the presence of Se(IV) is compared to an experiment without Se(IV).

[1] Saturation index, e.g. SI(calcite) = $\log_{10}(a(Ca^{2+}) \cdot a(CO_3^{2-}) / K_{SP}(\text{calcite}))$.

1.1.3 SI = 0.5-0.9, Mixed-Flow-Reactor (MFR) experiments

To investigate Se(IV) coprecipitation with calcite at a range of Se(IV) concentrations (10^{-13} – 10^{-4} mol/L) at surface controlled growth conditions MFR experiments are applied. Ca^{2+}, CO_3^{2-}, and SeO_3^{2-} are fed into the MFR from three independent feeding solutions. In the MFR seed crystals are provided as a substrate for calcite growth. Partition coefficients and growth rates can be derived from balance calculations between inlet and outlet concentrations. Spikes of ^{75}Se are added to the SeO_3^{2-} feeding solution and Se concentrations are measured by gamma counting. Ca^{2+} concentrations are analyzed by ICP-OES.

1.2 EXAFS investigations

EXAFS measurements are performed at the INE-Beamline for Actinide Research at ANKA the synchrotron radiation source at KIT, at the Se-K-edge at 12.664 keV. A powder sample form an non-radioactive MFR experiment and a Se(IV) doped calcite single crystal have been investigated. The single crystal sample was prepared by immersing a (104) terminated calcite single crystal into a supersaturated (SI(calcite) ~1), 1 mM Se(IV) containing solution. The decrease in supersaturation during the reaction time indicates, that a ~1 µm thick calcite layer precipitated onto the crystal surface. The single crystal sample is used for polarization dependent EXAFS measurements with the polarization vector pointing in three different directions along the (104) surface, the crystallographic [010] (bpa), [43-1] (bpb), and [46-1] (bpk) directions. The polarization dependent measurements can be used to obtain additional information about the orientation of the SeO_3^{2-} molecule relative to the calcite lattice ***(Schlegel et al. 1999; Denecke et al. 2005)***.

1.3 Single Defect Calculations

Single defect DFT calculations are performed with CASTEP using GGW/WC potentials. A second DFT calculation used to estimate the stability of the $CaSeO_3$ surface endmember was performed with VASP. As DFT calculations are performed by Victor Vinograd and Robert Polly who are not part of the SKIN project, details about the theoretical methods will not be described here, but in a common publication, which is currently in preparation.

2. Results and Discussion

EXAFS data and model curves are depicted in Figure 26. The observed polarization effect, the variation in the backscattering amplitude, clearly confirms that the orientation of the SeO_3^{2-} molecule is in the planes of the carbonate molecules in calcite. Bond distances and coordination numbers (Table 4) are well in line with the incorporation of SeO_3^{2-} at a slightly strained carbonate site, and are in perfect agreement with literature values ***(Aurelio et al. 2010)*** and with the structure derived from DFT calculations. This leads to the conclusion that SeO_3^{2-} substitutes CO_3^{2-} in the calcite structure and forms a solid solution:

$Ca(SeO_3)_X(CO_3)_{(1-X)}$.

Based on this stoichiometry a thermodynamic partition coefficient can be formulated:

$D = X(CaSeO_3) / X(calcite) \cdot c(CO_3^{2-}) / c(SeO_3^{2-})$,

where X is the mole fraction of either endmember in the solid and c are aqueous concentrations. All these quantities can be obtained from coprecipitation experiments. Results from MFR experiments are depicted in as red diamonds in Figure 27. From the slope of the linear regression we derive an average partition coefficient $D = 0.015 \pm 0.013$ ($R^2 = 0.9998$). The fact that the partition coefficient appears to be constant over the entire concentration range investigated indicates, that the system is best described as an ideal solid solution between calcite and a hypothetical $CaSeO_3$ endmember, which would be suspected to be a $CaSeO_3$ phase in calcite structure. Such a phase does not exist.

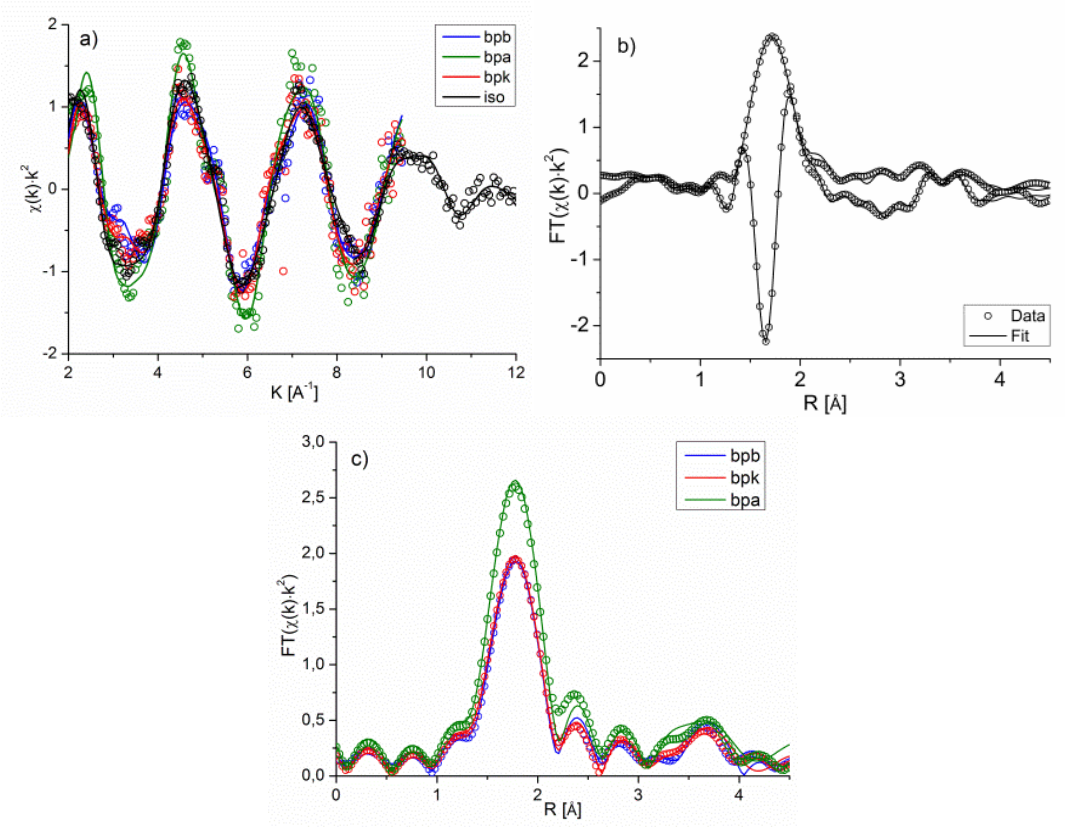

Figure 26: *EXAFS data. Figure 26a) shows the k^2-weighted EXAFS data (circles) and the corresponding model curves (lines) from isotropic (black) and the polarization dependent (blue, green, red) measurements. Fourier transformed EXAFS data (circles) and modeling results (lines) are shown in Figures b) and c). Figure 26b) shows the Fourier transform magnitude and imaginary part of the isotropic data, while Figure 26c) shows the Fourier transform magnitudes of the polarization dependent data. For reasons of clarity the imaginary parts are not depicted.*

For ideal solid solutions the thermodynamic partition coefficient is equal to the ratio of the solubility products (K_{SP}) of the endmember phases:

$D_{ideal}(Ca(SeO_3)_X(CO_3)_{(1-X)}) = K_{SP}(calcite) / K_{SP}(CaSeO_3)$.

This relation can be used to estimate the apparent solubility product of the hypothetical endmember phase: $\log_{10}(K_{SP}(CaSeO_3)_{exp}) = -6.65 \pm 0.5$.

Table 4: *Results from EXAFS data modeling: Bond distances, R, Debye Waller factors, σ^2, coordination number obtained from modeling the isotropic data, Niso, and effective coordination numbers obtained from the polarization dependent data, N_{eff}.*

	isotropic /powder			polarization dependent / single crystal				
shell	R [Å]	σ^2 [Å^2]	N_{iso}	R [Å]	σ^2 [Å^2]	N_{eff}(bpa)	N_{eff}(bpb)	N_{eff}(bpk)
O-SeO_3	1.68 ±0.01	0.001 ±0.001	3.0±0.1	1.68 ±0.01	0.001 ±0.001	3.8±0.2	2.9±0.2	3.1±0.4
O-CO_3	2.88 ±0.02	0.013 ±0.006	3.1±0.7	2.88 ±0.02	0.008 ±0.003	1.9±0.6	3.2±0.6	3.1±1.1
Ca1	3.26 ±0.02	0.010 ±0.003	2.7±0.7	3.26 ±0.02	0.012 ±0.002	3.6±0.8	2.7±0.7	3.3±1.4
Ca2	3.50 ±0.03	0.009 ±0.003	2.6±0.8	3.46 ±0.02	0.008 ±0.002	3.0±0.7	2.8±0.6	2.5±1.3

uncertainties are standard deviations calculated by the ARTEMIS ***(Ravel and Newville 2005)*** *software.*

Theoretically the solubility of the hypothetical phase should be higher than that of any existing $CaSeO_3$ phase. Unfortunately literature values for the solubility of $CaSeO_3 \cdot H_2O$, most likely the relevant $CaSeO_3$ phase to precipitate from aqueous solution at room temperature ***(Olin et al. 2005)***, show a tremendous variation. In their review on the chemical thermodynamics of selenium Olin et al. 2005 deal with that by assigning it: $\log_{10}(K_{SP}(CaSeO_3 \cdot H_2O)) = -6.40 \pm 0.25$, which is within uncertainty the same as what we find for the hypothetical $CaSeO_3$ endmember.

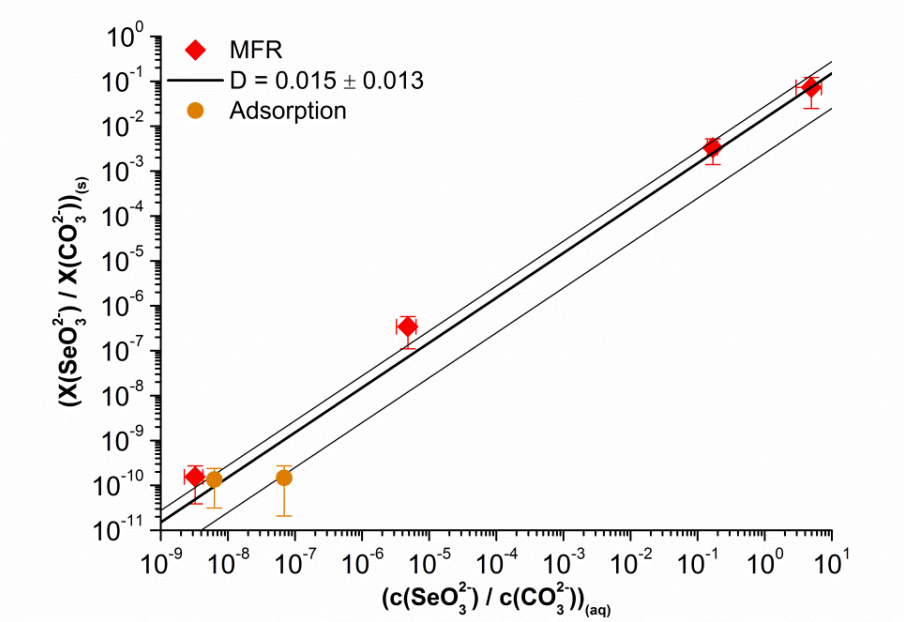

Figure 27: *SeO_3^{2-} to carbonate ratio in the solid, plotted against the SeO_3^{2-} to carbonate ratio in the solution phase. The trend in the MFR data indicates a constant partition coefficient over the entire concentration range. The adsorption experiment at calcite equilibrium shows the same result. To calculate the SeO_3^{2-} to carbonate ratio in the solid for the adsorption experiment, the formation of a single monolayer solid solution has been assumed.*

Nevertheless, the stability of the hypothetical $CaSeO_3$ endmember is much higher than expected. Single defect DFT calculations show, that the relaxation of the calcite structure around the incorporated selenite molecule is enough to destabilize the structure. This destabilisation is expressed in a theoretically derived solubility product for the hypothetical bulk $CaSeO_3$ endmember of: $\log_{10}(K_{SP}(CaSeO_3)_{bulk}) = 0.09$. Theoretically this solubility product should be used to describe the incorporation of SeO_3^{2-} into the bulk calcite structure. The corresponding partition coefficient, $D = 2.7 \cdot 10^{-9}$, is orders of magnitude lower than the measured partition coefficient.

As a first approach it was tested if the discrepancy between theory and experiment can be assigned to the effect that theory assumes real thermodynamic equilibrium, while in coprecipitation experiments supersaturated conditions are applied. This was tested by applying a simple kinetic model which considers the dependency of the partition coefficient on supersaturation ***(Shtukenberg et al. 2006)***, but this approach clearly failed.

Much more promising results are obtained if we assume an intermediate surface solid solution state, which is characterized by the solubility product of a hypothetical surface $CaSeO_3$ endmember. This surface endmember can be imagined as a (104) terminated calcite, covered by a monolayer of $CaSeO_3$. The solubility product of this surface endmember defines how much SeO_3^{2-} can be incorporated into the calcite surface monolayer. Upon coprecipitation this

surface layer can be entrapped and converted into a bulk solid solution. The thermodynamic properties of this bulk solid solution are characterized by the solubility product of the hypothetical bulk $CaSeO_3$ endmember of: $\log_{10}(K_{SP}(CaSeO_3)_{theo\_bulk}) = 0.09$. This bulk solid solution has the same composition as the surface solid solution it originates from. Therefore it is not in equilibrium with the aqueous solution composition, but as it has no direct contact with the solution phase and cannot react with the solution unless through the surface. The disequilibrium cannot cause any reaction. The unstable bulk solid solution is entrapped underneath the stable surface solid solution.

We call this concept thermodynamic entrapment model, as it describes an entrapment process, but it is not primarily kinetically driven. Instead it is based on the difference in the thermodynamic stability of the surface solid solution phase and the bulk solid solution phase.

If we try to estimate the solubility product of the hypothetical $CaSeO_3$ surface endmember from DFT calculations we get values between $\log_{10}(K_{SP}(CaSeO_3)_{theo\_surf}) = -3.74$ and $\log_{10}(K_{SP}(CaSeO_3)_{theo\_surf}) = -8.23$. Values which are right around the experimentally derived apparent solubility product of the surface endmember $\log_{10}(K_{SP}(CaSeO_3)_{exp}) = -6.65 \pm 0.5$. Most of the spread in the theoretical values depends on, if surface hydration is considered in the calculation or not. Other sources of uncertainty are the values for the stability of the reference $CaSeO_3$ phase, or how to deal with subtracting the contribution from surface free energy. But in any case DFT calculations show the right trend: the incorporation of SeO_3^{2-} into the calcite surface is energetically much more favorable than the incorporation into the bulk calcite structure. Considering the pyramidal geometry and the larger size of the SeO_3^{2-} molecule, as compared to the planar geometry of carbonate, this is easily comprehensible.

An interesting effect of the proposed entrapment model is related to the model consequence, that a certain energy is required for the conversion of the surface solid solution into a bulk solid solution. This entrapment energy can easily be calculated. The Gibbs' free energy of the endmember phases is related to the corresponding solubility products by:

$$\Delta G(endmember) = RT \ln(K_{SP}(endmember)) + \Sigma_i \Delta G_i,$$

where ΔG_i would denote the Gibbs free energies of the 'i' aqueous ions the endmember is composed of, while R and T are the universal gas constant and the absolute temperature, respectively. If we use the experimentally derived solubility product for the hypothetical $CaSeO_3$ endmember as the solubility product of the $CaSeO_3$ surface endmember, the ΔG values for all relevant endmembers are:

$\Delta G(calcite) = -1129.08$ kJ/mol

$\Delta G(CaSeO_{3\_surface}) = -955.5$ kJ/mol

$\Delta G(CaSeO_{3\_bulk}) = -914.7$ kJ/mol

ΔG of the ideal solid solution $Ca(SeO_3)_X(CO_3)_{(1-X)}$ for a given X is simply:

$\Delta G(Ca(SeO_3)_X(CO_3)_{(1-X)}) = X\ \Delta G(CaSeO_3) + (1-X)\ \Delta G(calcite)$.

To calculate the entrapment energy, ΔG_e, we subtract for one given composition X the free energy of the surface solid solution from that of the bulk solid solution, and get:

$\Delta G_e = X\ \Delta G(CaSeO_{3\_bulk}) - X\ \Delta G(CaSeO_{3\_surface})$

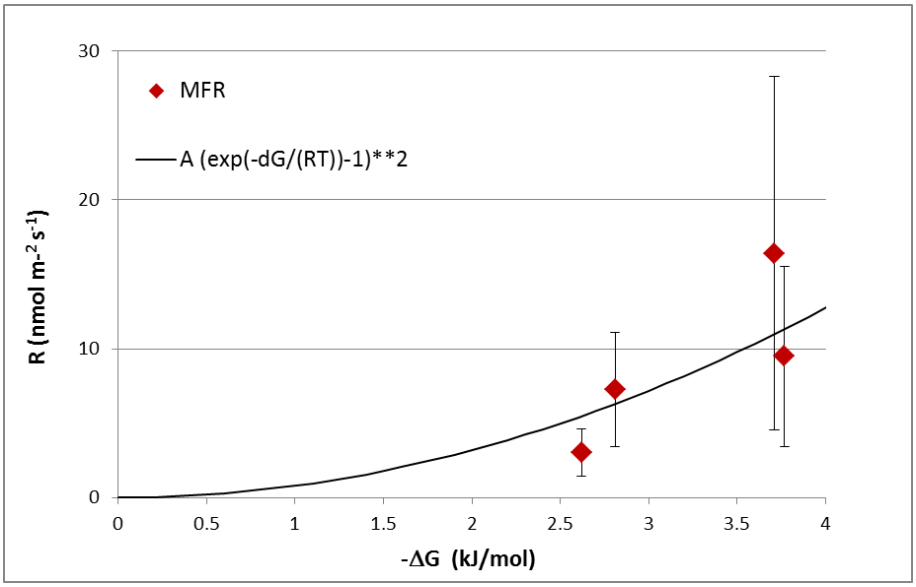

Figure 28: *MFR growth rates plotted as a function of –ΔG.*

This entrapment energy represents an energy barrier, which has to be overcome in order to enable solid solution growth. Opposed to this, the supersaturation is the driving force for solid solution growth. A ΔG_s value related to supersaturation, S, can be calculated from:

$\Delta G_s = RT \ln S$.

S in the case of a solid solution can be calculated from the total solubility product.

$S = [a(Ca^{2+})\ (a(CO_3^{2-})+a(SeO_3^{2-}))] / [(1-X)\ K_{SP}(calcite) + X\ K_{SP}(CaSeO_{3\_surf})]$

The remaining driving force for solid solution growth can now be calculated as:

$\Delta G = \Delta G_s + \Delta G_e$

Plotting the growth rates measured in MFR experiments against experimental –ΔG values (Figure 28) shows that ΔG is indeed a likely candidate for the driving force for solid solution growth in SeO_3^{2-} coprecipitation experiments. The black line in Figure 28 is an empirical fit to the data points which corresponds to the assumption that growth rates are proportional to $(S-1)^2$, as it is usually assumed for spiral growth processes ***(Mullin 2001)***. Only that S in this case is corrected for entrapment energy, which means it is calculated as:

$S = \exp(-(\Delta G_s + \Delta G_e)/(RT))$.

The concept of entrapment energy is also supported by the results from the aragonite recrystallization experiment. In this experiment the supersaturation with respect to calcite is very low (SI(calcite) = 0.14) and the SeO_3^{2-} concentration is relatively high: 10^{-4} mol/L. This leads to a situation where, according to the entrapment model, the surface solid solution contains 2.6 % (mol) SeO_3^{2-}, the supersaturation with respect to the solid solution is S = 1.43 (ΔG_s = -0.881 kJ/mol), and the entrapment energy is, ΔG_e = 0.996 kJ/mol. Accordingly, $\Delta G > 0$, and no solid solution growth should be possible.

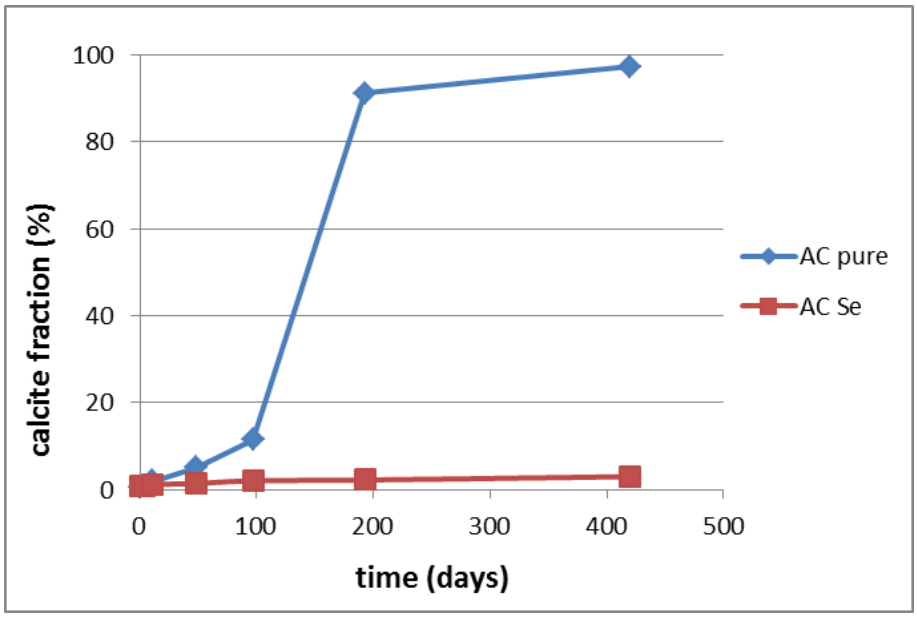

Figure 29: *While in the pure system aragonite recrystallizes over 420 days and forms the thermodynamically more stable calcite, in the SeO_3^{2-} containing system calcite growth is inhibited.*

The corresponding data are shown in Figure 29. They clearly show that in the selenite free system (blue diamonds) aragonite dissolves as expected over the experimental period of 420 days in favour of precipitation of the thermodynamically more stable calcite, while in the selenite containing system (red squares) the formation of calcite is inhibited and aragonite persists.

More experimental support for the thermodynamic entrapment concept comes from adsorption experiments. For calcite in a solution in equilibrium with calcite and in the presence of SeO_3^{2-}, it would be expected that at the calcite surface the topmost monolayer recrystallizes and forms an $Ca(SeO_3)_X(CO_3)_{(1-X)}$ surface solid solution. Bulk recrystallization is not expected. Regarding the resulting structure, the formation of a surface solid solution is

equivalent to ion exchange, which was the adsorption process for SeO_3^{2-} at calcite originally proposed by ***(Cowan et al. 1990)*** in their adsorption study, and later confirmed by ***(Cheng et al. 1997)*** by x-ray standing wave measurements. Correspondingly, the results from adsorption experiments (SI(calcite) = 0) can be expressed as a partition coefficient for the surface monolayer solid solution. Experimental results at pH 8.3 and pH 7.5 (cp. Section 1.1.1) i.e. the corresponding solution and surface monolayer compositions, are depicted as orange circles in Figure 27. The pH values during the adsorption experiments, 7.5 and 8.3, are close to those during MFR experiments, $7.6 < pH < 8.0$. The surface composition during adsorption experiments coincides surprisingly well with the partition coefficient derived from MFR experiments. For the adsorption experiment at pH 9.6 no adsorption was observed. This indicates that for the coprecipitation a similar pH dependency might be expected.

Conclusions and future work

The thermodynamic entrapment model provides a framework to comprehend Se(IV) coprecipitation with calcite, Se(IV) adsorption at calcite, and calcite growth inhibition in the presence of Se(IV). It is in agreement with previous literature about Se(IV) interactions with calcite ***(Cowan et al. 1990; Cheng et al. 1997; Aurelio et al. 2010)*** and its basic assumptions are supported by EXAFS spectroscopy and DFT calculations.

Consequences of the model for nuclear waste disposal are that at calcite equilibrium Se(IV) is expected to react with the calcite surface only. Incorporation into bulk calcite by spontaneous recrystallization, which would be the most effective retardation mechanism, is according to the model not possible. In order to incorporate Se(IV) into the bulk calcite structure, Se(IV) needs to be coprecipitated with growing calcite at a supersaturation, high enough to overcompensate entrapment energy, a process which may only be expected at some special locations in the barrier system around a nuclear waste disposal.

The next step in this study will be the publication of the experiments, DFT calculations, and the model concept.

Many ideas are around for future experimental and theoretical work, capable of testing the model concept and refining the thermodynamic parameters, including AFM-, surface diffraction-, and crystal growth experiments, but no decision is made yet, which will be the next step.

Acknowledgement

The research leading to these results has received funding from the European Union's European Atomic Energy Community's (Euratom) Seventh Framework Program FP7-Fission-2010 under grant agreement number 269688 (CP-SKIN).

References

Aurelio, G., A. Fernandez-Martinez, G. J. Cuello, G. Roman-Ross, I. Alliot and L. Charlet (2010). "Structural study of selenium(IV) substitutions in calcite." Chemical Geology **270**(1-4): 249-256.

Cheng, L. W., P. F. Lyman, N. C. Sturchio and M. J. Bedzyk (1997). "X-ray standing wave investigation of the surface structure of selenite anions adsorbed on calcite." Surface Science **382**(1-3): L690-L695.

Cowan, C. E., J. M. Zachara and C. T. Resch (1990). "Solution ion effects on the surface exchange of selenite on calcite." Geochimica et Cosmochimica Acta **54**(8): 2223-2234.

Denecke, M. A., D. Bosbach, K. Dardenne, P. Lindqvist-Reis, J. Rothe and R. Z. Yin (2005). "Polarization dependent grazing incidence (GI)XAFS measurements of uranyl cation sorption onto mineral surfaces." Physica Scripta **T115**: 877-881.

Jiang, S. S., J. R. Guo, S. Jiang, C. S. Li, A. Z. Cui, M. He, S. Y. Wu and S. L. Li (1997). "Determination of the half-life of Se-79 with the accelerator mass spectrometry technique." Nuclear Instruments & Methods in Physics Research Section B-Beam Interactions with Materials and Atoms **123**(1-4): 405-409.

Kulik, D. A., V. L. Vinograd, N. Paulsen and B. Winkler (2010). "(Ca,Sr)CO(3) aqueous-solid solution systems: From atomistic simulations to thermodynamic modelling." Physics and Chemistry of the Earth **35**(6-8): 217-232.

Montes-Hernandez, G., G. Sarret, R. Hellmann, N. Menguy, D. Testemale, L. Charlet and F. Renard (2011). "Nanostructured calcite precipitated under hydrothermal conditions in the presence of organic and inorganic selenium." Chemical Geology **290**(3-4): 109-120.

Mullin, J. W. (2001). Crystallization. Oxford, Boston, Butterworth Heinemann.

Olin, A., B. Noläng, E. Osadchii, L.-O. Öhman and E. Rosen (2005). Chemical Thermodynamics of Selenium, OECD Nuclear Energy Agency (NEA).

Ondraf/Niras (2001). Technical Overview of the SAFIR 2 Report, Safety Assessment and Feasibility Interim Report 2.

Ravel, B. and M. Newville (2005). "ATHENA, ARTEMIS, HEPHAESTUS: data analysis for X-ray absorption spectroscopy using IFEFFIT." Journal of Synchrotron Radiation **12**: 537-541.

Schlegel, M. L., A. Manceau, D. Chateigner and L. Charlet (1999). "Sorption of metal ions on clay minerals I. Polarized EXAFS evidence for the adsorption of Co on the edges of hectorite particles." Journal of Colloid and Interface Science **215**(1): 140-158.

Shtukenberg, A. G., Y. O. Punin and P. Azimov (2006). "Crystallization kinetics in binary solid solution–aqueous solution systems." American Journal of Science **306**(7): 553-574.

Vinograd, V. L., M. H. F. Sluiter and B. Winkler (2009). "Subsolidus phase relations in the CaCO(3)-MgCO(3) system predicted from the excess enthalpies of supercell structures with single and double defects." Physical Review B **79**(10): 9.

Wang, X. K. and X. P. Liu (2005). "Sorption and desorption of radioselenium on calcareous soil and its solid components studied by batch and column experiments." Applied Radiation and Isotopes **62**(1): 1-9

RECRYSTALLIZATION OF BARITE IN THE PRESENCE OF RADIUM

Felix Brandt[1*], Martina Klinkenberg[1], Konstantin Rozov[1], Uwe Breuer[2], Dirk Bosbach[1]

[1] Institute of Energy and Climate Research (IEK – 6) Nuclear Waste Management and Reactor Safety, Forschungszentrum Jülich (GER)

[2]Central Institute of Engineering, Electronics and Analytics, ZEA-3 Analytics, Forschungszentrum Jülich GmbH

* Corresponding author: f.brandt@fz-juelich.de

Abstract

The ^{226}Ra uptake by barite at ambient conditions and 90 °C was studied in batch experiments with a special focus on the radio-barite recrystallization mechanism, the solid-solution composition and the Ra uptake rate. Recrystallization experiments were carried out for two different types of barite with varying surface area and an initial Ra concentration of $5 \cdot 10^{-6}$ mol/L. The results obtained at ambient conditions show a significant decrease of the Ra concentration in the presence of barite to values between $3 \cdot 10^{-9}$ and $7 \cdot 10^{-9}$ mol/L at 5 g/L of barite and $2 \cdot 10^{-8}$ mol/L at 0.5 g/L of barite. At 90 °C Ra uptake into barite during batch recrystallization experiments is significantly lower than at room temperature, corresponding well with the end-member solubilities at room temperature and 90 °C as calculated with GEMS-PSI. First results of TOF-SIMS analyses using the Sachtleben barite after 443 days from the recrystallization experiments at ambient conditions with 0.5 and 5 g/L show a homogenous distribution of Ra within the recrystallized barite, indicating a full recrystallization.

Introduction

The possible solubility control of Ra by coprecipitation of a $Ra_xBa_{1-x}SO_4$ solid solution has been demonstrated in several cases e.g. ***Doerner & Hoskins, 1925***. However, an open question is whether a Ra containing solution will equilibrate with solid $BaSO_4$ under repository relevant conditions due to barite recrystallization. Here, Ra enters a system in which barite is in equilibrium with the aqueous solution. Previous studies have revealed that uptake of Ra is not limited by pure adsorption at close to equilibrium conditions but involves a significant fraction of the bulk solid ***(Bosbach et al. 2010, Curti et al. 2010)***.

Here we present barite recrystallization experiments in the presence of Ra at ambient conditions and 90 °C. In addition, thermodynamic calculations were carried out to gain a deeper understanding of the Ra - $BaSO_4$ exchange process.

1. Recrystallization experiments

1.1 Experimental setup

Batch recrystallization experiments were performed at ambient conditions (23 ± 2 °C) and at 90 (± 1) °C. The barites were pre-treated for 4 weeks in 10 mL of 0.2 n NaCl solutions in 25 mL glass bottles. Afterwards, 10 mL of a Ra containing solution were added, resulting in a total volume of 20 mL, an ionic strength of 0.1 n NaCl, and a concentration of $5 \cdot 10^{-6}$ mol/L of Ra. The ionic strength was chosen to be comparable to granitic ground waters e.g. at the Äspö site in Sweden. Experiments were carried out with a solid/liquid ratio of 5 g/L and 0.5 g/L. In regular time intervals 500 µL of the aqueous solution were taken and then filtered. The liquid was filtered through Advantec ultrafilters (MWCO = 10,000 Da) and then analyzed for the Ra and Ba concentration.

1.2 Sample preparation and characterization

Two different types of barite powders with varying grain size distribution and morphology were used during the Ra uptake experiments. The first barite was a synthetic, high purity barite (XR-HR10) from Sachtleben Chemie® GmbH, which was provided by Enzo Curti (Paul Scherrer Institute (PSI), Villigen, Switzerland). The same barite was used in the experiments of ***Bosbach et al. (2010)*** and ***Curti et al. (2010)***. The second barite was a commercially available barium sulfate from Aldrich® with a purity of 99.998 %. XRD confirmed that both powders are pure barite within the precision of this method.

A grain size fractionation was carried out via sedimentation using Atterberg cylinders to narrow down the grain size distribution of the two barite types and achieve a homogeneous morphology. A coarse fraction of the Sachtleben barite and a fine fraction of the Aldrich barite were separated. The specific surface area of the separated Sachtleben barite as determined via Kr-BET is S_{BET} = 0.17 m²/g, and differs from the specific surface area of S_{BET} = 0.31 m²/g determined by ***Curti et al. (2010)***, which may be due to the enrichment of coarse particles. The specific surface area of the fine Aldrich barite fraction was determined as S_{BET} = 1.70 m²/g. SEM observations indicated that the Aldrich barite consisted of rounded particles forming agglomerates. The particles showed smooth crystal surfaces with small pores. The mean particle size was < 2 µm (Figure 19 a, b).

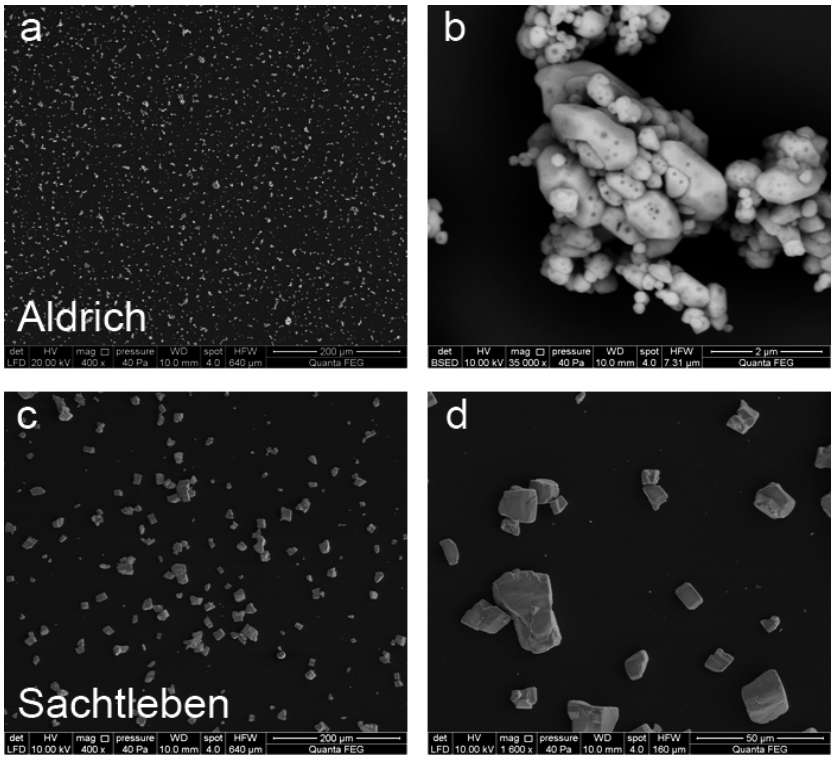

Figure 19: *SEM images of equilibrated Aldrich (a, b) and Sachtleben (c, d) barite. The magnification of the detail images b and d was adjusted to the actual grain size whereas the overview in a and c has identical magnifications.*

The Sachtleben barite consisted of blocky crystals with a particle size of > 10 µm (Figure 19 c, d). The morphology was dominated by barite cleavage planes.

1.3 Analysis of the aqueous solutions

The Ra concentration in solution was examined via Gamma spectrometry using a N_2 cooled high purity (HP) Ge-detector. The Ba concentration in solution was quantified via ICP-MS using an ICP-MS ELAN 6100 DRC (PerkinElmer SCISX) instrument.

1.4 Analysis of the solids

The morphology of the barite crystals was studied using the environmental scanning electron microscope FEI Quanta 200 F. In order to avoid artifacts due to precipitation of NaCl, $BaSO_4$ or $RaSO_4$, the samples were separated from their solution by two washing steps in iso-propanol. The samples were then prepared as a suspension on a Si wafer and subsequently dried.

The spatial distribution of Ra and Ba within the recrystallized barite powders was analyzed using an ION-TOF instrument equipped with a Cs source. The raw data were reconstructed and analyzed using the ION-TOF software package.

2. Modeling of the thermodynamic solid solution – aqueous solution equilibrium

The Lippmann formulation ***(Lippmann, 1980)*** of the solubility product of solid solutions and the graphical representation of this solubility product as a function of solid solution – aqueous solution (SS – AS) compositions has been used. The Lippmann approach allowed formulating the $BaSO_4$ – $RaSO_4$ – H_2O equilibria in terms of activities of dissolved relevant components (Ra^{2+} and Ba^{2+}) which are related to the mole fractions of $BaSO_4$ and $RaSO_4$ in the $(Ba,Ra)SO_4$ solid solution. The Lippmann diagram combines the activities of the dissolved components and the respective mole fractions of the solid solution in equilibrium via the total solubility product

$$\Sigma\Pi = ([Ra^{2+}] + [Ba^{2+}]) \cdot [SO_4^{2-}] \quad (1)$$

with $[Ra^{2+}]$, $[Ba^{2+}]$ and $[SO_4^{2-}]$ = activities of the dissolved components

A comprehensive discussion in which the expressions for the relationship between solid solution compositions and aqueous solution composition are derived can be found e.g in ***Prieto (2009)***. Based on the Lippmann theory, the complete equilibration of a SS – AS system can be calculated, provided that the solubilities of the end - members and the interaction parameters are known. Here, SS - AS equilibrium calculations were carried out for the $BaSO_4$ – $RaSO_4$ – H_2O system with the GEMS – PSI code ***(Kulik et al., 2012, Wagner et al., 2012)*** with the implemented NAGRA – PSI thermodynamic database ***(Hummel et al., 2002)***.

3. Results & Discussion

3.1 Recrystallization at room temperature

The temporal evolution of the Ra and Ba concentrations in solution is shown in Figure 20. In total, seven experiments with 5 g/L of Sachtleben barite were carried out. Mean values and the standard deviation were calculated from replicate experiments and were used for error bars in Figure 20. After one day of experiments, measured concentrations of dissolved Ba were in good agreement with values calculated by GEMS-PSI. This confirms that the experiments with 0.5 g/L were close to equilibrium conditions with the barite end-member. Slightly higher Ba concentrations than expected were observed during the 5 g/L of barite experiments.

The general shape of the c(Ra) vs. time curves is similar in the experiments with 0.5 and 5 g/L of barite, although the Ra decrease is much faster using 5 g/L of barite. Three stages can be observed in the c(Ra) vs. time curves of the 0.5 g/L experiments: (1) slow, but steady decrease up to day 70 of the Sachtleben and day 182 of the Aldrich experiment; (2) strong decrease of up to 2 orders of magnitude of the Ra concentration within 110 days (Sachtleben) to 170 days

(Aldrich); (3) steady state of the Ra concentration at 3 – 5 · 10^{-8} mol/L of Ra, compared to an initial Ra concentration of 5 · 10^{-5} mol/L.

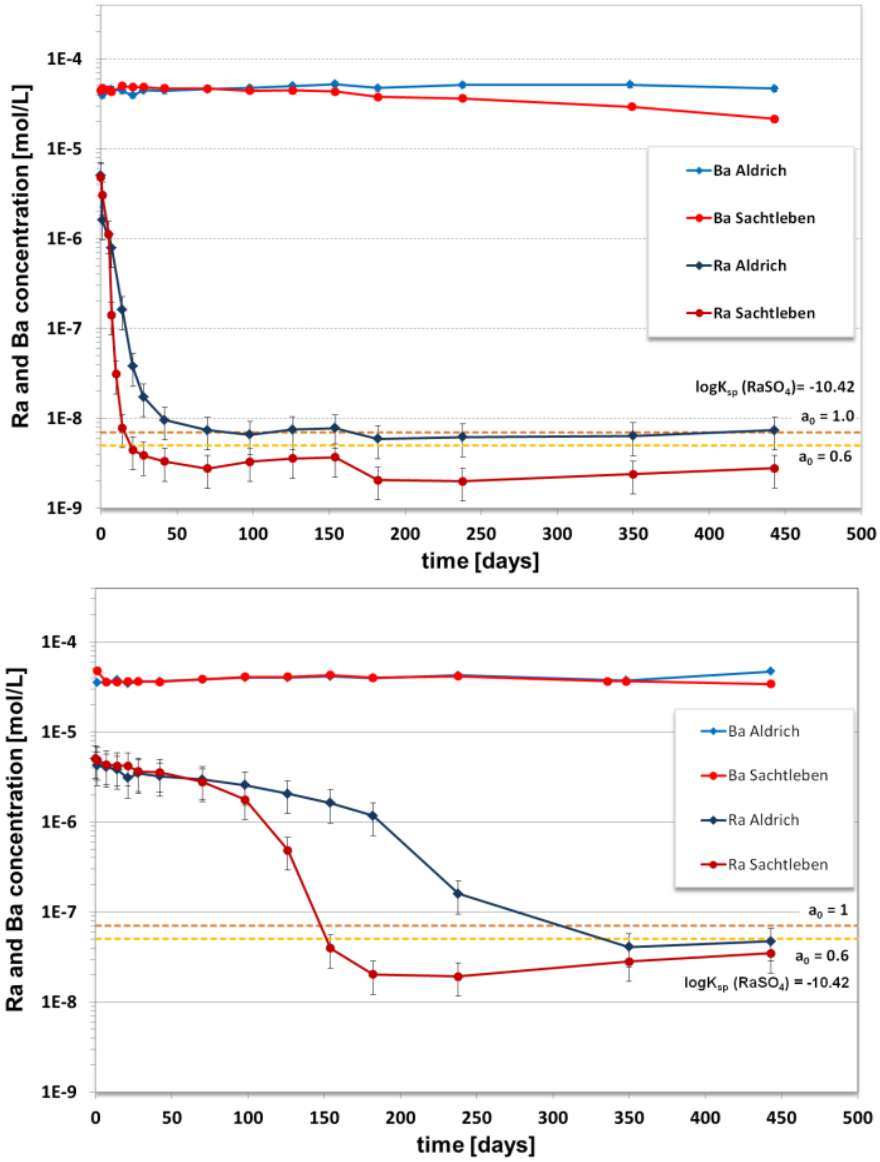

Figure 20: *Temporal evolution of the Ra and Ba concentrations Top: experimental results with 5 g/L of barite; Bottom: results for 0.5 g/L of barite.*

In the experiments with 5 g/L, a first stage of the Ra concentration decrease is observed within the first week for both barites, followed by a decrease of more than two orders of magnitude after 2 weeks for Sachtleben and 5 weeks for the Aldrich barite. The final Ra concentration of Sachtleben (~ 3 · 10^{-9} mol/L) is slightly lower than the final Ra concentration observed for Aldrich (~ 6 · 10^{-9} mol/L), although Aldrich has a significantly higher specific

surface area. Similarly, the final concentration of Ra is slightly lower for the Sachtleben experiment at 0.5 g/L.

The recrystallization was modeled using the GEMS-PSI code combined with the NAGRA-PSI database. However, if the implemented value is used, only negative interaction parameters a_0 would be possible to fit the observed final Radium concentrations. Positive a_0 in combination with a $\log K_{SP}(RaSO_4)$ of -10.26 would predict significantly higher final Ra concentrations than observed in all experiments of this study. In addition, negative a_0 would be in contradiction with a_0 values proposed by ***Zhu (2004)*** and ***Curti et al. (2010)*** and with general trends of the sulfate salts ***(Glynn, 2000, Kiseleva et al., 1994, Plummer et al,. 1987)*** as all these publications suggest positive a_0.

The available solubility products of $RaSO_4$ as published in literature are based on only two experimental studies by ***Nikitin & Tolmatscheff (1933)*** and ***Lind et al. (1918)***. In contrast to $BaSO_4$, for $RaSO_4$ the available data do not provide sufficiently tight constrains on the value of $\log K_{RaSO4}$. The results of ***Paige et al. (1998)*** showed that slight variation in the fitting procedure applied to the same data produced the variation within the range of 10.21 – 10.42 in $\log K_{RaSO4}$ values. A combination of $\log K_{RaSO4} = -10.41$ with a positive a_0 could be used to model the new experimental data.

TOF-SIMS was carried out on a Sachtleben barite sample from the 0.5 g/L experiment taken after 443 days in order to examine the spatial Ra distribution within the recrystallized barite. Figure 21 shows an overlay of the integrated elemental signal of Ba (top) and Ra (bottom) with the complementary electron microscopy image. The integrated Ra concentration corresponds with the size of the barite particles, i.e. all particles contain Ra in similar amounts. A depth profile of the respective Ba and Ra concentrations was reconstructed from the TOF-SIMS data (Figure 21, right). A homogenous Ra concentration distribution was observed for the large barite crystal in the middle of the SEM image (Figure 21, left).

The Ba/Ra ratio was calculated from several TOF-SIMS measurements, using the integrated elemental signals (Figure 22). Mass balance calculations for the Sachtleben barite suggest a mole fraction of $X_{RaSO4(s)} = 2.3 \cdot 10^{-3}$, assuming full recrystallization at the end of the experiment. The Ra/Ba intensity distribution of Figure 22 has its maximum between 2 and $4 \cdot 10^{-3}$, corresponding well with the macroscopic results.

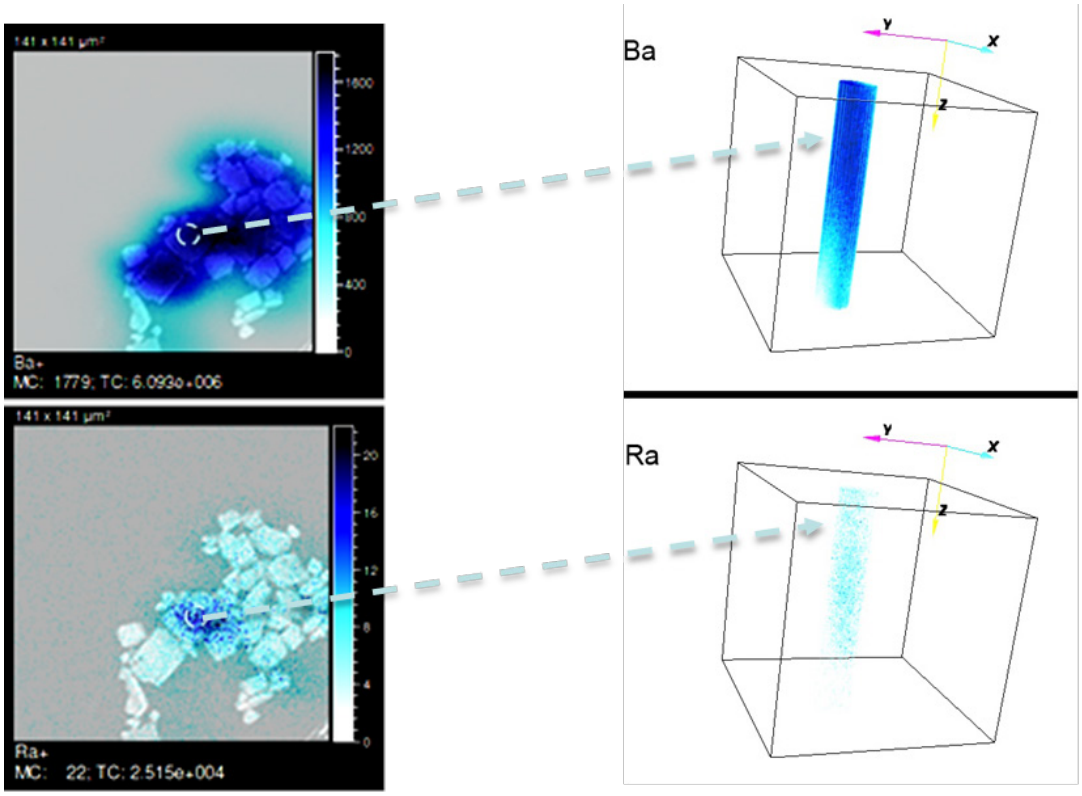

Figure 21: *Left: combined SEM and TOF-SIMS image of barite 1.5 after 350 days of recrystallization. The blue colour indicates the integrated TOF-SIMS signal of the respective element; right: depth profile reconstructed for the indicated X-Y area of the left image.*

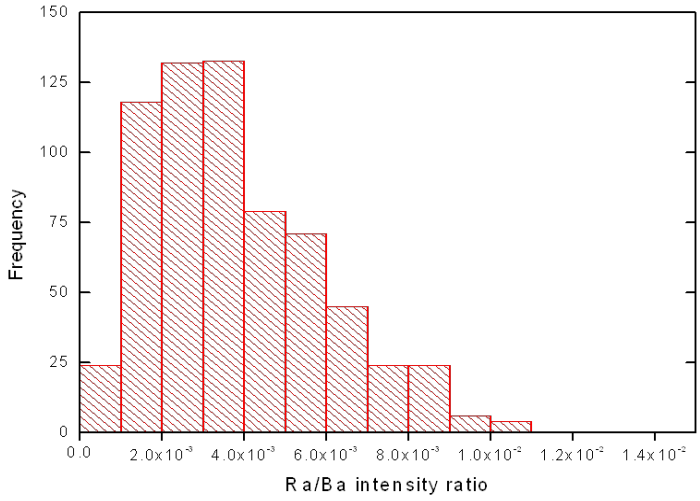

Figure 22: *Evaluation of Ra/Ba intensities as calculated from the TOF-SIMS measurements of sample 1.5 after 350 days of recrystallization. The calculated Ra/Ba based on mass balance is 2.3 . 10-3.*

3.2 Recrystallization at 90 °C

Lippmann diagrams calculated with GEMS-PSI using the Nagra-PSI database, show that $RaSO_4$ is less soluble than $BaSO_4$ at room temperature (RT) whereas at 90 °C $RaSO_4$ is more soluble (Figure 23). Consequently, based on the shapes and respective positions of the solidus and solutus curves at room temperature (RT) and at 90 °C, a lower uptake of Ra during barite recrystallization at higher temperatures can be expected. This is confirmed by the experimental results of experiments with 5 g/L of the respective barites at 90 °C (Figure 23, right) which show a higher final Ra concentration of ~ $1 \cdot 10^{-8}$ mol/L compared to 3 to $6 \cdot 10^{-9}$ mol/L for RT. In contrast to the experiments at RT, the final Ra concentration is lower when Aldrich barite is in contact with the Ra solution. Compared to RT, much faster reaction kinetics are observed, i.e. the plateau is reached already after 7 to 15 days in experiments using 5 g/L of initial barite. The Ba concentration is again in good agreement with the barite end - member solubility already in early phases of the recrystallization experiment.

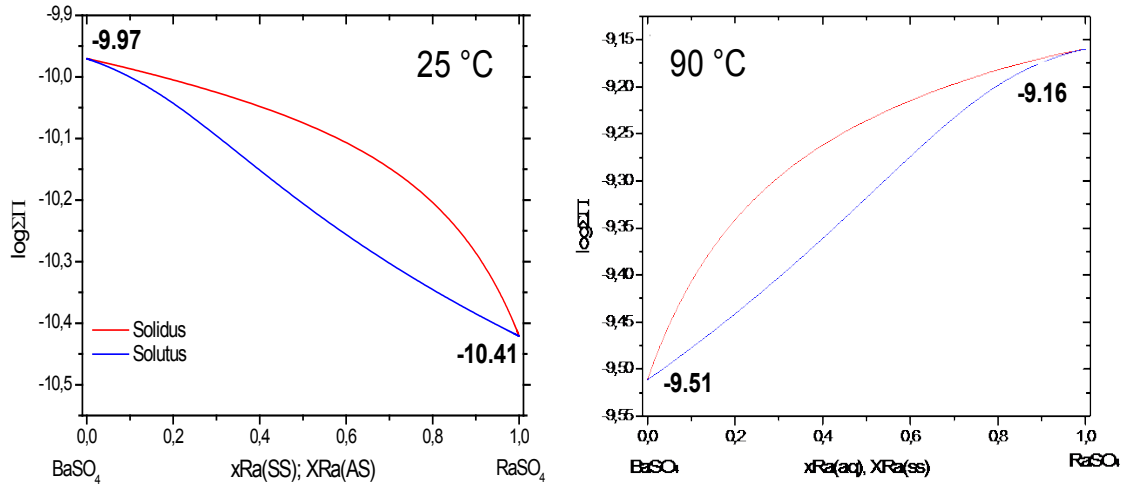

Figure 23: *Lippmann diagrams for 25 °C and 90 °C (a_0 = 0.6 at RT and recalculated for 90°C), calculated GEMS-PSI program code using the indicated solubility products.*

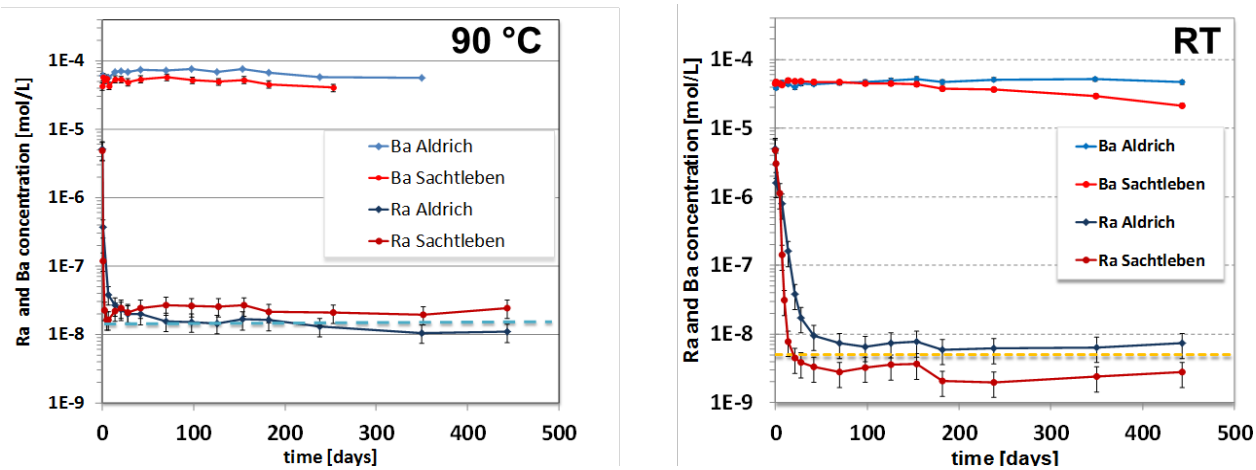

Figure 24: *Comparison of temporal evolution of the Ra and Ba concentrations. Left: experimental results obtained with 5 g/L of barite at 90°C; right: experimental results obtained with 5 g/L of barite at room temperature.*

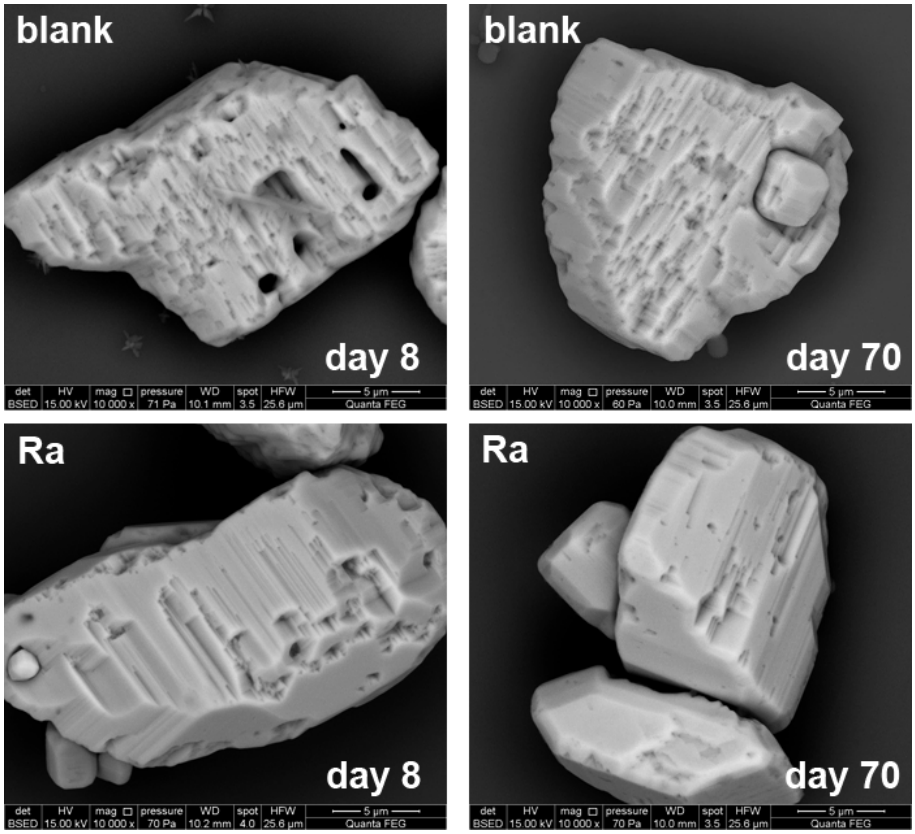

Figure 25: *Barite grains from a blank experiment at 90 °C (top) and Ra recrystallization experiment (bottom); left images were taken after day 8 and right images after day 70.*

Samples of a 5 g/L Sachtleben blank experiment at 90 °C without Ra were compared with samples taken from the Ra uptake experiments taken at similar times. Figure 25 shows that blank and Ra experiment have a similar morphology at the early stages of the experiments (left images); however, already after day 8 the typical crystal surfaces of the barites in contact with Ra solution appear smoother and less pores are observed. With time this effect becomes clearly visible as indicated by the two SEM images on the right side. Thus, Ra seems to have a major impact on the recrystallization of barite which may be catalytic to the formation of the typical barite crystal morphology.

Conclusions

The recrystallization experiments starting with a Ra concentration of $5 \cdot 10^{-6}$ mol/L show a very efficient uptake of Ra by barite. The experiments at room temperature indicate three different kinetic stages of the Ra uptake which are best identified in the experiments with a starting solid/liquid ratio of 0.5 g/L. The experimental data can be fitted best with a solubility product of the $RaSO_4$ endmember of log Ksp = -10.41 and a Guggenheim parameter $a_0 = 0.6$. TOF-SIMS analyses of the final radiobarite powders indicate a full recrystallization leading to a homogenous distribution of Ra within the particles. The Ra/Ba ratios calculated from the experiments via mass balance correspond well with the typical Ra/Ba intensity ratio obtained via TOF-SIMS.

As predicted by thermodynamic modeling, the final Ra concentrations of comparable experiment at 90 °C are higher than at room temperature. Microscopic observation of samples taken at various times during the experiments indicates a significant impact of the presence of Ra on the recrystallization of barite.

Acknowledgement

The research leading to these results has received funding from the European Union's European Atomic Energy Community's (Euratom) Seventh Framework Program FP7-Fission-2010 under grant agreement number 269688 (CP-SKIN).

References

Bosbach, D.; Böttle, M. & Metz, V. Experimental study on Ra2+ uptake by barite (BaSO4), SKB Technical Report TR-10-43 Waste Management, Svensk Kärnbränslehantering AB, 2010

Curti, E.; Fujiwara, K.; Iijima, K.; Tits, J.; Cuesta, C.; Kitamura, A.; Glaus, M. & Müller, W. Radium uptake during barite recrystallization at 23±2°C as a function of solution

composition: An experimental 133Ba and 226Ra tracer study Geochimica et Cosmochimica Acta, 2010, 74, 3553-3570

Doerner, H. A. & Hoskins, W. M. Co-precipitation of radium and barium sulfates Journal of the American Chemical Society, 1925, 47, 662-675

Glynn, P., 2000. Solid-solution solubilities and thermodynamics: Sulfates, carbonates and halides. Sulfate Minerals - Crystallography, Geochemistry and Environmental Significance 40, 481-511.

Hummel, W.; Berner, U.; Curti, E.; Pearson, F. J. & Thoenen, T. Nagra / PSI Chemical Thermodynamic Data Base 01/01; Nagra technical report 02-16 2002

Kiseleva, I. A., Kotelnikov, A. R., Martynov, K. V., Ogorodova, L. P., and Kabalov, J. K., 1994. Thermodynamic Properties of Strontianite-Witherite Solid-Solution (Sr,Ba)Co3. Phys Chem Miner 21, 392-400.

Kulik, D.; Wagner, T.; Dmytrieva, S.; Kosakowski, G.; Hingerl, F.; Chudnenko, K. & Berner, U. GEM-Selektor geochemical modeling package: Numerical kernel GEMS3K for coupled simulation codes. Computational Geosciences, 2012 (in press)

Lind, S.C., Underwood, J.E., Whittemore, C.F., 1918. The solubility of pure radium sulfate. The Journal of the American Chemical Society XL, 465-472.

Lippmann, F., Phase diagrams depicting aqueous solubility of binary mineral systems. N. Jb. Miner. Abh 1980, 139, 1-25.

Nikitin, B., Tolmatscheff, P., 1933. Article on the validity of mass effect law. II. Quantitative determination of solubility of radium-sulfate in sodium-sulfate solutions and in water. Zeitschrift für physikalische Chemie – Abteilung A – Chemische Thermodynamik Kinetik Elektrochemie Eigenschaftslehre 167, 260-272.

Paige, C.R., Kornicker, W.A., Hileman, O.E.J., Snodgrass, W.J., 1998. Solution equilibria for uranium ore processing: The BaSO4-H2SO4-H2O system and the RaSO4-H2SO4-H2O system. Geochimica et Cosmochimica Acta 62, 15-23.

Plummer, L. N. and Busenberg, E., 1987. Thermodynamics of Aragonite-Strontianite Solid-Solutions - Results from Stoichiometric Solubility at 25-Degrees-C and 76-Degrees-C. Geochim Cosmochim Ac 51, 1393-1411.

Prieto, M. Thermodynamics of Solid Solution-Aqueous Solution Systems Thermodynamics and Kinetics of Water-rock Interaction, 2009, 70, Mineralog Soc Amer; Geochem Soc

Wagner, T.; Kulik, D.; Hingerl, F. & Dmytrieva, S. GEM-Selektor geochemical modeling package: TSolMod library and data interface for multicomponent phase models Canadian Mineralogist, 2012, 50, 701 - 723

Zhu, C. Coprecipitation in the barite isostructural family: 1. binary mixing properties 1 Geochimica et Cosmochimica Acta, 2004, 68, 3327-3337

RECRYSTALLIZATION OF 223-RADIUM WITH BARITE

Natallia Torapava[1*], Hanna Hedström[1], Henrik Ramebäck[1,2], Gunnar Skarnemark[1] and Christian Ekberg[1]

[1] Department of Chemical and Biological Engineering, Nuclear Chemistry, Chalmers University of Technology, SE-41296, Gothenburg, Sweden

[2] Swedish Defence Research Agency, Division of CBRN Defence and Security, SE-90182, Umeå, Sweden

* Corresponding author: torapava@irs.uni-hannover.de

Abstract

The kinetics of 223-radium and 133-barium recrystallization with barium sulphate at low concentrations, i.e. 10^{-13} mol·L^{-1} have been studied in the acidic 0.01 mol·L^{-1} sodium sulfate solution. The results show a decrease in both 223-radium and 133-barium concentrations in solution when barium sulfate crystals are present in the system. The system follows first order reaction behavior both for barium and radium. The EXAFS data of solid radium sulphate were collected. The Arrhenius parameters, the activation energy, E_a, pre-exponential factor, A, for the co-precipitation of the radium, barium and strontium systems in sulfate media were determined.

Introduction

A co-precipitation study of radium and barium sulphates showed that in a large excess of barium over radium, radium sulphate will precipitate even though the solubility product of radium sulphate is not reached ***(Doerner et al. (1925))***. Later, Gordon and Rowley confirmed the Doerner and Hoskins distribution law of radium between the aqueous and solid phases during their co-precipitation studies ***(Gordon et al. (1957))***. Two conditions of this distribution law should be obeyed: the surface of the growing crystal should be in equilibrium with the body of the solution and the rate of diffusion of ions within the crystalline lattice should be negligible compared to the rate of precipitation ***(Doerner et al. (1925), Gordon et al. (1957))***. The solubility product of radium sulphate was estimated to be $\log K_{sp}$ = -10.26 ***(Langmuir et al. (1985))***. The radium concentration in natural waters is rather small, ca. 10^{-12} mol·L^{-1} and seems to be controlled by the solubility of trace amounts of radium in minerals, as e. g. barite ***(Langmuir et al. (1985))***. Although the short-lived isotopes ^{223}Ra and ^{224}Ra are unlikely to be significantly involved in solution-mineral equilibria, all radium isotopes must participate in complexation and adsorption-desorption processes ***(Langmuir et al. (1985))***. Radium incorporation into barium sulphate is a process which controls the solubility of ^{226}Ra in natural and anthropogenic waters, as e.g. uranium mining tailings or oil production environment ***(Grandia et al. (2008))***.

Previous studies of 226-radium(II) uptake by barite, in the concentrations about 10^{-7} mol·L^{-1} and pH = 5, indicated that equilibration between radium(II) ions and barite involves a significant part of the initial barite and proceeds beyond pure adsorption processes ***(Bosbach et al. (2010))***. Various parameters such as specific surface area, amount of sample, ionic medium may affect the kinetics of radium exchange with barite. Uranium mining tailings, which have rather high acidity, may mobilize radium into the environment under some conditions ***(Sebesta et al. (1981), Martin et al. (2003), Grandia et al. (2008))***. However, the radium(II) uptake by barite at concentrations found in the environment and at low pH as well as kinetics of isotopic exchange of ^{226}Ra and ^{223}Ra isotopes have not been studied earlier. The aim of this study was to investigate the recrystallization kinetics at low concentrations, i.e. $<10^{-13}$ mol·L^{-1}, of $^{223}Ra^{2+}$, a radionuclide often used in targeted cancer therapy ***(Larsen et al. (2003), Dahle et al. (2007), Nilsson et al. (2007))***, on the surface of synthesized barium sulphate having a particle size of 0.5 – 1 mm in 0.01 mol·L^{-1} sodium sulfate solution used as ionic medium.

1. Experimental

1.1 Reagents and materials

Milli-Q water (18 MΩ) was used throughout the experiments to make all solutions up to volume. Nitric acid (Sigma-Aldrich, ≥ 69%), hydrochloric acid (Labassco, 37%), barium chloride dehydrate (Aldrich, 99.999+%), sodium sulphate (Aldrich, 99.99+%), 133-barium chloride in 0.1 mol·L^{-1} hydrochloric acid with a total activity of 4MBq (Eckert & Ziegler Nuclitec GmbH), 227-actinium(III) nitrate solution in 2 mol·L^{-1} nitric acid with total activity of 273 kBq (Isotrak, QSA Amersham International), and Actinide Resin (Eichrom, 35-70 μm silica) were used. All plastic bottles and test-tubes were washed with 50% nitric acid before the experiments. All samples were filtered through 0.02 μm filters (Whatman) before gamma spectrometric measurement. Barium sulphate was synthesized following the method described elsewhere, Figures S1 and S2 ***(Patel and Koshy 1968)***. 226-radium sulfate was prepared as described elsewhere ***(Hedstrom, Foreman et al. 2012)***.

1.2 Methods

The gamma spectrometric measurements in this study were done using a high purity germanium detector, HPGe, (Canberra γ-analyst). The relative efficiency of the detector was about 24.6%, and the resolution was 1.84 keV at 1332 keV.

Powder diffraction data were collected on a Bruker D2 Phaser diffractometer using CuK_α radiation with the sample placed on a silicon plate.

A scanning electron microscope TM 3000, Hitachi, was used to analyze the barium sulfate particles size. The sample was attached onto a carbon film.

1.3 ^{223}Ra generator system

As ^{223}Ra is only available from ^{227}Ac, possible separation methods were considered ***(Mitsugashira et al. (1977), Alhassanieh et al. (1999), Henriksen et al. (2001), McAlister et al. (2011), Möller et al. (2011))***. A simple and relatively effective way of separating ^{223}Ra from ^{227}Ac source was via actinide resin (P,P´-di(2-ethylhexyl)methanediphosphonic acid) ***(Henriksen et al. (2001))***. For that purpose 10 mL plastic column (BIO RAD) was packed with glass wool followed by actinide resin preliminary soaked in 1 mol·L^{-1} hydrochloric acid (half volume of predetermined volume) and then with a top layer of actinium resin, which was preliminary agitated in 2 mL of actinium solution for four hours as described elsewhere ***(Henriksen et al. (2001))***. Elution of ^{223}Ra to be used in the experiments was done with 1 mol·L^{-1} hydrochloric acid.

1.4 Radiometric measurements

All samples with the total volume of 1 mL were measured in 10 mL plastic test-tubes to obtain fixed measurement geometry, equivalent to the calibrated geometry in the gamma spectrometric measurements. 0.1 mL of radium from the generator system was diluted to 1 mL with 1 mol·mL^{-1} hydrochloric acid and was measured directly after the elution.

1.5 Preparation of solutions

For the experiments with $^{223}Ra^{2+}$ six solutions were prepared, Table 1. Three solutions (systems 1 – 3) containing 100 mL of 0.01 mol·L^{-1} sodium sulfate and 0.05 g of barium sulfate in 250 mL plastic bottles were prepared and left to equilibrate for one and half week. After that, $^{223}Ra^{2+}$ and $^{133}Ba^{2+}$ spikes were added according to the Table 1. The other three solutions (systems 4 – 6) contained 100 mL of 0.01 mol·L^{-1} sodium sulfate solution with $^{223}Ra^{2+}$ and $^{133}Ba^{2+}$ spikes to study the effect of the adsorption on the walls of the plastic bottle.

For the experiments studying $^{223}Ra^{2+}$ and $^{133}Ba^{2+}$ exchange with 226-radium sulfate, three solutions were prepared, Table 2. Several grains of 226-radium sulfate powder were placed into 100 mL plastic beakers filled with 100 mL of 0.01 mol·L^{-1} sodium sulfate solution and left for equilibration for 1.5 months. After that time ^{223}Ra and ^{133}Ba spikes were added according to the Table 2.

Table 1: *Composition of the solutions for the experiment with $BaSO_4$(s)*

System	$BaSO_4$(s), g	Ionic medium	^{223}Ra or ^{133}Ba added
1	0.05		^{223}Ra and ^{133}Ba
2	0.05		^{223}Ra
3	0.05	0.01 mol·L^{-1} Na_2SO_4	^{133}Ba
4	not added		^{223}Ra and ^{133}Ba
5	not added		^{133}Ba
6	not added		^{223}Ra

Table 2: *Composition of the solutions for the experiment with 226$RaSO_4$(s)*

System	$RaSO_4$(s)	Ionic medium	^{223}Ra or ^{133}Ba added
7	Added	0.01 mol·L^{-1} Na_2SO_4	^{223}Ra
8	added		^{133}Ba
9	added		^{223}Ra and ^{133}Ba

All uncertatinties presented in this work were calculated in accordance with GUM ***(2008)*** using the Kragten spreadsheet approach ***(Kragten (1994))***. All uncertainties in this paper are expanded uncertainties with a coverage factor of two (k = 2), yielding an approximate confidence interval of 95 %, unless otherwise stated.

1.6 Characterization of radium sulfate

The crystal structure of radium sulphate was investigated and compared to the structures of barium, strontium and lead sulphates. It was confirmed that radium sulphate is isostructural with barium, strontium and lead sulphates. The radium sulphate powder was measured both by powder X-ray diffraction (XRD) and EXAFS. The unit cell was determined to be orthorhombic, belonging to the Pnma (No. 62) space group with the cell parameters a = 9.07 Å, b = 5.52 Å, c = 7.28 Å and V = 364.48 Å^3. The bond distances were determined using EXAFS. The mean Ra-O and S-O bond distances were found to be 2.96(2) Å and 1.485(8) Å respectively and the Ra-O-S bond angle was 127(2)°.These data were consistent with and supported the XRD data. These findings show that it is possible for radium to co-precipitate with barium, strontium and lead in sulphate media to form a substitutional solid solution.

1.7 Co-precipitation studies

In this work the kinetic reaction behavior of the radium, barium and strontium co-precipitation systems in sulphate media is studied by making Arrhenius plots and evaluating the activation energies of the experiments.

The co-precipitation was believed to follow a first order kinetic behavior, the rate constant k is determined *via* a linear regression of ln(c) *vs*. time, where the slope gives $-k$. In accordance with Eq. (1) the determined rate constants were then used for the Arrhenius plot shown in Figure 1.

$$\ln(k) = -E_a/(R \cdot T) + \ln(A) \quad (1)$$

2. Results and Discussion

The reactions of the radium, barium and strontium co-precipitation systems in sulphate media are showing an Arrhenius behavior, *i.e.* the relationship between ln(k) and 1/T is linear in the temperature range of 10 – 30 ºC, Figure 1. This means that the Arrhenius parameters, E_a and A can be determined using Eq. (1). The Arrhenius parameters obtained in this work are shown in Table 3.

Table 3: *Composition of the solutions for the experiment with* $^{226}RaSO_4(s)$

	E_a/R [K]	ln(A)
100 % Ba	7524 ± 206	21.22 ± 0.74
50 % Ba 50 % Ra	6182 ± 180	16.64 ± 0.64
100 % Ra	5623 ± 228	15.00 ± 0.68

Short-lived ^{223}Ra ($t_{1/2}$ = 11.3 days) has an advantage over ^{226}Ra ($t_{1/2}$ = 1600 years) by decreased detection limit below the picomolar level and non-generation of long-lived radioactive waste. The fast decay of the ^{223}Ra may be a problem for the thermodynamic interpretation of the data, because of continuously changing system composition. Whether a thermodynamic equilibrium will be achieved will thus depend on sufficiently high recrystallization rate. Figure 2 shows that decrease of simultaneously added spikes of $^{223}Ra^{2+}$ and $^{133}Ba^{2+}$ is fast within 400 hours and slows down at longer time. The decrease in $^{223}Ra^{2+}$ and $^{133}Ba^{2+}$ concentrations by about one order of magnitude is observed. The calculated solubility of Ba^{2+} in 0.01 mol·L^{-1} $NaSO_4$ solution is $9.5 \cdot 10^{-8}$ mol·L^{-1}. The concentrations of $^{223}Ra^{2+}$ and $^{133}Ba^{2+}$ spikes are far below the calculated solubility. The reaction order of both $^{223}Ra^{2+}$ and $^{133}Ba^{2+}$ uptake is one, i.e. linear decrease of concentrations with time is observed, Figure 3. A Figure 4 shows that when $^{223}Ra^{2+}$ and $^{133}Ba^{2+}$ are added individually to $BaSO_4$(s) in 0.01 mol·L^{-1} $NaSO_4$ solution the decrease in their concentrations follows the same pattern and magnitude as shown in Figure 2. The adsorption of either $^{223}Ra^{2+}$ or $^{133}Ba^{2+}$ on the walls of the reaction vessel can be ruled out, Figure 5. It was shown that addition of a new spike of $^{223}Ra^{2+}$ into solution where initially added $^{223}Ra^{2+}$ was consumed and $^{133}Ba^{2+}$ is still present lead to further decrease in $^{223}Ra^{2+}$ and $^{133}Ba^{2+}$ concentrations, Figure 6. However, after second addition of $^{223}Ra^{2+}$ spike, $^{133}Ba^{2+}$ concentration first increased, between 1008 and 1080 hours,

before it started to decrease again. This means that within this time some of formed radium-barite has dissolved, whereas decrease of $^{223}Ra^{2+}$ concentration shows that simultaneous growth of new secondary radium-barite is observed.

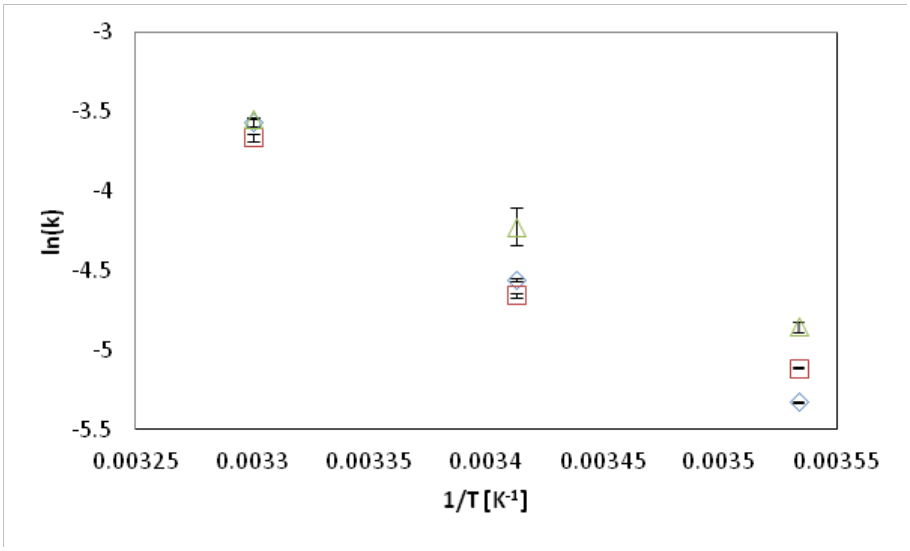

Figure 1: *ln(k) vs 1/T, for pure radium (Δ), pure barium (◊) and for a 50/50 radium/barium mixture (□). The linear regression for these systems gives r2-values between 0.97-0.99 for the different systems.*

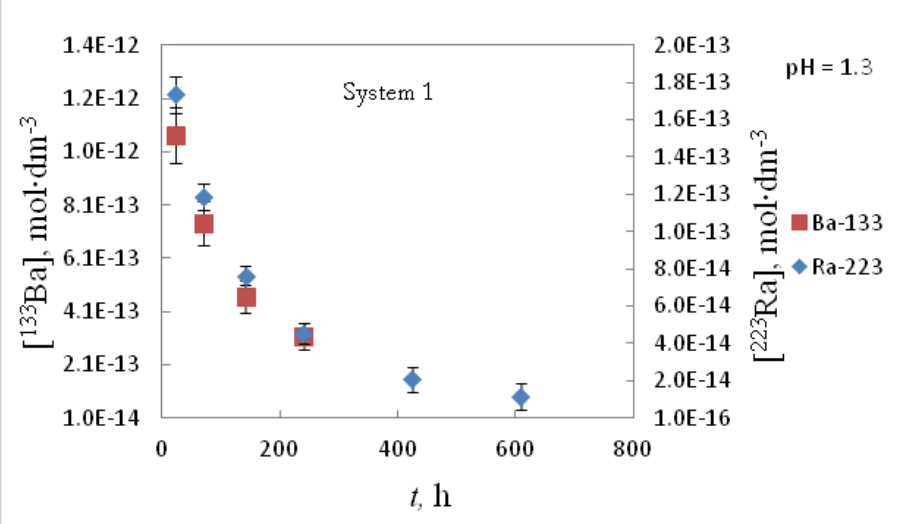

Figure 2: *$^{223}Ra^{2+}$ and $^{133}Ba^{2+}$ concentrations change with time in the system containing $BaSO_4(s)$*

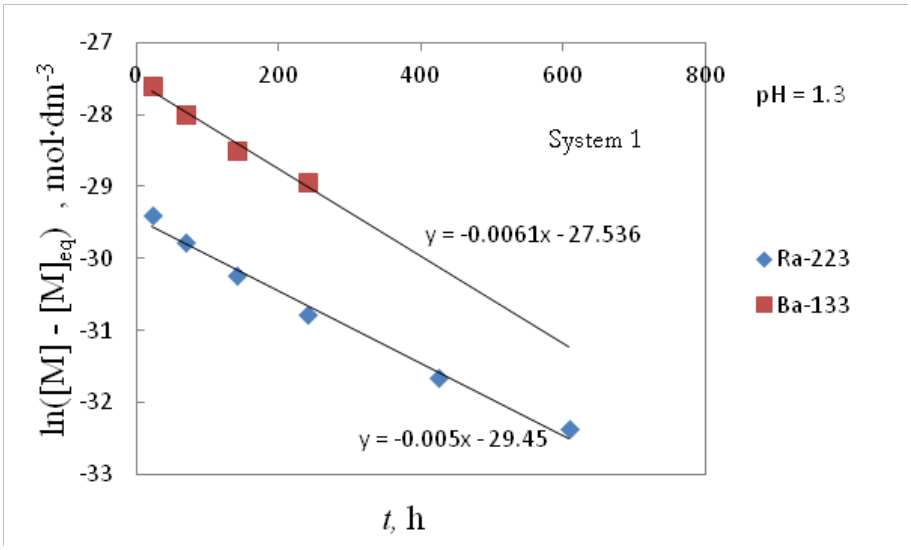

***Figure 3**: $^{223}Ra^{2+}$ and $^{133}Ba^{2+}$ reaction order in the system containing $BaSO_4(s)$*

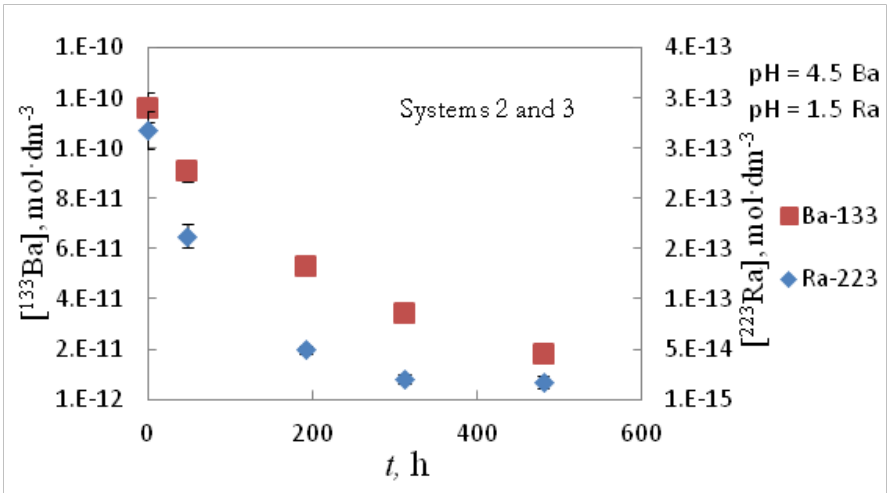

***Figure 4:** $^{223}Ra^{2+}$ and $^{133}Ba^{2+}$ concentrations change with time in the systems 2 and 3 respectively, containing $BaSO_4(s)$*

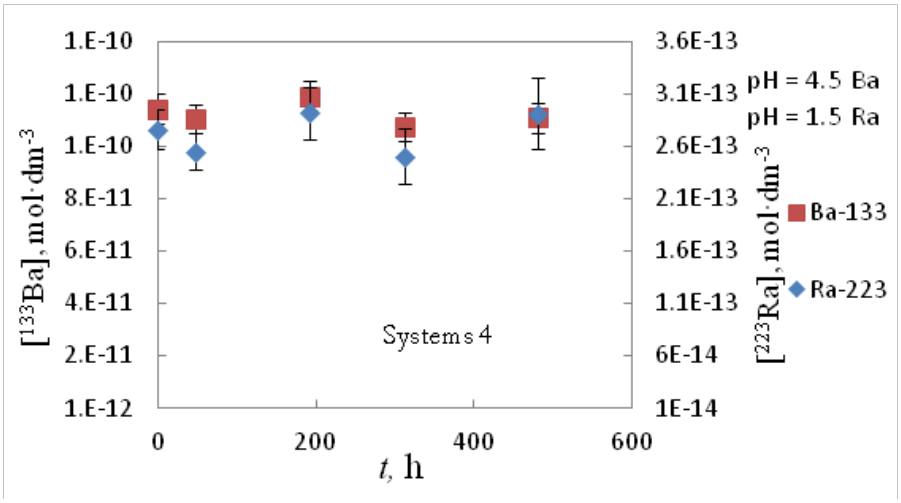

Figure 5: *$^{223}Ra^{2+}$ and $^{133}Ba^{2+}$ concentration change in the system containing $BaSO_4$(s)*

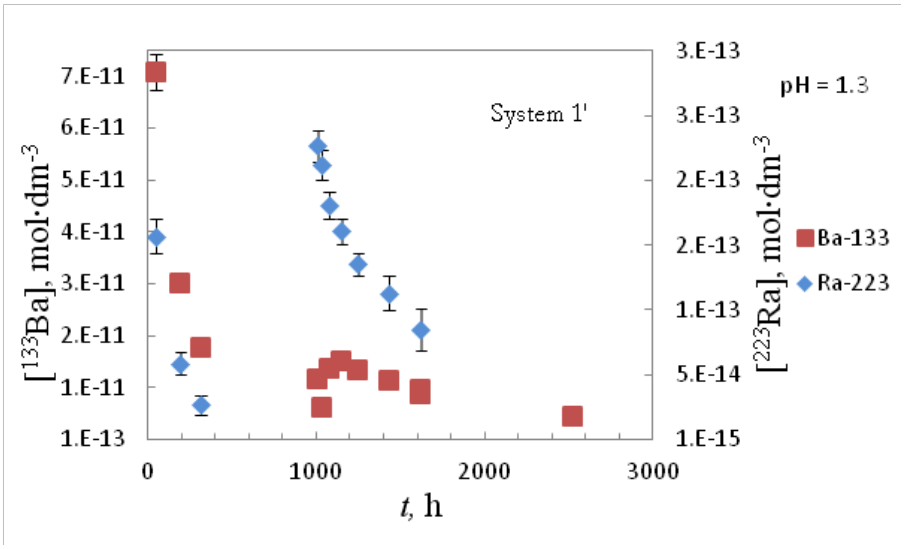

Figure 6: *$^{223}Ra^{2+}$ and $^{133}Ba^{2+}$ concentrations change with time in the system containing $BaSO_4$(s), after 42 days spiked with more $^{223}Ra^{2+}$*

Conclusions and Future work

The decrease in both $^{223}Ra^{2+}$ and $^{133}Ba^{2+}$ concentrations by one order of magnitude is observed in the systems containing barium sulfate. The concentration of $^{223}Ra^{2+}$ was ca. 10^{-13} mol·L^{-1} as low as could be found in nature and the recrystallization of $^{223}Ra^{2+}$ with barium sulphate is observed despite the very low concentration of radium.

The activation energy of the pure radium, barium and strontium sulphates decreases in the order Sr>Ba>Ra, which may be correlated to their ionic size, since this effects the ability to lose their hydration water.

$^{223}Ra^{2+}$ and $^{133}Ba^{2+}$ recrystallization with 226-radium sulphate will be studied in the future work.

Acknowledgement

The research leading to these results has received funding from the European Union's European Atomic Energy Community's (Euratom) Seventh Framework Programme FP7-Fission-2010 under grant agreement n° 269688 (SKIN project).

References

(2008). "JCGM 100: 2008, GUM 1995 with minor corrections, Evaluation of measurement data - Guide to the expression of uncertainty in measurement." from http://www.bipm.org.

Alhassanieh, O., A. Abdul-Hadi, M. Ghatar, A. Aba (1999). "Separation of Th, U, Pa, Ra and Ac from natural uranium and thorium series." Applied Radiation and Isotopes **51**: 493-498.

Bosbach, D., M. Böttle, V. Metz (2010). Experimental study on Ra^{2+} uptake by barite ($BaSO_4$)

Kinetics of solid solution fromation via $BaSO_4$ dissolution and $Ra_xBa_{1-x}SO_4$ (re)precipitation Stockholm, Swedish Nuclear Fuel and Waste Management Co**:** 106.

Dahle, J., J. Borrebak, Jonasdottir, T. J., Hjelmerud, A. K., Melnus, K. B., Bruland, O. S., Press, O. W., Larsen, R. H. (2007). "Targeted cancer therapy with a novel low-dose rate α-emitting radioimmunoconjugate." Blood **110**(6): 2049-2056.

Doerner, H. A. and W. M. Hoskins (1925). "Co-precipitation of radium and barium sulfates." Journal of the American Chemical Society **47**: 662-675.

Gordon, L. and K. Rowley (1957). "Coprecipitation of radium with barium sulfate." Analytical chemistry **29**(1): 34-37.

Grandia, F., J. Merino, J. Bruno (2008). Assessment of the radium-barium co-precipitation and its potential influence on teh solubility of Ra in the near-field. Stockholm, Swedish Nuclear Fuel and Waste Management Co**:** 52.

Hedstrom, H., M. Foreman, C. Ekberg, H. Ramebäck. (2012). "Radon capture with silver exchanged zeolites." Radiochimica Acta **100**(6): 395-399.

Henriksen, G., P. Hoff, J. Alstad, R. H. Larsen (2001). "^{223}Ra for endoradiotherapeutic applications prepared from an immobilized $^{227}Ac/^{227}Th$ source." Radiochimica Acta **89**: 661-666.

Kragten, J. (1994). "Calculating Standard Deviations and Confidence Intervals with a Universally Applicable Spreadsheet Technique." Analyst **119**: 2161 - 2165.

Langmuir, D. and D. Melchior (1985). "The geochemistry of Ca, Sr, Ba and Ra sulfates in some deep brines from the Palo Duro Basin, Texas." Geochimica et Cosmochimica Acta **49**: 2423-2432.

Langmuir, D. and A. C. Riese (1985). "The thermodynamic properties of radium." Geochimica et Cosmochimica Acta **49**: 1593-1601.

Larsen, R. H. and O. S. Bruland (2003). "Targeting of skeletal metastases by alpha-emitter radium-223." Targeted Cancer Therapis (29): 195-202.

Martin, A. J., J. Crusius, J. J. McNee, E. K. Yanful (2003). "The mobility of radium-226 and trace metals in pre-oxidized subaqueous uranium mill tailings." Applied Geochemistry **18**(7): 1095-1110.

McAlister, D. R. and E. P. Horwitz (2011). "Chromatographic generator systems for the actinides and natural decay series elements." Radiochimica Acta **99**: 151-159.

Mitsugashira, T., H. Yamana, Suzuki, S. (1977). "The Mutual Separation of ^{227}Ac, ^{227}Th, ^{223}Ra, and ^{223}Fr by the Solvent Extraction Technique Using Bis(2-ethylhexyl)phosphoric Acid as an Extractant." Bulletin of the chemical society of Japan **50**(11): 2913-2916.

Möller, T., N. Bestaoui, Wierzbicki, M., Adams, T., Clearfield, A. (2011). "Separation of lanthanum, hafnium, barium and radiotraces yttrium-88 and barium-133 using crystalline zirconium phosphate and phosphonate compounds as prospective materials for a Ra-223 radioisotope generator." Applied Radiation and Isotopes **69**: 947-954.

Nilsson, S., L. Franzén, Parker, C., Tyrrell, C., Blom, R., Tennvall, J., Lennernäs, B., Petersson, B., Johannessen, O. C., Sokal, M., Pigott, K., Yachnin, J., Garkavij, M., Strang, P., Harmenberg, J., Bolstad, B., Bruland, O. S. (2007). "Bone-targeted radium-223 in symptomatic, hormone-refractory prostate cancer: a randomised, multicentre, placebo-controlled phase II study." The Lancet Oncology **8**(7): 587-594.

Patel, A. R. and J. Koshy (1968). "Growth of barium sulphate single crystals by chemically reacted flux method." Journal of Crystal Growth **2**: 128-130.

Sebesta, F., P. Benes, Sedlacek, J., Sandrik, R. (1981). "Behavior of radium and barium in system including uranium-mine waste-waters and adjacent surface waters" Environmental Science & Technology **15**(1): 71-75.

EFFECT OF TEMPERATURE ON THE DISSOLUTION OF CLAYEY MATERIALS

Tomo Suzuki-Muresan[1*], Karine David[1], Bernd Grambow[1]

[1] SUBATECH, Unité Mixte de Recherche 6457, Ecole des Mines de Nantes, CNRS/IN2P3, Université de Nantes, 4 rue Alfred Kastler, BP 20722, 44307 Nantes cedex 03, France

* Corresponding author: tomo.suzuki@subatech.in2p3.fr

Abstract

Surface studies on illite, illite/smectite and Callovo-Oxfordian argillite clay mineral phases were performed in conditions close to equilibrium for three temperatures (35°, 50° and 90°C) in 0.01 mol/L NaCl solution. Prior the experiments, clays were purified to remove impurities and secondary accessory mineral phases, in particular the quartz phase. Characterization of the solids was done by XRD and quantification by Rietveld refinement. Concentrations of Si, Fe and Al were measured in solution by Q-ICP-MS. Maximum concentration of Si values were determined for each solids in contact with the solution and a pseudo-equilibrium is reached after 50 days of contact time. These values ($\sim 10^{-5}$ - $\sim 10^{-4}$ mol/L) under the solubility of quartz values corresponds to the solubility values of the clays. Concentration of Fe is 2.5×10^{-6} mol/L and Al is 3×10^{-6} mol/L in solution. This work is the first part of the study to prepare the clay mineral phases in close to equilibrium conditions. This work includes also the preparation of the tracer which will be introduced in the studied system as a spike of ^{29}Si.

Introduction

According to the French laws for the management of nuclear wastes, high level nuclear glass wastes are planned to be stored in deep geological formation. At 490 m in depth, the Callovo-Oxfordian formation presents interesting properties in terms of high retention coefficients of radionuclides, low permeability of water, large specific surface area, reactivity and pronounced sorption capacity ***(ANDRA (2005), Bergaya et al. (2006))***. This geological formation is mainly characterized by the presence of illite, interstratified illite/smectite 40-45 %, carbonates 30-40 %, tectosilicates 20-30 % and pyrite 1-2 % ***(Gaucher et al. (2004))***. Prior the determination and the acceptance by the public of the final site for the geological disposal CIGEO directed by ANDRA, an underground research laboratory has been built in Meuse/Haute-Marne in the Callovo-Oxfordian formation (northeastern, France) to evaluate the feasibility of disposal of radioactive wastes in a deep clay rock formation. After having filled the galleries by the nuclear waste (high level long live and intermediate level long live), the disposal locations will be sealed from access tunnels by bentonite plugs. The Callovo-Oxfordian argillite host rock and the bentonite will both become saturated with the

groundwater. The increase of temperature caused by the high level nuclear waste may also change the chemical and physical properties of the clay barrier and in particular its dissolution kinetics.

In literature, a number of studies are performed on dissolution of clays minerals focusing on the temperature dependence and pH effects ***(eg. Bauer and Berger (1998); Ganor et al. (1995); Huertas et al. (2001); Köhler et al. (2003); Palandri and Kharaka (2004); Rozalén et al. (2009))***. The overall results showed a typical dissolution rates profile with an increasing of rates values in the acid and alkaline pH-range, and a minimum in near neutral pH. However, rare are the studies on understanding of clays surfaces in conditions close to equilibrium. A recent study, with illite and montmorillonite, showed that a dynamic equilibrium is established between the claystone and the porewater and is described as a dissolution/precipitation mechanism ***(Suzuki-Muresan et al. (2011))***. Current models consider that the frayed edge sites are stable but these recent results with illite coupled to $Si/^{32}Si$ isotopic exchange studies indicate that an ongoing dissolution/precipitation mechanism at solubility equilibrium may be related to a permanent dissolution/reconstruction on frayed edge sites.

Related to the context of nuclear waste disposal in deep geological formation, the high level nuclear waste vitrified by PUREX method will be stored in tunnels and sealed by swelling clays materials as bentonite plugs for the French programme. Considering the resaturation period and the equilibrium time with the bentonite and the Callovo-Oxfordian argillite, the concentration of Si in the porewater in equilibrium with the Callovo-Oxfordian argillite (1.8×10^{-4} mol/L, Tournassat et al. 2007) will increase to the maximum concentration of 2×10^{-3} mol/L in presence of bentonite ***(Suzuki-Muresan et al. (2011))***. This later is four times higher than the solubility of the nuclear glass waste ([Si] 5×10^{-4} mol/L at 90 °C; ***Daux et al., 1997; De Cannière et al., 1998)***. The contribution of tectosilicates impurities in the Callovo-Oxfordian argillite may contribute to the inventory of silicium in the porewater and may control the solubility of the clay. Thus, the bentonite may control the dissolution of the nuclear glass waste. The question raised in this study is how the surface of the Callovo-Oxfordian argillite will react at the interface between the argillite and the nuclear glass waste. For that, two clay minerals (illite and interstratified illite/smectite) considered as reference materials are studied and compared to the Callovo-Oxfordian argillite at different temperature. The work is focused on the close to equilibrium conditions in the experiments. The assessment of the surface reactivity is performed by the $^{29}Si/^{28}Si$ isotopic exchange.

1. Materials and methods

1.1 Solid materials

Natural clayey samples were used for this project: (i) illite/smectite ISCz1 provided by Clay Mineral Society (C.M.S.) (0.5 wt% quartz, 1 wt% kaolinite) and (ii) illite IMT2 from C.M.S.

(7.5 % quartz, 2 % microcline); (iii) Callovo-Oxfordian argillite from the Underground Research Laboratory at Bure (40–45 % illite, interstratified illite/smectite, 20-30 % quartz, 30-40 % carbonate, 1-2 % pyrite ***(ANDRA, 2005b; Gaucher et al., 2004))***. The samples contain a fraction of quartz phase which the proportions could be considered as none neglectable for the experiments. The clayey samples were therefore purified by the method of elutriation defined as "*the process of separating the lighter particles of a powder from the heavier ones by means of an upward directed stream of fluid (gas or liquid)"* ***(IUPAC, 1997)***.

1.2 Batch experiments

The experiments were performed in batch systems for three temperatures studied 35, 50 and 90 °C. The solution composition is a solution of NaCl 0.01 mol/L with an initial pH of 5.5. The aqueous solution is then filled into PFA Teflon reactors (Savillex, 250 mL) containing 1 g of solid. One reactor contains only one type of solid. This operation is repeated for each temperature at 35, 50 and 90 °C. For each set of temperature, one reactor containing only a solution of NaCl is prepared as blank experiment (free of solids). A total of 12 reactors were prepared (4 reactors × 3 temperatures) with a solid/solution (m/V) ratio of 6.7 g/L. The temperature of the oven was controlled by a digital system. Before sampling, the reactors were taken out of the oven and quenched at room temperature and filtered at 0.45 µm. Solution aliquots were taken, measured for pH (pHC3006 Ag/AgCl, Radiometer) and stored until they were analyzed.

Initial dissolution rates (expressed as Si release rates in mol Si/m²/s) were calculated from the variation of aqueous silicon concentrations far from the equilibrium at very early time in all system.

$$R_{dissolution} = \frac{[Si]_t - [Si]_0}{\frac{m}{V} \times SA/m \times t}$$

where $[Si]_t$ and $[Si]_0$ (mol/L) stand for the final and initial silicon concentrations in solution, m/V (g/L) for the ratio of the solid mass onto the solution volume, SA/m (m²/g) for the specific surface area and t (s) for the reaction time.

1.3 Analytical methods

Determinations of element concentrations in solution were carried out by plasma based techniques, namely Quadrupole Inductively Coupled Plasma Mass Spectrometry (ICP-QMS, X Series, Thermo Electron Corporation) and sector field High Resolution Inductively Coupled Plasma Mass Spectrometry (HR-ICP-MS, Thermo-Electron™ Element-XR instrument).

Q-ICP-MS. Aliquots sampled during the experiments were prepared for concentration measurements of silicon, iron and aluminum by ICP-QMS using external calibration with ^{45}Sc and ^{115}In as internal standards for signal drift correction. The quantification limit calculated as

ten times the standard deviation of the blank (i.e. 0.2 % HNO_3 solution) is equal to 7×10^{-7} mol/L for silicon, 7×10^{-8} mol/L for iron and 4×10^{-8} mol/L for aluminum. Multi-Element calibration standard and sample solutions for analysis were prepared in 2 % HNO_3. The ^{45}Sc-^{115}In mixed internal standard solution at 20 ppb was introduced on-line in all solutions. Any residual signal drift was corrected from the measurement of the "quality-check" multi-element standard performed every five samples. All standards used during the course of the study were supplied by Scp Science, ultrapure water was obtained with a Milli-Q water purification system and HNO_3 acid was purified by sub-boiling distillation.

1.4 Characterization methods

BET. The surface area of illite, interstratified illite/smectite and Callovo-Oxfordian argilite samples were determined from N_2 adsorption isotherms at 77 K experiments and obtained with a Micromeritics ASAP 2010 M. Prior to analyses, the samples were outgassed in vacuum overnight. Surface area of illite is 50.9 m²/g, interstratified illite/smectite 82.3 m²/g and Callovo-Oxfordian argillite 92.8 m²/g.

Granulometry. The particle size was determined by means of the particle sizing system (PSS) from CAD instrumentation. Size distributions (volume based) from 1 to 100 µm diameter range were determined by single-particle optical sensing using an AccuSizer™ 780 optical PSS.

XRD. Patterns were collected with a Bruker-AXS D5000 (Bragg-Brentano geometry Advance diffractometer (Bragg–Brentano geometry) equipped with a Cu anticathode under the following experimental conditions: 0.2 mm receiving slits and 1 mm divergence slits for radial divergence, a 16 mm-high receiving slit, and a 2.3° Soller slit. X-ray powder diffraction data were collected with a step size of 0.02° 2θ over the angular range from 10-60° 2θ. MAUD program ***(Luterroti, 2000)*** with the full pattern XRD Rietveld fitting procedure combined with a Fourier analysis were used to describe the broadening of peaks ***(McHale et al, 1997)***. This method consists in refining the experimental diffractograms from the structural model of the phases.

2. Results

2.1 Characterization of the solids

The characterizations by X-Ray diffraction of Callovo-Oxfordian argillite and illite are presented in Figure 30. The Figure presents the XRD patterns before (a, c) and after purification (b, d) of the clays, respectively. The quantifications of the different mineral phases constituting the clays after purification are presented in Table 5. The results indicate that the purification has decreased the quantity of quartz phase, considered as secondary accessory mineral phase, from 20-30 wt% to 6 wt% for the Callovo-Oxfordian argillite and from 7.5 wt% to 3 wt% for the illite. This method has not allowed the complete removal of

the quartz phase but it's a compromise between the decrease as much as possible the quantity of quartz phase and the preservation of the structure of the clays.

After purification, in the Callovo-Oxfordian argillite 22 wt% of illite, 20 wt% of montmorillonite-type, 18 wt% of muscovite and 25 wt% of kaolinite were recovered. In illite minerals, 90 wt% of illite were recovered as the main fraction. The granulometry of the clays after purification give a median diameter of particles of 1.0 ± 0.1 µm.

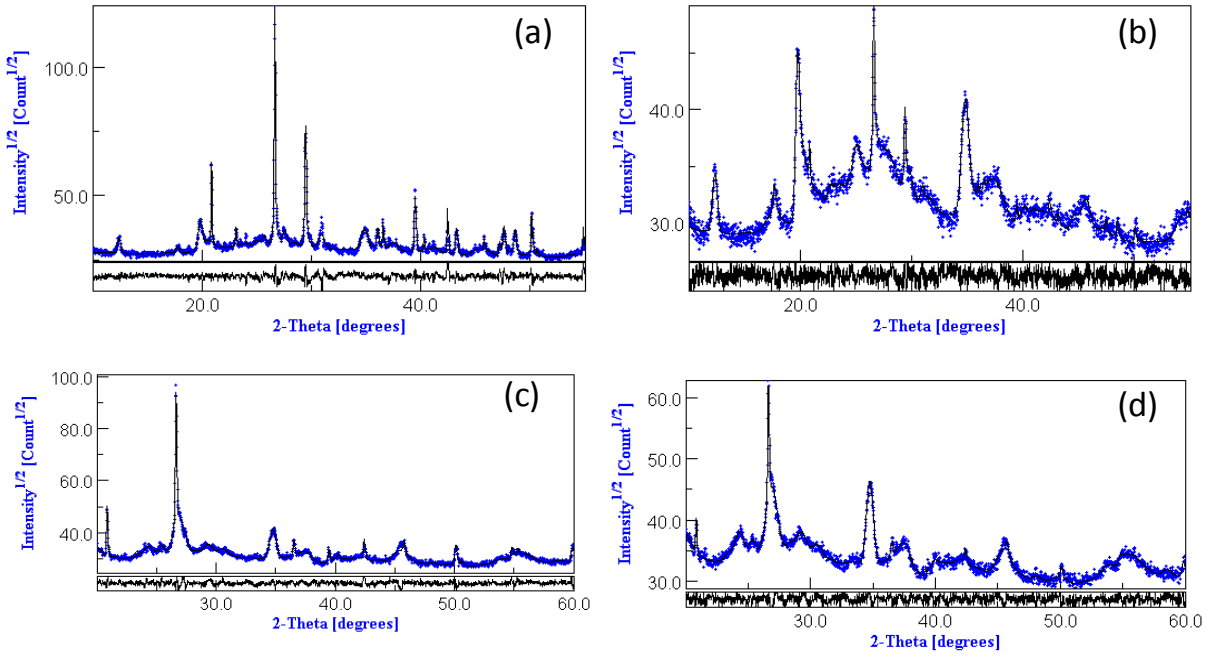

***Figure 30**: XRD patterns of Callovo-Oxfordian argillite (a, b) and illite/smectite (c, d) before and after purification, respectively. Blue points correspond to the experimental XRD patterns and the black line to the refinement XRD patterns.*

***Table 5:** Quantification by Rietveld method **(Luterroti (2000), McHale et al. (1997))** of mineral phases existing in the Callovo-Oxfordian argillite and illite after purification.*

Callovo-Oxfordian	***Weight % (± 1.5)***
Quartz	*6*
Calcite	*9*
Illite	*22*
Montmorillonite	*20*
Muscovite	*18*
Kaolinite	*25*

Illite	***Weight % (± 1.5)***
Quartz	*3*
Illite	*90*
Microcline	*4*
Kaolinite	*1*
Chlorite	*2*

The method of purification by elutriation has allowed to remove 76 % and 63 % of quartz fraction from the the Callovo-Oxfordian argillite and illite, respectively. For the illite/smectite, almost 100 % of the quartz fraction has been removed. This method has not completely removed all quartz fraction although sonification has been used to separate the secondary mineral phases from the clayey materials.

2.2 Dissolution of clays.

The results of the dissolution of illite/smectite, illite and Callovo-Oxfordian argillite are shown in Figures 31, 32 and 33, respectively, and present the concentration of Si (mol/L) measured in solution against the contact time (days) at 35, 50 and 90 °C. From a general observation, the concentrations at 35 and 50 °C are very similar and different to that of at 90 °C. After about 50 days, a maximum of Si-concentration is reached and those results are presented in Table 6. The concentrations of Si in presence of illite and illite/smectite are higher at 35 and 50 °C by a factor 2 compared with the Callovo-Oxfordian argillite. At 90 °C the concentrations in all the systems are similar. At low temperature, the dissolution of illite and/or illite/smectite seems not to participate to the dissolution of the Callovo-Oxfordian argillite due to the lower concentration of the later. The presence of muscovite and kaolinite in the Callovo-Oxfordian argillite request more investigation to assess the influence of each of the clay mineral phases present. At 90 °C, the results indicate clearly that illite and/or illite/smectite may control the dissolution of the Callovo-Oxfordian argillite.

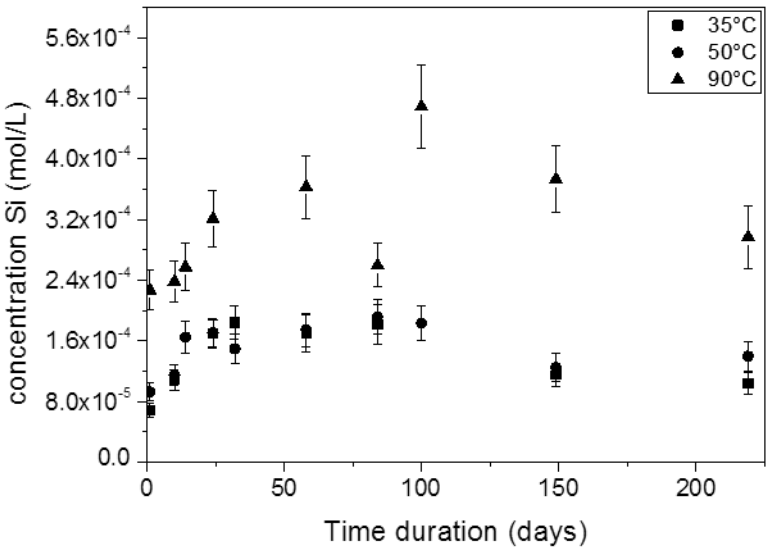

***Figure 31**: Evolution of Si-concentration in solution versus time for different temperature (35, 50, and 90 °C) for illite/smectite: m/V = 6.7 g/L, SA/m = 82.3 m²/g, NaCl 0.01 M, pH 5.6 – 6.3.*

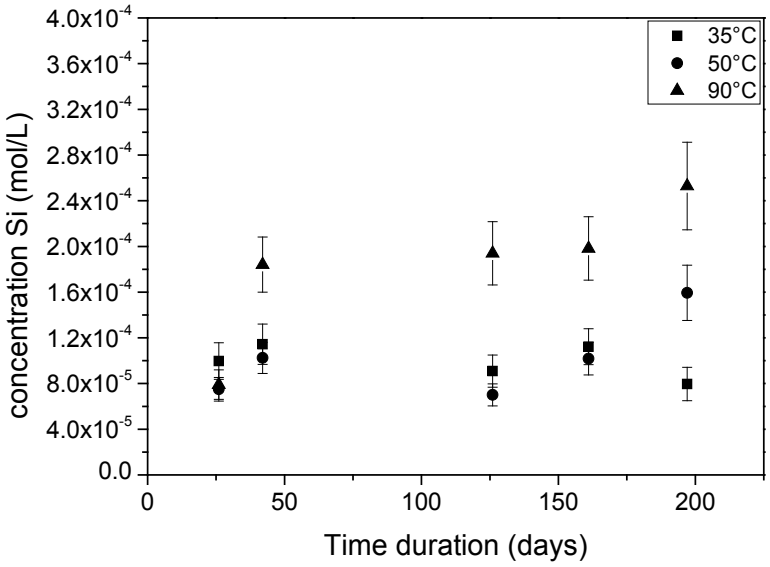

***Figure 32**: Evolution of Si-concentration in solution versus time for different temperature (35, 50, and 90 °C) for illite: m/V = 6.7 g/L, SA/m = 50.9 m²/g, NaCl 0.01 M, pH 6.1 – 5.8.*

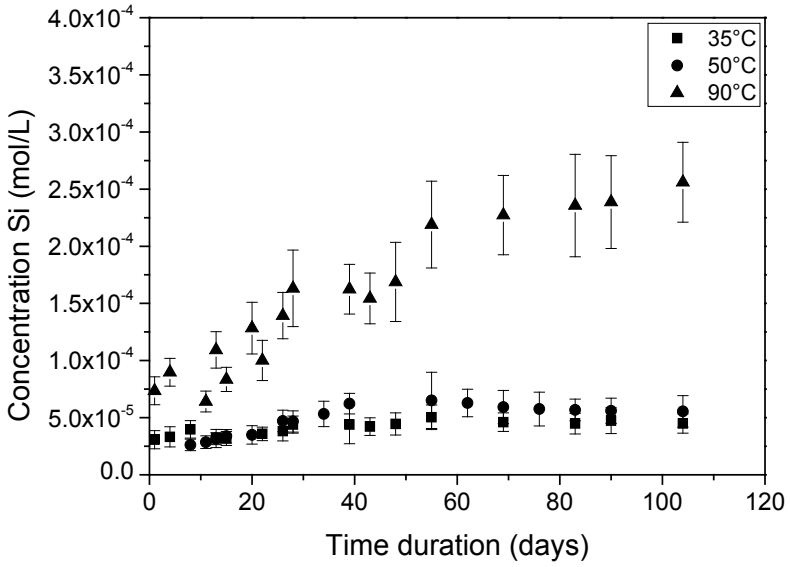

***Figure 33**: Evolution of Si-concentration in solution versus time for different temperature (35, 50, and 90 °C) for Callovo-Oxfordian argilite: m/V = 6.7 g/L, SA/m = 92.8 m²/g, NaCl 0.01 M, pH 8.0 – 8.2.*

***Table 6:** Maximal Si-concentration (mol/L) for illite, illite/smectite and Callovo-Oxfordian argillite (COx) at 35, 50 and 90 °C.The maximal concentration corresponds to the mean value for the period after 50 days of contact.*

	[Si] mol/L		
	Illite	**Illite/smectite**	**COx**
35 °C	$(1.1 \pm 0.6) \times 10^{-4}$	$(1.6 \pm 0.2) \times 10^{-4}$	$(3.9 \pm 0.8) \times 10^{-5}$
50 °C	$(1.2 \pm 0.2) \times 10^{-4}$	$(1.5 \pm 0.2) \times 10^{-4}$	$(5.7 \pm 0.6) \times 10^{-5}$
90 °C	$(2.2 \pm 0.3) \times 10^{-4}$	$(3.2 \pm 0.4) \times 10^{-4}$	$(2.0 \pm 0.3) \times 10^{-4}$

Comparing to the data published in ***Suzuki et al. (2011)***, the concentrations of Si in solution for the Callovo-Oxfordian argillite sample is lower in this study by a factor 2. This is could be explain by the presence of quartz fraction existing in the study of Suzuki et al. which has been removed by purification in this study. In this work, we have assessed the maximum concentration values of Si for the Callovo-Oxfordian argillite in conditions close to equilibrium. This implies that the quartz fraction in the geological disposal will be a key fraction and may compete with dissolution of the nuclear glass waste.

From the results (Figures 31-33), the initial dissolution rates R_{diss} (mol Si/m²/s) were calculated between 0 and 25 days or 0 – 50 days depending on the clays and the temperature. The results are presented in Table 7. The general observations show an increase of the

dissolution rates with the temperature and the rate values for the Callovo-Oxfordian argillite are lower than that of illite and illite/smectite by 0.8 to 0.3 orders of magnitude. The dissolution rate values are almost similar between illite and illite/smectite at 35 and 50 °C, while at 90 °C the values are close for the three clays.

Those results (Table 6) as well as the results from the maximum of Si-concentration (Table 7) indicate that the behavior of the dissolution of the Callovo-Oxfordian is a function of temperature. Illite and illite/smectite may not control the dissolution of the Callovo-Oxfordian argillite at low temperature but may influence at 90 °C. At 35 and 50 °C, other mineral phases such as kaolinite (for e.g.) may expect to be in competition with the two other clays.

Table 7: *Dissolution rates R_{diss} (mol Si/m²/s) illite/smectite, illite and Callovo-Oxfordian argillite (COx) at 35, 50 and 90 °C.*

	Log R_{diss} (mol Si/m²/s)		
	Illite	**Illite/smectite**	**COx**
35 °C	-13.6	-13.4	-14.2
50 °C	-13.5	-13.4	-13.7
90 °C	-12.7	-13.1	-13.4

In addition to the data collected on the concentration of Si measured in solution, aluminum and iron were measured in solution where the results are presented in Table 8. Due to the low concentration in solution, in particular for Fe, the quantification is not obvious even if precautions are taken (low dilution factor, use of internal standard…). For some samples, as for the case of illite, the concentration of Fe is about 8×10^{-7} mol/L, almost 1 order of magnitude higher than the quantification limit (QL) of the instrument. The release of Fe from illite and illite/smectite could be considered as neglectable whereas the concentration at 90°C in presence of illite/smectite is in the same order of magnitude of the one measured in presence of Callovo-Oxfordian argillite. For the later, the concentration of Fe at 35°, 50° and 90°C are about 2.5×10^{-6} mol/L. The concentration of Al in presence of clays is not influenced by the type of clays studied with a mean concentration value of 3×10^{-6} mol/L. The concentration evolved with temperature where at 90°C the concentration of Al in presence of illite/smectite and Callovo-Oxfordian argillite increase up to 1×10^{-6} mol/L and 8×10^{-6} mol/L, respectively.

Table 8: *Al-,Fe-concentrations (mol/L) for illite/smectite, illite and Callovo-Oxfordian argillite (COx) at 35, 50 and 90 °C.*

	[Fe] mol/L		
	Illite	**Illite/smectite**	**COx**
35 °C	<QL	$8 \pm 2 \times 10^{-7}$	$1.9 \pm 0.5 \times 10^{-6}$
50 °C	$8 \pm 2 \times 10^{-7}$	$5.4 \pm 0.5 \times 10^{-7}$	$3.3 \pm 0.7 \times 10^{-6}$
90 °C	$7 \pm 2 \times 10^{-7}$	$1.5 \pm 0.5 \times 10^{-6}$	$2.4 \pm 0.5 \times 10^{-6}$

	[Al] mol/L		
	Illite	**Illite/smectite**	**COx**
35 °C	$1.9 \pm 0.7 \times 10^{-6}$	$3.2 \pm 0.9 \times 10^{-6}$	$3.1 \pm 0.5 \times 10^{-6}$
50 °C	$1.5 \pm 0.6 \times 10^{-6}$	$3.0 \pm 0.7 \times 10^{-6}$	$4.2 \pm 0.7 \times 10^{-6}$
90 °C	$2.5 \pm 0.5 \times 10^{-6}$	$1.2 \pm 0.8 \times 10^{-5}$	$8 \pm 1 \times 10^{-6}$

Conclusions and Future work

The dissolution of illite, illite/smectite and Callovo-Oxfordian were perfomed at 35, 50 and 90 °C in NaCl 0.01 mol/L solution in batch system. Concentrations of Si, Fe and Al were measured in solution with a strong influence of temperature on the release rates and the maximum concentration in solution. The dissolution behaviour of the Callovo-Oxfordian argillite could be explained by the dissolution of the various mineral phases existing in argillite. Less than 90 °C, mineral phases such as kaolinite and/or muscovite could influence the dissolution behaviour whereas at temperature higher than 90 °C, illite and/or illite/smectite may control the dissolution of the argillite. The efficiency of the purification of clayey materials allow to consider that the quartz fraction is present in the minerals as impurities. The concentrations of Si measured in the experiments are lower than the solubility of quartz. This indicates that the influence of the quartz fraction contained in the clayey materials is neglectable in this study.

The next step concerns the isotopic exchange $^{29}Si/^{28}Si$. The tracer supplied by Euriso-top® as solid SiO_2 form with an enrichment of ^{29}Si up to 99.9 % was prepared on the base of the procedure of ***Van den Boorn et al. (2006)***. The tracer was prepared gravimetrically and dissolved in $NaOH.H_2O$ (99.99 % Suprapur) at 200 °C in a PFA pressure vessel. The working tracer solution was obtained after taking up the residue in Milli-Q water and then adding a 10 mol/L HCl solution in order to get a final concentration of silicon equal to 459.2 ± 1.2 µg/g (1 sigma) in 0.25 mol/L NaOH and pH 13.4. $^{29}Si/^{28}Si$ isotopic ratios are measured in medium resolution mode (R = 4000, Δm = 0.007 u.m.a. for m = 28, 29, 30) for complete removal of isobaric spectral interferences such as nitrogen, carbon based major molecular species on ^{28}Si, ^{29}Si and ^{30}Si. The use of a free-Si liquid sample introduction device with PFA Teflon nebulizer and spray chamber but also an injector torch made of platinum as well as purified

reagents will greatly improve the silicon instrumental background and as a consequence the accuracy and reproducibility of Si isotopic ratios after ^{29}Si tracer addition. Working silicon standards were prepared in 0.01 mol/L HCl from a 1000 mg/L stock solution (PlasmaCal, SCP Science). After several tests and validations on the preparation, detection and measurement of the tracer ^{29}Si by HR-ICP-MS, the tracer will be added in each reactor. The ratio $^{29}Si/^{28}Si$ will be measured and its evolution will be monitored.

Acknowledgement

We acknowledge Shweta MESHRAM (student) for the help on experiments, Pierre Belloeil (student) and Zonguyan Chen (PhD) for the preparation of clays, Dr Yassine El Mendili for the Rietveld refinement, Dr Jebril Hadi and Dr Christophe Tournassat for the method of purification of clays, and Dr Jean-Pierre Regoin for the granulometry.

The research leading to these results has received funding from the European Union's European Atomic Energy Community's (Euratom) Seventh Framework Program FP7-Fission-2010 under grant agreement number 269688 (CP-SKIN).

References

ANDRA (2005). Dossier ANDRA argile: Evaluation de la faisabilité du stockage géologique en formation argileuse

Bauer, A. and Berger, G. (1998). Kaolinite and smectite dissolution rate in high molar KOH solutions at 35° and 80°C. Applied Geochemistry, 13, 905–916

Bergaya, F., Theng, B.K.G., Lagaly, G. (2006). Handbook of Clay Science, Developments in Clay Science. Elsevier, Amsterdam

De Cannière, P., Moors, H., Dierckx, F., Gasiaux, F., Aertsens, M., Put, M., Van Iseghem, P. (1998). Diffusion and Sorption of ^{32}Si-labelled silica in the boom clay. Radiochimica Acta, 82, 191–196

Daux, V., Guy, C., Advocat, T., Crovisier, J.-L., Stille, P. (1997). Kinetic aspects of basaltic glass dissolution at 90°C: role of aqueous silicon and aluminium. Chemical Geology, 142, 109–126

Ganor, J., Mogollón, J.L., Lasaga, A.C. (1995). The effect of pH on kaolinite dissolution rates and on activation energy. Geochimica Cosmochimica Acta, 59, 1037–1052

Gaucher, E., Robelin, C., Matray, J.M., Négrel, G., Gros, Y., Heitz, J.F., Vinsot, A., Rebours, H., Cassagnabère, A., Bouchet, A. (2004). ANDRA underground research laboratory: interpretation of the mineralogical and geochemical data acquired in the Callovian-Oxfordian formation by investigative drilling. Physics and Chemistry of Earth, Parts A/B/C 29, 55–77

Huertas, F.J., Caballero, E., Jiménez de Cisneros, C., Huertas, F., Linares, J. (2001). Kinetics of montmorillonite dissolution in granitic solutions. Applied Geochemistry, 16, 397–407

IUPAC (1990). Compendium of Chemical Terminology, 2nd ed. (the "Gold Book"). Compiled by A. D. McNaught and A. Wilkinson. Blackwell Scientific Publications, Oxford (1997)

Köhler, S.J., Dufaud, F., Oelkers, E.H. (2003). An experimental study of illite dissolution kinetics as a function of ph from 1.4 to 12.4 and temperature from 5° to 50°C. Geochimica Cosmochimica Acta, 67, 3583–3594

Lutterotti L. (2000). MAUD program, CPD, Newsletter (IUCr) No. 24. 2000, http://www.ing.unitn.it/~maud/.

McHale J.M., Auroux A., Perrotta A.J., Navrotsky A. (1997). Science, 1997, 277, 788.

Palandri, J.L. and Kharaka, Y.K. (2004). A compilation of rate parameters of water-mineral interaction kinetics for application to geochemical modelling, US GEOLOGICAL SURVEY

Rozalén, M., Huertas, F.J., Brady, P.V. (2009). Experimental study of the effect of pH and temperature on the kinetics of montmorillonite dissolution. Geochimica Cosmochimica Acta, 73, 3752–3766.

Suzuki-Muresan, T., et al. (2011). Solution controls for dissolved silica at 25°, 50° and 90°C for quartz, Callovo-Oxfordian claystone, illite and MX80 bentonite. Physics and Chemistry of the Earth, Parts A/B/C 36(17-18): 1648-1660

van den Boorn, S. H. J. M., P. Z. Vroon, C. C. van Belle, B. van der Wagt, J. Schwieters, M. J. van Bergen (2006). Determination of silicon isotope ratios in silicate materials by high-resolution MC-ICP-MS using a sodium hydroxide sample digestion method. Journal of Analytical Atomic Spectrometry, 21(8): 734-742

DIFFUSION AND ADVECTION IN CEMENTITIOUS MEDIA

John Hinchliff*, Nick Evans, Monica Felipe Sotelo

Loughborough University (UK)

* Corresponding author: cmjh5@lboro.ac.uk

Abstract

A series of diffusion and advection experiments have been undertaken and examples are presented where significant results have been obtained. In the diffusion experiments the effect of cellulose degradation products on the mobility of strontium is investigated and an illustration of isotope exchange as a mechanism for calcium migration is described. The advection experiments required the development and manufacture of a purpose designed cell, the new cell is described and the preliminary results for H-3, Sr-90 and Ca-45 are presented.

Introduction

This paper describes a few examples from a series of diffusion and advection experiments. These dynamic experiments aim to understand the interaction between cementitious media and radionuclides relevant to the geological disposal of radioactive waste.

The cementitious media being studied are NRVB (Nirex Reference Vault Backfill) and a waste packaging grout containing PFA (pulverised fuel ash). The results for the PFA grout will not be available until mid-2013 so the discussion here concentrates on the NRVB experiments. The radionuclides being studied are Sr-90, Ca-45, Am-241, Eu-152 and Se-75. In addition a small amount of work has been undertaken investigating the effect of CDP (cellulose degradation products) and the mobility of Sr-90.

1. Diffusion Experiments

The experimental set up was described in the review of the first year of WP2.

The Sr-90 and Ca-45 experiments produce results relatively quickly and details are provided below. The Eu-152 and Am-241 experiments are being left to run for the maximum amount of time and will be concluded mid to late 2013. The Se-75 experiments will commence early 2013.

Sr-90: Diffusion

The radial diffusion experimental technique uses small pre-cast cylinders of the cementitious matrix under investigation, in this case, NRVB. An appropriate concentration of Sr-90 is introduced into a cavity in the centre of the cylinder, which is then sealed and placed in a

solution previously equilibrated with the solid matrix. The increase in concentration of the isotope in the external solution is then determined at defined time intervals. Radial diffusion experiments on NRVB have been undertaken using Sr-90 in the presence and absence of CDP or gluconate (a surrogate for the CDP mixture).

The Sr-90 diffusion experiments proceeded fast enough to be monitored via the build of concentration in the surrounding solution. Figures 7-9 below show the results of the experiments. The effect on the migration of Sr-90 caused by addition of CDP is seen to be significant at tracer concentrations where, contrary to expectations, migration was significantly slowed. The effect was not evident in the carrier experiments when a higher concentration of non-active Sr was used. The use of gluconate as a potential surrogate for the CDP had no discernible effect on Sr migration.

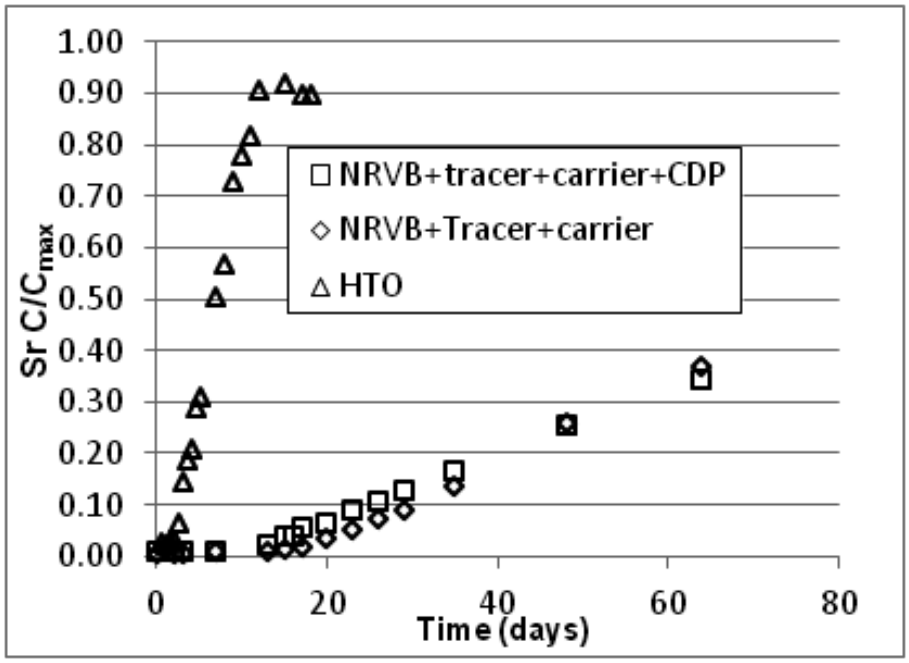

Figure 7: *Results using Sr carrier and Sr-90 tracer*

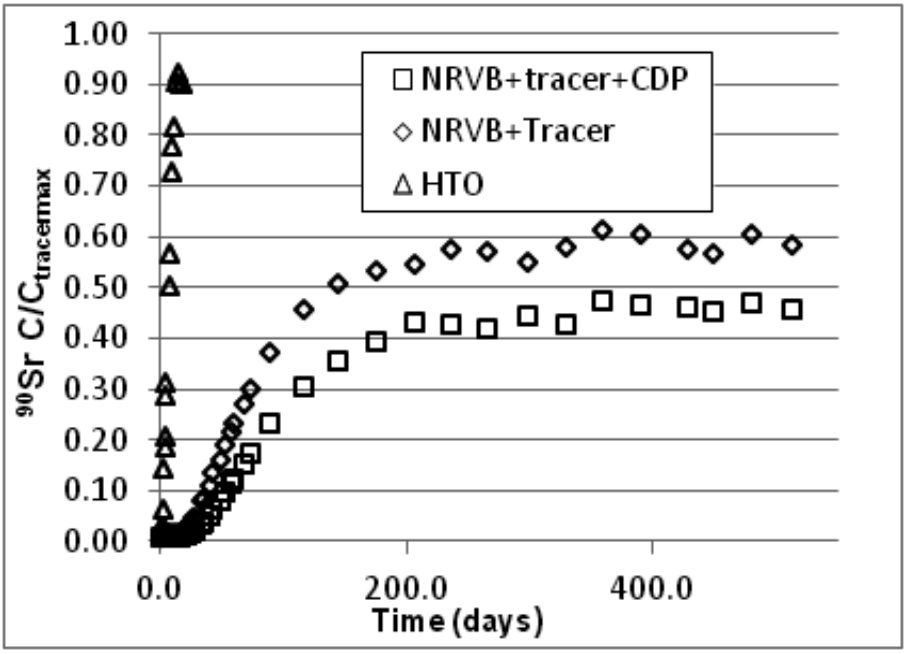

Figure 8: *Results using Sr-90 tracer only*

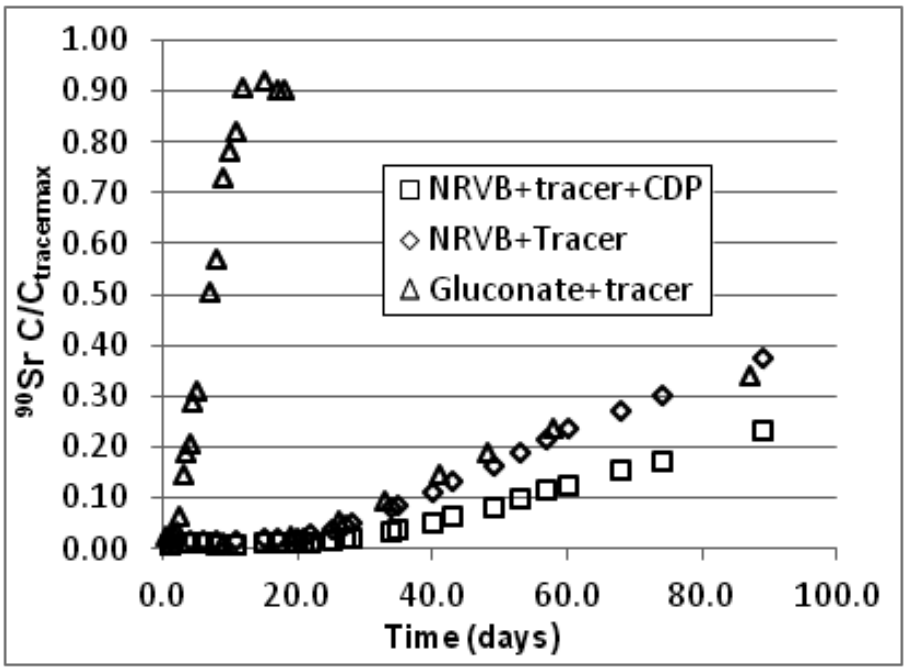

Figure 9: *Results using gluconate instead of CDP*

The slowing of Sr migration could be due to the formation of a ternary complex between a component of the CDP, the surface of the cement matrix and Sr, or enhanced ion exchange with calcium in the cement phases in the matrix. The results demonstrate that gluconate is not a suitable surrogate for CDP in this type of experiment.

Ca-45 Diffusion

There had been an expectation to observe some mobility of calcium in the cementitious systems being investigated primarily because calcium is present in high concentration in both solid (> 25% w/w) and solution (~800 ppm or ~ $2x10^{-2}$ mol dm^{-3}). However the addition of Ca-45 was so small in comparison that isotope exchange would be the only migration mechanism observed.

The short half-live of Ca-45 (163 days) could also represent a problem if mobility was slow. After one year, and with no breakthrough of Ca-45, one of the NRVB experiments was stopped and the cylinder sectioned for autoradiography. This was done because of the need to establish whether the decay of Ca-45 had rendered it difficult to detect on the autoradiography plates. The resulting images are shown below.

It is clear that Ca-45 has moved into the NRVB matrix from the central core, penetration appears to be several millimetres. The image of the activity in the matrix (Figure 10) has been made clearer by screening, with a plastic plug (absorbing the beta radiation from Ca-45 decay), the much higher activity present on the surface of the core. The unshielded autoradiograph and intensity plot are shown below.

It should be noted that the intensity plots are not calibrated and it is only possible to infer relative concentrations (Figure 11). The unshielded figures demonstrate that a significant proportion of the Ca-45 has remained on the inner walls of the central core. Additionally the 2 cm^3 of solution remaining in the core when the experiment was halted, was removed and analysed by liquid scintillation counting and the Ca-45 activity concentration was found to be at background.

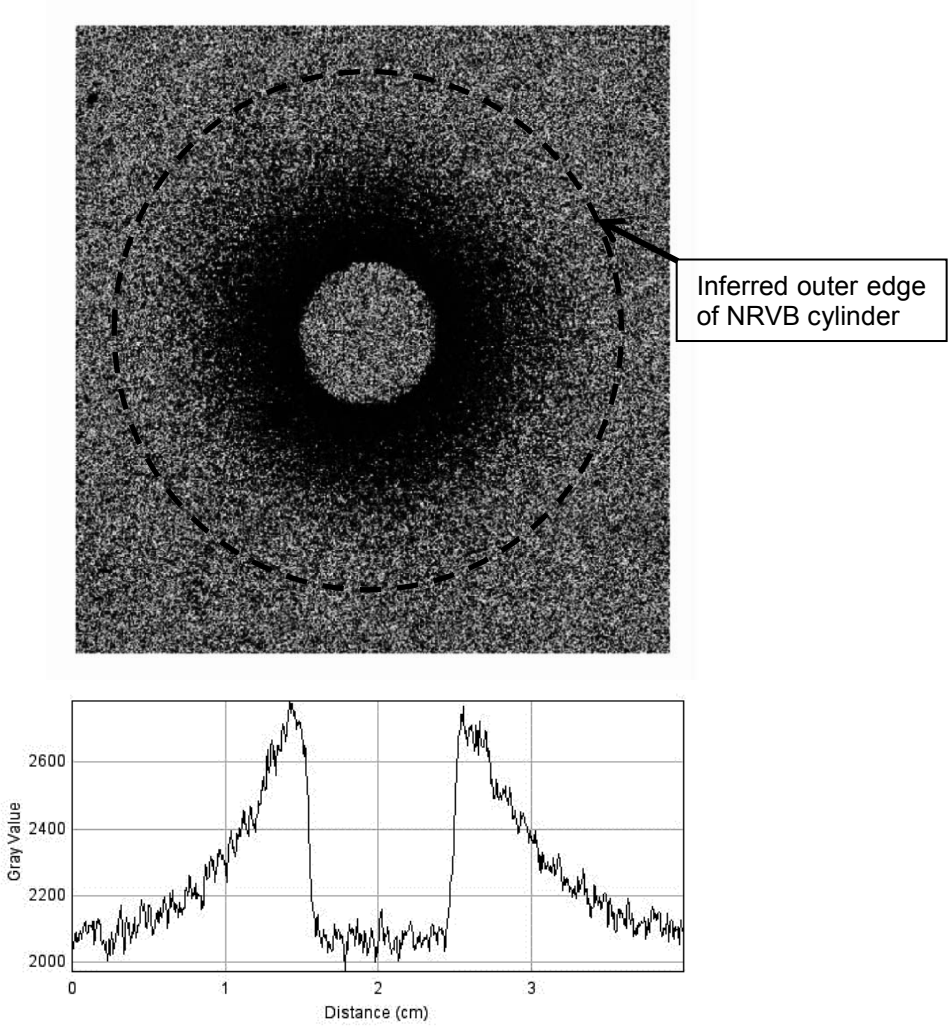

Figure 10: *Autoradiograph and intensity plot of NRVB cylinder from the Ca-45 diffusion experiments (central core "plugged" to shield highest activity at inner walls).*

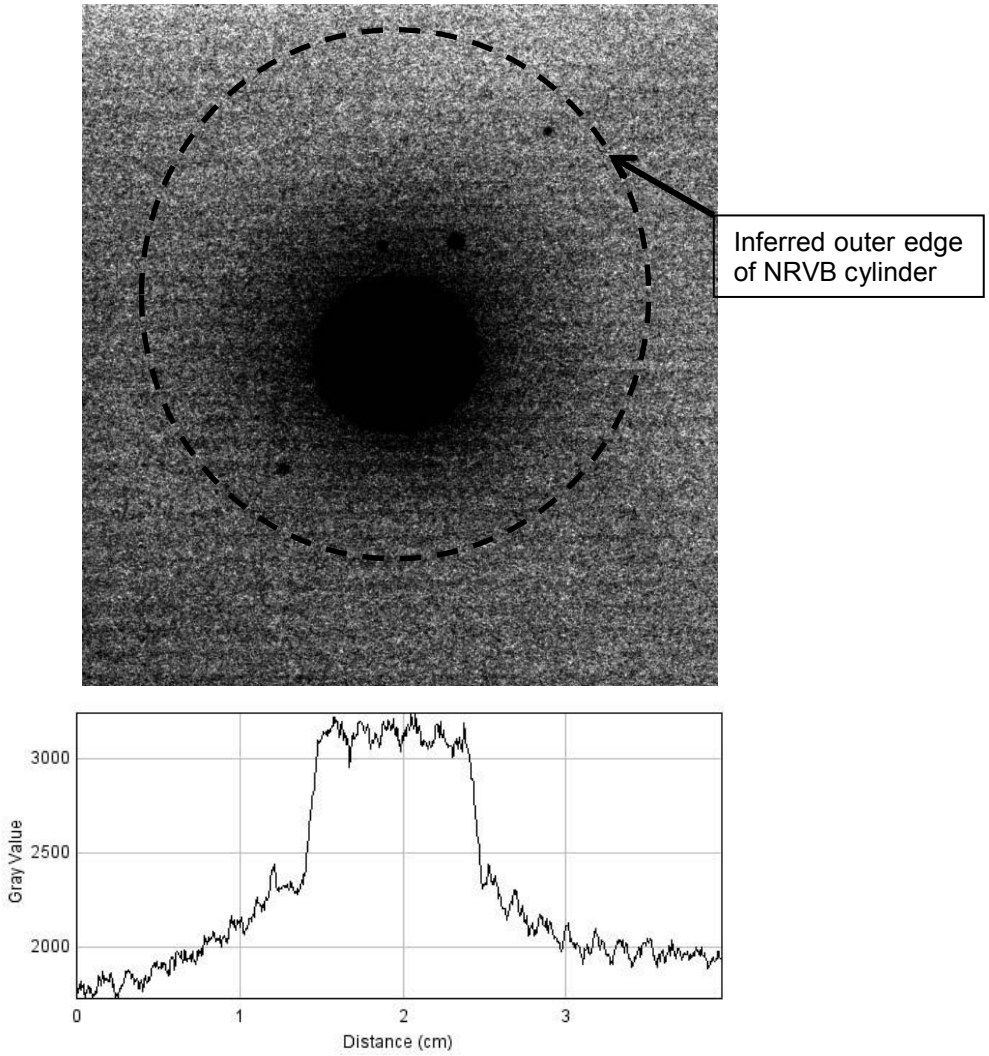

Figure 11: *Autoradiograph and intensity plot of NRVB cylinder from the Ca-45 diffusion experiments (central core "unshielded" to show highest activity at inner walls)*

2. Advection Experiments

A radial advection apparatus has been designed and manufactured and is now operational. Initial results for H-3 Sr-90 and Ca-45 have been obtained. The photographs below show the main parts dismantled and the completed set up. The apparatus has been manufactured to enable testing of cementitious cylinders with similar dimensions those used in the diffusion experiments. The "eluent" is pushed from the steel reservoir through the cylinder using N_2 pressure. The whole system is effectively closed to O_2 and CO_2 ingress up to the end of the sample collection tube where interaction with the atmosphere is limited by the small internal diameter of the teflon tubing.

Figure 12: *Photographs of the advection apparatus*

The HTO and Sr-90 and Ca-45 plots below show that good progress is being made and the results are in line with expectations. Flow rate control using N_2 pressure remains an issue. The "step" changes and data gaps observed in the results were generally associated with interventions e.g. refilling the reservoir, changing the gas bottle or clearing blocked tubing.

2.1 H-3 Advection

Figures 13 and 14 below show the results of the H-3 advection experiment. H-3 provides the conservative case where sorption to the solid phase should be at a minimum and mobility in the liquid phase maximised. It can be seen that the experiment proceeds quickly and that over 85% of the H-3 injected is recovered.

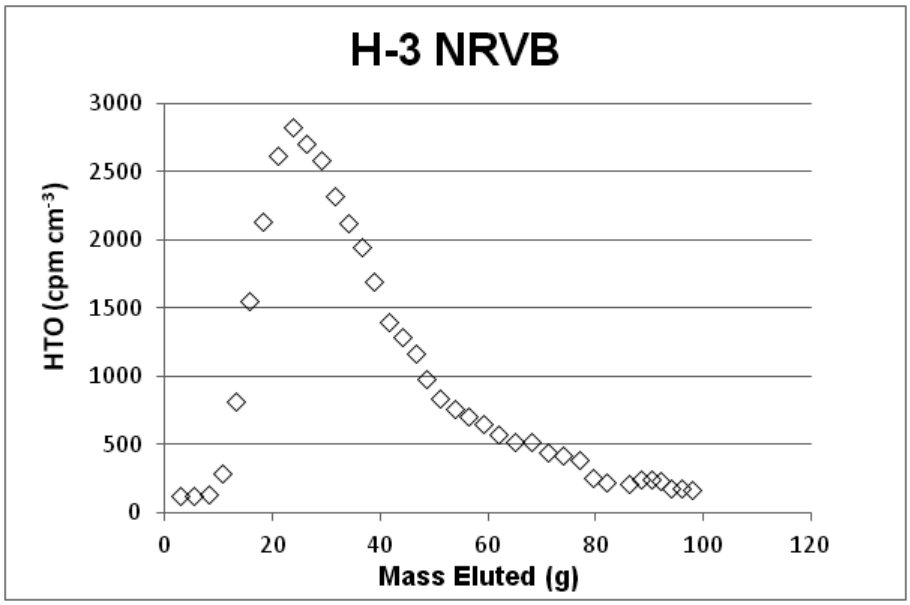

Figure 13: *Graph showing advection of H-3 through NRVB*

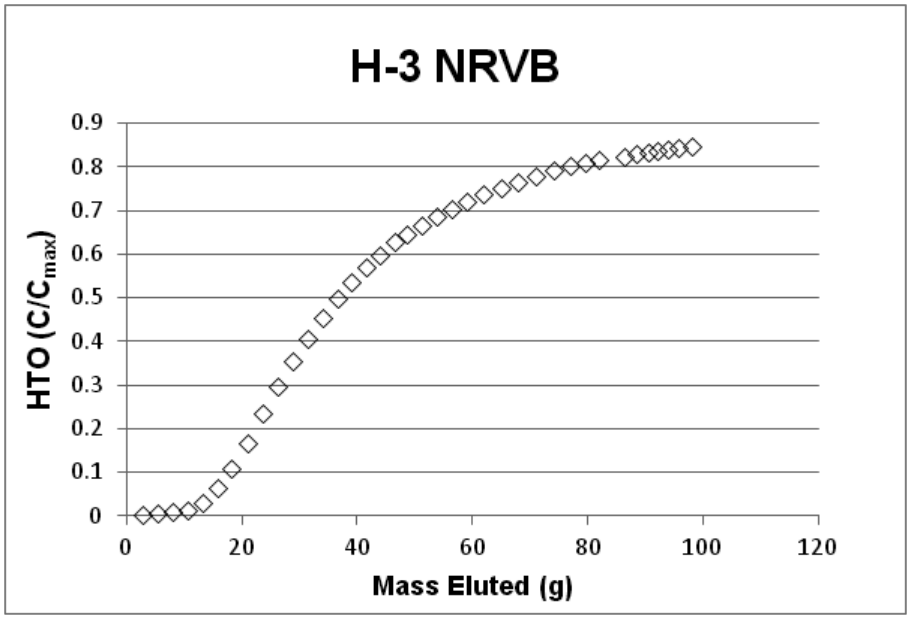

Figure 14: *Graph showing cumulative H-3 results*

2.2 Ca-45 Advection

Figures 15 and 16 below show the results of the Ca-45 advection experiment. The contrast to the H-3 results is marked with 50-60 times more eluent being required prior to breakthrough being observed. The recovery of Ca-45 is much reduced when compared to H-3 and although the experiment is not yet completed it can be seen that a recovery of ~35% could be reasonably anticipated.

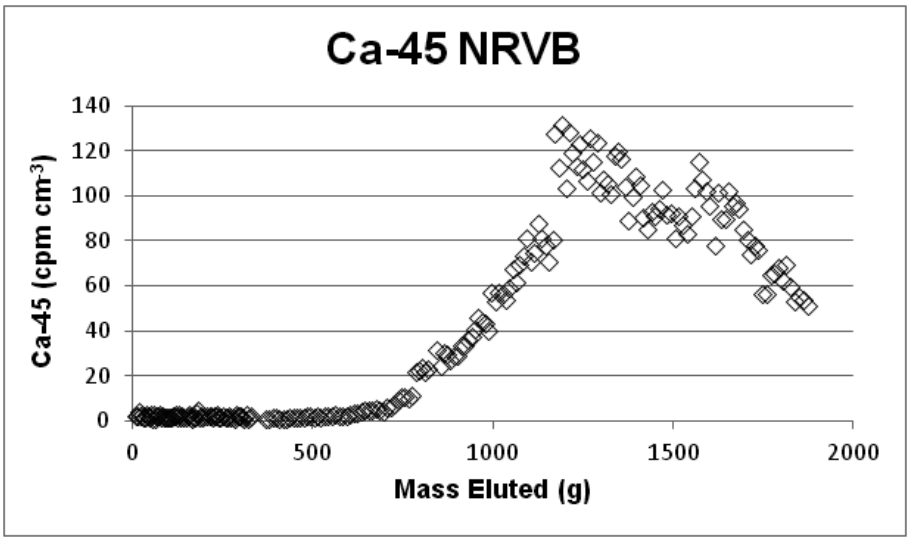

Figure 15: *Graph showing advection of Ca-45 through NRVB*

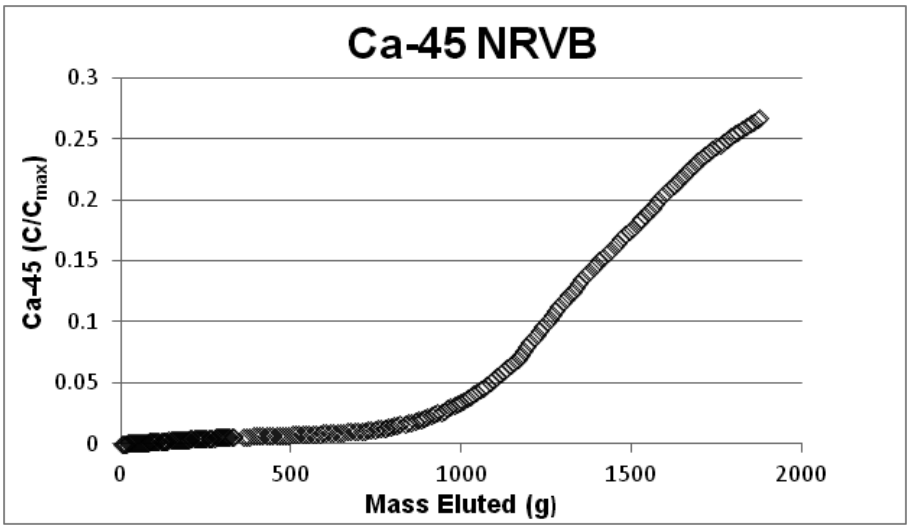

Figure 16: *Graph showing cumulative Ca-45 results*

2.3 Sr-90 Advection

Figures 17 and 18 below show the results of the Sr-90 advection experiment. The results are different to both the H-3 and Ca-45 results. The recovery of Sr-90 is ~85% similar to H-3 and very different to Ca-45.

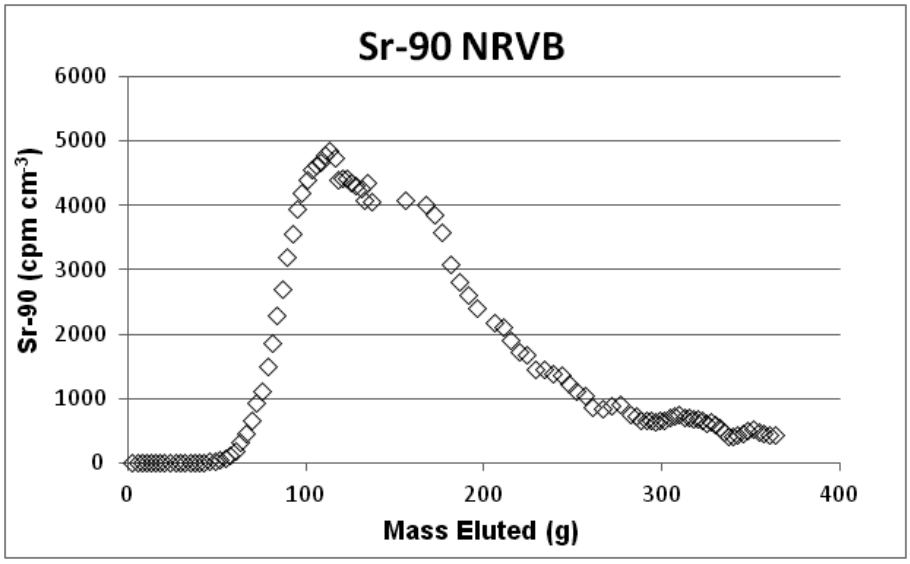

Figure 17: *Graph showing advection of Sr-90 through NRVB*

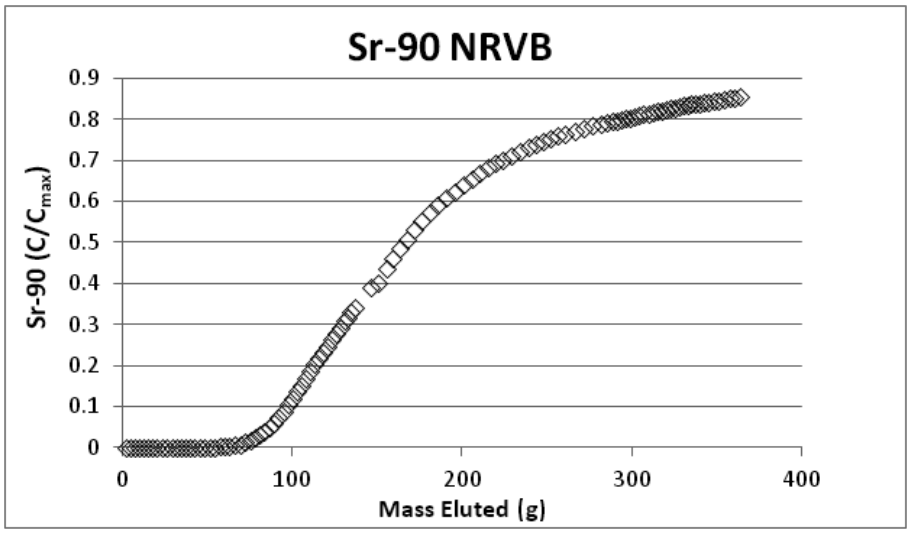

Figure 18: *Graph showing cumulative Sr-90 results*

2.4 Advection – concluding remarks

The advection experiments show that there are clear differences in mobility between the radionuclides tested. As expected, H-3 behaved conservatively being subject primarily to dispersion it moved very quickly through the cylinder (although the long "tail" suggests some interaction with the NRVB matrix). The comparison between Sr-90 and Ca-45 is significant and both radionuclides are retained to a much greater extent than H-3. The Ca-45 results indicate a strong interaction with the NRVB which is most likely due to a combination of isotope exchange and solubility limitation. The Sr-90 results indicate higher mobility than Ca-45 and a less significant interaction with the solid matrix. Isotope exchange with Ca in the solid matrix will be less efficient for Sr-90 than Ca-45 and the solubility of Sr is not limited in the system.

Future work

Future work includes:

- Undertaking similar experiments using a PFA waste packaging grout.
- Advection experiments on "doped" cement blocks for Am-241.
- Modelling and comparison of diffusion and advection.
- Visualisation of the Sr migration using Sr-82/Rb-82 pair and a PET scanner.

Acknowledgement

The research leading to these results has received funding from the European Union's European Atomic Energy Community's (Euratom) Seventh Framework Program FP7-Fission-2010 under grant agreement number 269688 (CP-SKIN).

References

Abdullah M. Alshamsi and Hassan D. A. Imran; *Development of a permeability apparatus for concrete and mortar*. Cement and Concrete Research Volume 32, Issue 6, June 2002, Pages 923-929.

Evans N D M. *Binding mechanisms of radionuclides to cement*. Cement and Concrete Research Volume 38, Issue 4, April 2008, pages 543-553

Francis, A J, Cather, R, and Crossland, I G, *Development of the Nirex Reference Vault Backfill; report on current status in 1994*, Nirex Science Report S/97/014, UK Nirex Ltd., Harwell, UK, 1997.

Jakob A, *Diffusion of tritiated water (HTO) and 22Na+-ions through non-degraded hardened cement pastes – II. Modelling results*. PSI-Bericht Nr. 02-21 December 2002.

Andersson K, Torstenfelt B. Allard B: *Sorption and diffusion studies of Cs and I in concrete* Department of Nuclear Chemistry Chalmers University of Technology Göteborg, Sweden January 1983

Mibus J, Sachs S, Pfingsten W, Nebelung C, Bernhard G, *Migration of uranium(IV)/(VI) in the presence of humic acids in quartz sand*: A laboratory column study. Journal of Contaminant Hydrology 89 (2007).

M.M. Askarieh, A.V. Chambers, F.B.D. Daniel, P.L. FitzGerald, G.J. Holtom, N.J. Pilkington, J.H. Rees. *The chemical and microbial degradation of cellulose in the near field of a repository for radioactive wastes.* Waste Management 20 2000 pp 93-106.

Pala´gyi S, Tamberg K S, Vodickova H; *Transport and sorption of Sr-85 and I-125 in crushed crystalline rocks under dynamic flow conitions*. Journal of Radioanalytical Nuclear Chemistry 2010 page 283

Tits J, Wieland R, Bradbury M H; *The effect of isosaccharinic acid and gluconic acid on the retention of Eu(III), Am(III) and Th(IV) by calcite*. Applied Geochemistry 20 November 2005 Volume 20, Issue 11 pages 2082-2096

Rowe P W, Barden L; *A new consolidation cell*. Géotechnique, Vol. 16, No. 2, 1966, pages 116-124.

INTERACTION BETWEEN URANIUM AND IRON (III) OXIDES

Mireia Grivé[1*], Elisenda Colàs[1], Alba Valls[1], Lara Duro[1]

[1] Amphos 21 (SPAIN)

* Corresponding author: mireia.grive@amphos21.com

Abstract

The objectives of this work are to study the nature and long term processes of the interaction between uranium and iron oxides, linking short-term and long-term processes.

Ferrihydrite samples coprecipitated with U(VI) at different wet and dry ageing periods, have been analysed using conventional solution techniques and several spectroscopic techniques such as XRD, EXAFS and μ-XRF.

The preliminary conclusions obtained so far indicate that the Fe(III)-U(VI) coprecipitates have a ferrihydrite-like structure that evolves with ageing time. Spectroscopic measurements are consistent with a re-arranging of the uranium content of the samples towards a schoepite-like structure. This would have some implications on the assessment of the efficiency of uranium retention process, which would be given by the schoepite solubility limit at long time frames. The study of the influence of carbonate in the overall process is on-going.

Introduction

Iron oxides are present in nature and also in the near and far field of the repository; they are formed from oxidation of canister corrosion products and are ubiquitous among the engineered and geological barriers. Among the iron oxides, the amorphous ferrihydrite is one of the most widespread iron solids and an important precursor of more stable and crystalline iron oxides. Ferrihydrite is a poorly ordered iron oxide and exists as 2-line and 6-line ferrihydrite, because of the number of reflections shown in their respective XRD patterns ***(Cornell and Schwertmann, 2003)***.

Ferrihydrite evolution with time and the final products formed depend on many factors, such as pH, time, temperature, etc. The presence of foreign species in the system will affect the ferrihydrite ageing process. Those foreign species can a) modify the rate of transformation, usually by slowing the process, and/or b) change the composition and properties of the end product ***(Cornell and Schwertmann, 2003)***.

The ageing and transformation process of ferrihydrite will in turn affect the solubility and the retention/release of uranium from the coprecipitates ***(Bruno et al., 1995, Duro, 1996)***.

Carbonate, that has a high affinity towards both, U and Fe, is expected to influence significantly the overall process.

The objective of this work is to deepen in the understanding of bounding processes between uranium and iron oxides at long time frames, in order to evaluate the role of these solids in the retention and release of uranium from the repository.

1. Experimental

Fe(III)-U(VI) coprecipitates were prepared from $Fe(NO_3)_3 \cdot 9H_2O$ and $UO_2(NO_3)_2 \cdot 6H_2O$ solutions. Initial concentrations were [Fe]≈0.01 M and [U(VI)]≈10^{-4} M at pH=5.5, that is, initial uranium concentrations were below theoretical schoepite solubility limit. Afterwards, the samples were aged in solution for periods between 1 day and 5 weeks. The solids were then collected and let to age in dry state for periods between some days to 11 years previous to the analysis.

All the process (preparation, wet aging and dry aging) were carried out at room temperature, so that thermal transformations are not expected to occur.

The analysis of the solutions indicated that the uranium content in the coprecipitates was ≈1-2%.

Different spectroscopic techniques were used in order to characterize the precipitates:

- X-ray diffraction analyses (XRD) were performed in the X-ray laboratory of Institut de Ciències de la Terra Jaume Almera (CSIC) and in the X-ray diffraction service of the Universitat Autònoma de Barcelona (UAB).
- Iron Extended X-Ray Absorption Fine Structure analyses (EXAFS) were performed using the Fe K-edge signal in the A1 Beamline at the German Electron Synchrotron facility (DESY/Hasylab) in Hamburg. Spectra were collected in transmission mode at room temperature.
- Uranium EXAFS analyses were performed using the U LIII-edge in the Rossendorf Beamline (ROBL) at the European Synchrotron Radiation Facility (ESRF) in Grenoble. Spectra were collected in fluorescence mode at room temperature.
- Micro X-ray fluorescence analyses (μ-XRF) were performed in the L Beamline at the German Electron Synchrotron facility (DESY/Hasylab) in Hamburg.

EXAFS scans were collected, pre-treated and averaged using Sixpack ***(Webb, 2005)***. Data analysis was performed using the EXAFSPAK ***(George and Pickering, 1995)*** or the WinXAS ***(Ressler, 1998)*** software. Theoretical scattering amplitudes for each absorber and backscattered pair were calculated with the FEFF 8.20 code ***(Rehr and Albers, 2000)***.

μ-XRF data treatment was done using PyMca ***(Solé et al. 2007)***.

2. Results

2.1 The effect of uranium in the ferrihydrite ageing process

Results of iron EXAFS analyses using the Fe K-edge signal for samples aged 1 week, 3 week and 7 years are shown in Figure 34. The bulk solids were shown to have a ferrihydrite-like structure. The spectra of the samples aged for 1 and 3 week resemble that of a 2-line ferrihydrite (in comparison with the EXAFS data reported by ***Toner et al. 2009)***. Nevertheless, the spectrum of the 7 years sample has some distinct features (different line shape and amplitudes in the Fe-Fe shell) indicating the evolution towards a 6-line ferrihydrite.

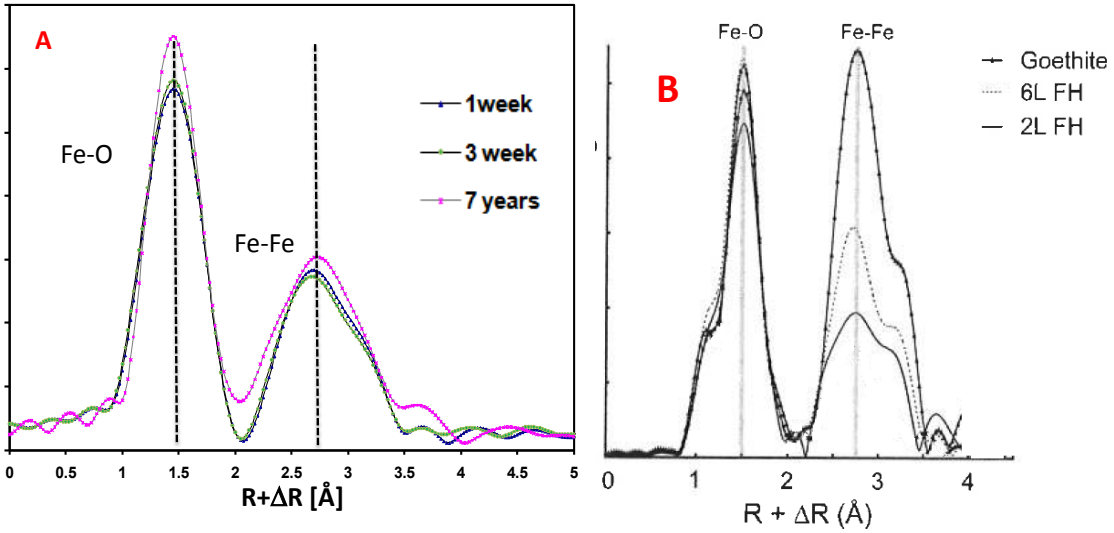

Figure 34: *A) Results of the EXAFS Fe K-edge measurements for samples aged 1 week, 3 weeks and 7 years respectively. B) EXAFS Fe K-edge spectra for goethite, 6-line ferrihydrite and 2-line ferrihydrite reported by* ***Toner et al. (2009)****. The spectra are provided for comparison purposes.*

The evolution of the coprecipitates was also confirmed with XRD. As shown in Figure 35, the XRD spectrum for a sample aged 3 weeks was similar to that of a 2-line ferrihydrite. On the contrary, the spectrum of a 9 years aged sample resembled that of a 6-line ferrihydrite.

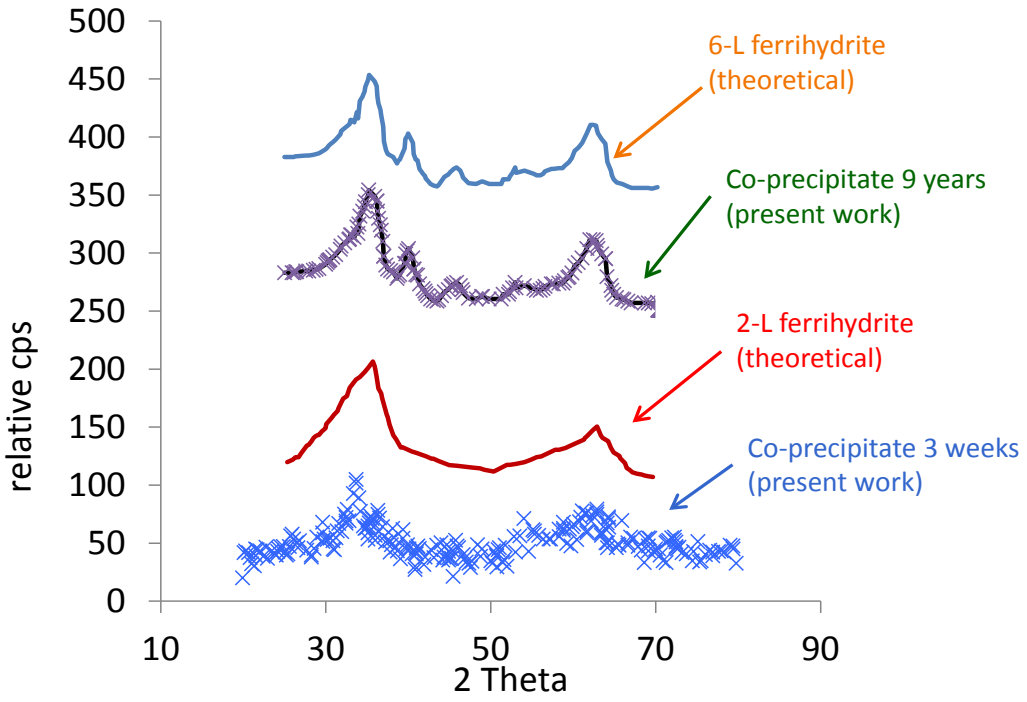

Figure 35: *Crosses: Results of the XRD measurements for samples aged 3 week and 9 years (present work). Solid lines: XRD spectra for 2-line (red) and 6-line (blue) ferrihydrite, from* ***Zhao et al. (1994)****.*

It may then be concluded that the presence of uranium has an influence on the ferrihydrite internal ordering. Although goethite and hematite are the most common ferrihydrite transformation products described in the literature ***(Cornell and Schwertmann, 2003)***, the evidences obtained in present work indicate an evolution from a 2-line ferrihydrite towards a 6-line ferrihydrite without goethite neither hematite formation. This change in the expected products is probably consequence of the presence of uranium in the solid. This type of transformation (from 2-line to 6-line ferrihydrite) has also been described in ***Kukkadapu et al. (2003)*** due to the presence of other foreign cation (nickel) in the system.

2.2 The effect of ageing in the retention of uranium in the coprecipitates

The ageing process of the coprecipitates and the evolution of the bulk solid structure are expected to have an influence on the retention of uranium within them. EXAFS analyses using the U L_{III}-edge signal for samples aged from 1 day to more than 10 years were performed to investigate this process. Some slight differences are observed in the spectra as the ageing time of the coprecipitates increases (see Figure 36), suggesting that the uranium environment might change with time.

The uranium EXAFS spectrum of the coprecipitates shows several coordination shells (Figure 37):

- The first coordination shell corresponds to the two axial oxygen atoms (O_{ax}) of the uranyl group. This is the most intense feature in the spectrum.
- The second coordination shell corresponds to the uranium interaction with oxygen atoms in the equatorial plane of the uranyl group (Oeq_1).
- The third coordination shell also seems to correspond to the uranium interaction with an oxygen in the equatorial plane (Oeq_2). The distance between uranium and this atom seems to progressively decrease with the ageing time of the co-precipitate sample, moving closer to the distance of that corresponding to schoepite.
- Preliminary fittings also indicate that the U-Fe distances observed in the U(VI)-Fe(III) co-precipitates (fourth coordination shell) are consistent with an edge-sharing bond between U(VI) and ferrihydrite. The U-Fe coordination number decreases with time.
- U-U interaction (fifth coordination shell) is difficult to appreciate in some of the spectra, due to noisy background and the long interaction distances between those atoms. However, the U-U distance seems to decrease with the aging time, getting close those U-U distances in schoepite. Furthermore, preliminary fits also point out that the U-U coordination number could increase with time.

Those measurements are consistent with a re-arranging of the uranium content towards a schoepite-like structure.

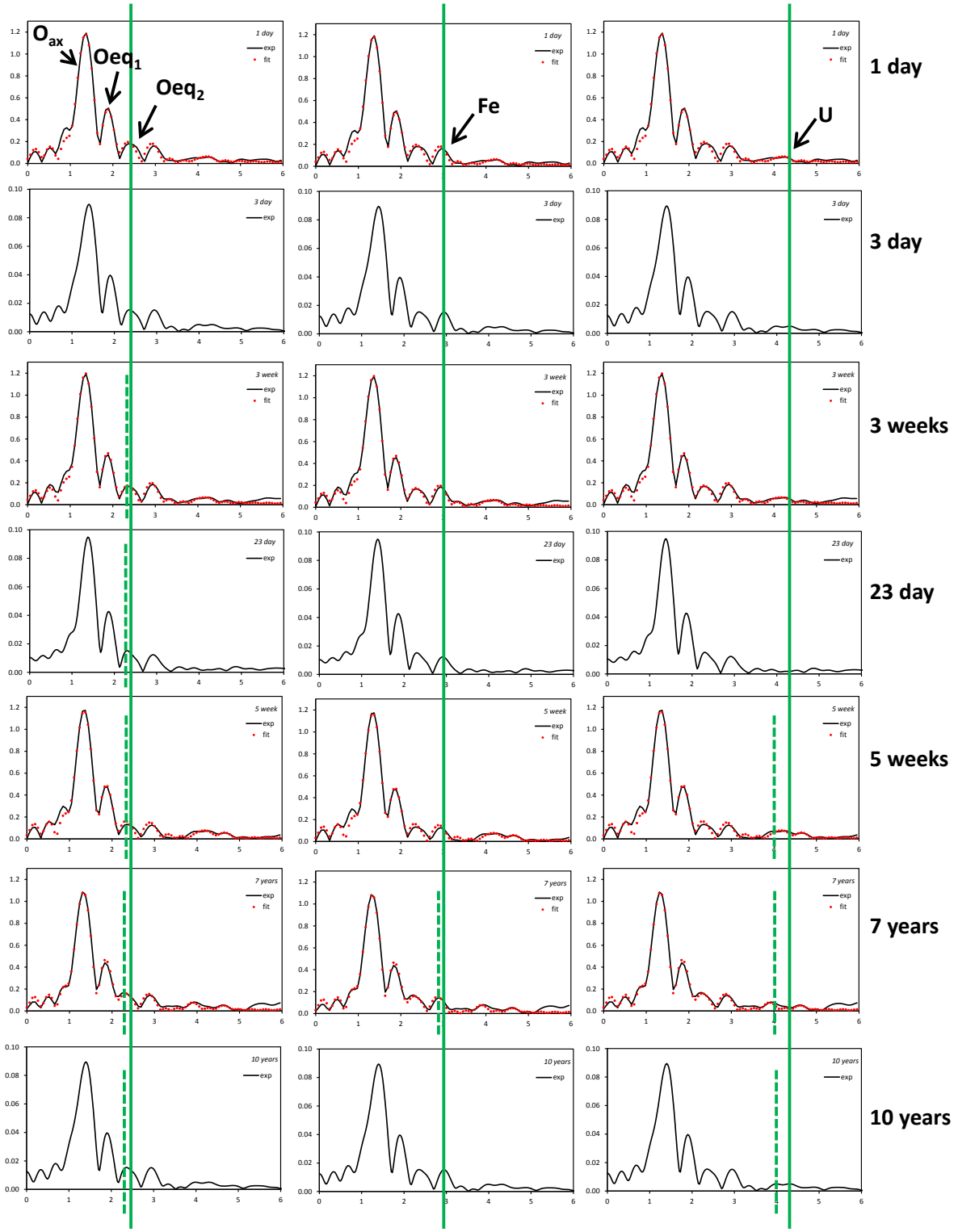

Figure 37: *Results of the EXAFS U L_{III}-edge measurements for U(VI)/Fe(III) coprecipitates at different ageing times. Solid black lines are experimental data; red dots indicate fittings (when available). Green lines indicate peak displacement (see text).*

In order to observe the distribution of the elements (Fe, U) in the different ageing samples µ-XRF analyses were performed. The results are shown in Figure 38.

As shown in the µ-XRF results, the samples are highly heterogeneous. There is also a strong correlation between the zones where high iron concentrations are measured and the zones where high uranium concentrations are observed.

Uranium measurements are consistent with a regrouping of the uranium content as ageing time increases, being the difference most significant in the 11 years aged sample (Figure 38) when compared with samples aged for 3 or 23 days.

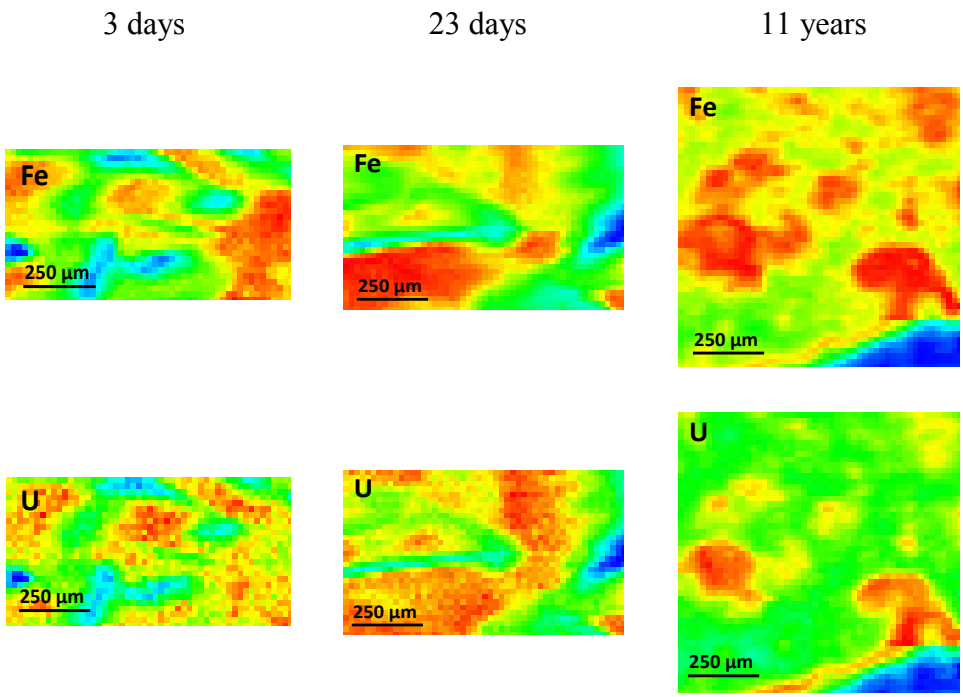

Figure 38. *Results of the µ-XRF measurements for U(VI)/Fe(III) coprecipitates at different ageing times. Up) Iron. Down) Uranium. Colors provide a qualitative indication of the concentration of the different elements in the samples (red: high concentration; blue: low concentration).*

Summarizing, the analyses have shown that the retention of U(VI) within the ferrihydrite structure remains effective after 5 weeks of suspension and after 11 years of a dry-stored sample. Uranium is affected by the ageing process, and the results indicate a re-arranging of the uranium content towards a schoepite-like structure. This would suggest that the assessment of the efficiency of this retention process at long time frames could be governed by the schoepite solubility limit.

Conclusions and Future work

The Fe(III)-U(VI) coprecipitate has a ferrihydrite-like structure which evolves with time, from 2-line to 6-line ferrihydrite. The presence of uranium in the solid affects the ageing process, changing ferrihydrite reactivity towards internal ordering.

The retention of U(VI) within the solid has been shown to be effective after 5 weeks of suspension and after 11 years of a dry-stored sample. Uranium measurements are consistent with a re-grouping and re-arranging of the uranium content towards a schoepite-like structure.

Further data analysis of EXAFS U L_{III}-edge and μ-XRF results are still on-going in order to provide additional evidences that support those hypotheses.

The effect of pCO_2 on the dissolution rate of different solids (Fe(III)-U(VI)coprecipitates and the two end-members of the system, ferrihydrite and schoepite) is also being studied. First results point out a bicarbonate promoted dissolution of the co-precipitates, and allow the determination of an experimental dissolution rate. Further data evaluation and additional dissolution experiments, as well as the study of the dissolution reaction mechanisms, are on-going.

Acknowledgement

We acknowledge the ESRF and HASYLAB for provision of synchrotron radiation facilities and we would like to thank A. Rossberg, A. Scheinost, C. Hennig, M. Borchet and V. A. Solé for assistance in using beamlines ROBL (ESRF) and L (Hasylab) and for their help with data treatment.

The research leading to these results has received funding from the European Union's European Atomic Energy Community's (Euratom) Seventh Framework Programme FP7-Fission-2010 under grant agreement n° 269688 (SKIN project).

References

Bruno J., DePablo J., Duro L., Figuerola E. (1995). Experimental study and modeling of the U(VI)-$Fe(OH)_3$ surface precipitation/coprecipitation equilibria. Geochimica et Cosmochimica Acta, 59(20):4113–4123.

Bruno J., Wersin P., Stumm W. (1992). On the influence of carbonate in mineral dissolution:II. The solubility of $FeCO_3$(s) at 25ºC and 1 atm total pressure. Geochimica et Cosmochimica Acta 56, 1149-1155.

Cornell R. M., Schwertmann U. (2003). The iron oxides. Structure, properties, reactions, occurrence and uses. VCH, second edition edition.

Duro L. (1996). Estudio cinético y termodinámico de la interacción entre U(VI) y oxihidróxidos de Fe(III). PhD thesis, UB.

George G., Pickering, I. (1995) EXAFSPAK: A suite of computer programs for analysis of X-ray absorption spectra. Stanford synchrotron Radiation Laboratory, Standford, CA, USA.

Kukkadapu R., Zachara J., Fredrickson J., Smith S., Dohnalkova A., Russell C. (2003). Transformation of 2-line ferrihydrite to 6-line ferrihydrite under oxic and anoxic conditions. American Mineralogist, 88(11-12):1903–1914.

Rehr J.J., Albers R.C. (2000) Theoretical approaches to X-ray absorption fine structure. Reviews of Modern Physics, 72, 621-654.

Ressler T. (1998) WinXAS: a program for X-ray absorption spectroscopy data analysis under MS-Windows. Journal of Synchrotron Radiation, 5, 118-122.

Solé V.A., Papillon E., Cotte M., Walter Ph., Susini J. (2007) A multiplatform code for the analysis of energy-dispersive X-ray fluorescence spectra, Spectrochimica Acta Part B 62 63-68.

Toner B.M., Santelli C.M., Marcus M.A., Wirth R., Chan C.S., McCollom T., Bach W., Edwards K.J. (2009) Biogenic iron oxyhydroxide formation at mid-ocean ridge hydrothermal vents: Juan de Fuca Ridge. Geochimica et Cosmochimica Acta 73(2), 388-403.

Webb S.M. (2005) SIXPack: a graphical user interface for XAS analysis using IFEFFIT. Physica Scripta, T115, 1011.

Zhao J., Huggins F. E., Feng Z., Huffman G. P. (1994) Ferrihydrite: surface structure and its effects on phase transformation. Clays and Clay Minerals 42(6), 737-746.

THORIUM OXIDE SOLUBLITY BEHAVIOR VS. THE SURFACE CRYSTALLINE STATE

Johan Vandenborre[1*], Tomo Suzuki-Muresan[1], Katy Perrigaud[1], Bernd Grambow[1]

[1] SUBATECH, Unité Mixte de Recherche 6457, Ecole des Mines de Nantes, CNRS/IN2P3, Université de Nantes, 4 rue Alfred Kastler, BP 20722, 44307 Nantes cedex 03, France

* Corresponding author: johan.vandenborre@subatech.in2p3.fr.

Abstract

The aim of this task is to study the solubility of ThO_2(s) in the pH range 3 to 7. Previous studies indicated that thorium oxide solubility is very much dependent on the material at the grain boundary. With the use of powdered material, the cleaning of the surface is expected to be more effective, so that artifacts derived from pre-altered surface phases will be minimised. The attainment of apparent solubility equilibrium will be followed by analysing ^{232}Th with time and after equilibration half of the solution will be removed for subsequent desorption studies, ^{229}Th traces will be added to the remaining solution/solid system and the experiment will be continued until establishment of constant ^{229}Th concentrations. In all solution analyses, colloids will be removed by ultra-filtration but Th analyses of colloidal material will be included in the mass balance. Once ^{229}Th uptake on the surface has reached a steady state, desorption experiments will be performed putting the solids with a ^{229}Th rich surface into the previously conserved solution without ^{229}Th. Typical duration of experiments is shorter than a year. Different analytical techniques will be used for solution and solid analyses: ICP-MS, SEM, XRD, BET method.

Synthesis of the solid oxide has been performed with different calcinations temperatures (ambient, 700 °C, 900 °C, 1300 °C) in order to obtain 4 crystallizations of oxide Thorium with different grains vs. grain boundaries ratio. Also separation of ThO_2 crystallized kernel from the coating layers of HTR of ThO_2 has been conducted. These two methodologies have provided samples of the oxide with different crystallinity, i.e., grain size.

Solubility measurements have been conducted in the acidic pH range and the results compared with available data in the literature.

Introduction

We study Th atom exchange between different thorium oxide surfaces and aqueous solution (0.01 $molL^{-1}$ NaCl for pH = 3.2, 5.0, 6.8) to address the Task 3.2. In a previous work ***(Vandenborre et al., 2010)***, we have determined by the solid-state characterization (XPS, SEM, AFM) that 80 % of the XPS accessible near surface region of sintered thorium oxide is represented by the less reactive ThO_2(cr) grains. The remaining 20 % corresponds to

$ThO_x(OH)_y(H_2O)_z$ which is largely associated with grain boundaries. The empirical solubility data does not correspond to thermodynamic bulk phase/solution equilibrium, as measured solution concentrations are controlled by specific site exchange mechanisms at the solid/solution interface. Therefore for sparingly soluble solids, one needs to quantify the specific surface site involved in the attachment and detachment rates if one wants to assess solubility constraints. For this reason, the purpose of our work is to study different crystalline states of thorium oxide surfaces without the grain boundaries.

Material and Methods

Samples

In this aim, we synthesized thorium oxides from thorium oxalate $Th(C_2O_4)_2$, 4 H_2O as precursor in order to control the grain size of ThO_2 crystallized with different heating temperatures (T = 700 °C, 900 °C, 1300 °C) ***(Heisbourg, 2003; Oktay and Yayli, 2001; Rand et al., 2008)***. The second solid used in this study is provided by J. Fachinger from Forschungzentrum Jülich (Germany). The particles are spherical and synthesized at a high calcination temperature (1600 °C). A part of the spheres used for solubility experiments are crushed in order to remove all the grain boundaries even into the core of the sphere by the pre-washing experiments. The synthesis method and the physical properties of the solid are described in ***(Müller, 2006; Vandenborre et al., 2010)***, respectively. Table 9 presents the 4 sets of solid sample: (I) Crushed ThO_2 spheres, (II) Initial ThO_2 spheres, (III) ThO_2 powder synthesized at 1300 °C, (IV) ThO_2 powder synthesized at 700 °C.

Table 9: *Sets of solid samples*

Samples	Solid description
I	Crushed ThO_2 spheres
II	Initial ThO_2 spheres
III	ThO_2 powder synthesized at 1300°C
IV	ThO_2 powder synthesized at 700°C

Solid characterization

Solid surface pictures are performed by SEM (scanning electron microscopy, JEOL 5800 SV with a 15 kV voltage). The SEM samples were covered by a Pt layer in order to improve electron conduction and increase the picture resolution. XRD patterns are recorded with the diffractometer BRUKER-AXS D5000 (Bragg-Brentano geometry, copper anticathode Cu at λ = 1.5406 Å). Moreover N_2-gas adsorption by B.E.T. method, using a COULTER SA3100

apparatus, is carried out in order to determine the specific surface area for each solid sample, in particular versus the heating temperature during the synthesis process.

Solubility and 229Th Addition experiments

The pre-washing and solubility batch experiments were performed exposing 150 mg of solids ThO_2(cr) (synthesized powder with different heating temperature, spheres crushed or intact) to an aqueous solution in undersaturated conditions. A HDPE (High Density poly-ethylene) reaction vessel is used, containing 15 mL of a 0.1 mol L^{-1} HCl solution under continuous stirring during 15 days.

We have started the solubility experiments by the contact between each pre-washed solid with the NaCl 0.01 mol L^{-1} aqueous solution at different pH values (3.2, 5.0, 6.8). For the experiments at pH = 3.2, solutions were spiked with a ^{229}Th ($t_{1/2}$ = 7340 years) carrier-free solution to achieve a final $[^{229}Th]_{aq}$ = 4.9 10^{-10} molL^{-1}. The addition date of 200 days corresponds to the time necessary to reach a constant ^{232}Th concentration ("steady state"). Immediately after the addition of the acid ^{229}Th aliquot, the acid perturbation of the solution pH was compensated for by the addition of small aliquots of 0.01 molL^{-1} NaOH until the target pH value of 3.2 was reached again. The objective of adding the spike is to test the reversibility and to allow one to follow the potentially ongoing solution/surface isotopic exchange on the $ThO_{2(cr)}$ surface at "steady state". The dissolution process of $^{232}ThO_{2(cr)}$ and the uptake of ^{229}Th from solution are monitored by sampling aliquots of 0.5 mL over a period of 220 days. After, the solution samples were ultrafiltered, using 1.8 nm cutoff membranes (5 kDa) in order to exclude colloidal particles commonly described in the literature. The ultrafiltered solutions were then acidified with 2 % distilled Nitric Acid and analyzed by inductively coupled plasma mass spectrometry (THERMOELECTRON) for determination of the $^{232/229}Th$ concentration in solution ($[^{232/229}Th]_{aq}$) with an estimated error of 10 %.

Normalization of solution concentrations and rate values

The measured solution concentrations in experiments are normalized to solid composition and surface area and expressed as normalized mass loss NL using the equation

$$NL = \frac{[Th] \times MW_{ThO_2}}{S/V} \quad (1)$$

where [Th] signifies the measured ^{232}Th or ^{229}Th concentrations in mol m^{-3}_{H2O}, MW_{ThO2} is the molecular weight of ThO_2 (g mol^{-1}), S is the surface area (m^2) of the solid, and V the solution volume (m^3). The normalized mass loss rate (in g m^{-2} d^{-1}) is then calculated with the following equation:

$$NLR = \frac{\Delta NL}{\Delta t} \quad (2)$$

where Δt signifies an interval in contact time (d) and ΔNL the variation of normalized mass loss in this interval.

Results

Solid characterization

SEM picture of HTR sphere surface shows grains of thorium oxide coated by grain boundaries (Figure 39) which control the solubility without pre-washing. The solids characterization by X-Rays Diffraction is performed onto the ThO_2 spheres in order to check the high crystalline state of this sample. From the results, we confirm the different crystallization states by the decrease of Full Width Half Middle observed onto the XRD peaks when the heating temperature increases (Figure 40). Hence, the ratio between grains and grain boundaries is different for all these samples. The B.E.T. method give us the specific surface area values between 17.8 m^2/g for the lower crystallized sample (synthesized at 700 °C) and 1.9 m^2/g for the higher crystallized (synthesized at 1300 °C) presented in the Table 9. The specific area value for initial ThO_2 sphere can be estimated from the geometric structure at 1.2 10^{-3} m^2/g. However, it seems not realistic because the pre-washing must be implying a non negligible effect onto the surface of the spheres which increase the specific surface area.

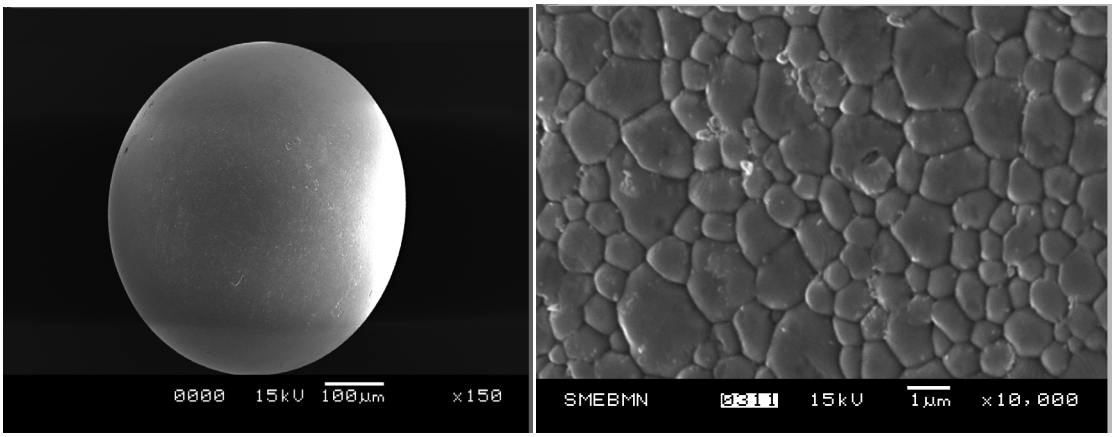

Figure 39: *SEM pictures of ThO_2(cr) HTR sphere with different zooms (×150 and ×10000)*

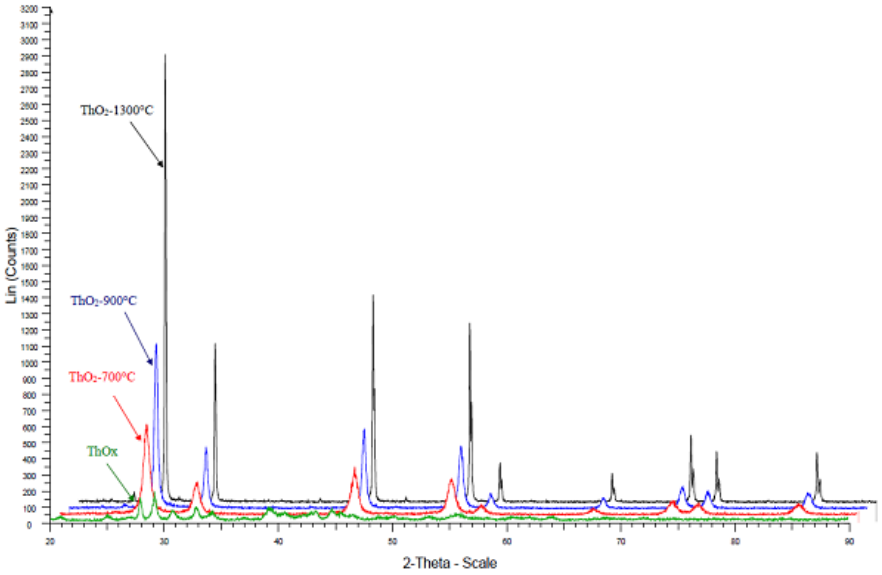

Figure 40: *XRD diagrams of ThO_2 synthesized samples crystallized at 700 °C, 900 °C or 1300 °C.*

Solubility experiments

The Figure 41 presents the results for a contact time of about 100 days. During the dissolution step corresponding to the period between 0 and 10 days, the slopes are different between the 4 sets of sample: (I), (II), (III), (IV) (cf. Table 9). From the results (Table 10), the slope values, which describe the kinetic state of the system, are higher for the powder samples than for the spheres ones and they are similar between the powder synthesized at 1300 °C (III) and the crushed sphere (I). After about 50 days, the pseudo steady-state equilibrium is reached for all samples with different [Th] measurements presented in Table 10. Again, the values are close between the powder synthesized at 1300 °C and the crushed sphere. It seems that the global and the kinetic dissolution behaviours are similar for these two samples. These results indicate the similar behaviour and the close crystalline degree between the powder synthesized at 1300 °C (III) and the crushed sphere (I). We can notice that the NLR value for the sample (II) has been not yet calculated depending on the value of the specific surface area which is not yet empirically determined due to its very low expected value.

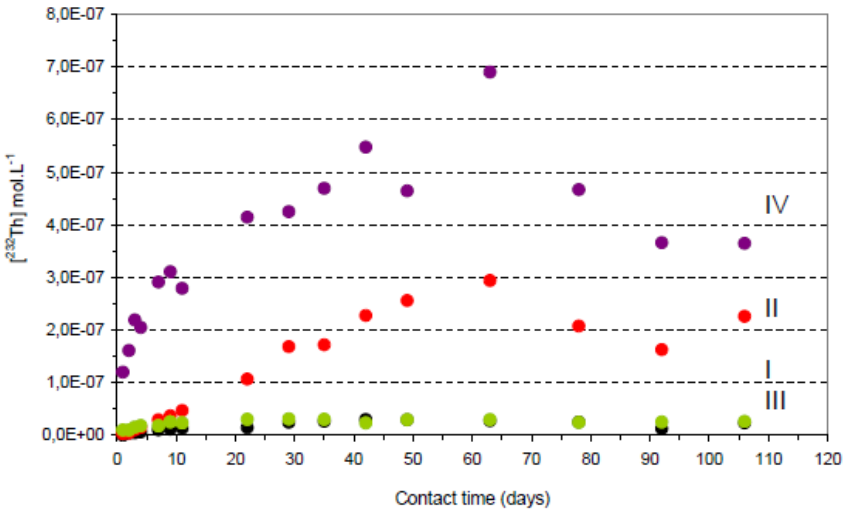

Figure 41: *[^{232}Th] = f(contact time) for each sample at pH = 3.2, monitored by ICP-MS, (I) Crushed ThO_2 spheres, (II) Initial ThO_2 spheres, (III) ThO_2 powder synthesized at 1300 °C, (IV) ThO_2 powder synthesized at 700 °C.*

Table 10: *Experimental data from the solubility experiments for Samples (I), (II), (III), (IV) with a contact time of 110 days.*

Samples	[Th]10d mol/L	Slope (1-10d) mol/L/d	Specific Area m^2/g	NLR(1-10d) $g/m^2/d$	[Th]50d mol/L
I	$1.35\ 10^{-8}$	$1.35\ 10^{-9}$	1.9	$1.88\ 10^{-5}$	$2.95\ 10^{-8}$
II	$4.71\ 10^{-8}$	$4.38\ 10^{-9}$	?	?	$2.56\ 10^{-7}$
III	$2.37\ 10^{-8}$	$1.33\ 10^{-9}$	1.9	$1.85\ 10^{-5}$	$2.98\ 10^{-8}$
IV	$3.11\ 10^{-7}$	$1.91\ 10^{-8}$	17.8	$2.83\ 10^{-5}$	$4.64\ 10^{-7}$

From the results, we made the evidence that the crystalline state of the samples is involved in the dissolution mechanism during the initial kinetic leaching and the reaching of the pseudo steady-state equilibrium. The normalized mass loss rate (NLR) depending on the specific surface area show again the similar behaviour between the powder synthesized at 1300 °C (III) and the crushed sphere (I).

Finally the same evolution of the ratios grain/grains boundaries and global/kinetic leaching behaviour can be described as following: (IV) > (II) > (I) = (III) with (I) Crushed ThO_2

spheres, (II) Initial ThO_2 spheres, (III) ThO_2 powder synthesized at 1300 °C, (IV) ThO_2 powder synthesized at 700 °C.

2.1 ThO_2 powder synthesized at 700 °C (Sample IV)

The Figure 42 presents the concentrations of [^{232}Th] and [^{229}Th] as a function of the contact time for sample (IV) ThO_2 powder synthesized at 700 °C at pH = 3.2 and monitored by ICP-MS. The Table 11 presents the experimental data from the solubility experiments of Sample (IV). When the NLR is determined as a negative value, we can assume that a precipitation process occurs onto the solid surface after the ^{229}Th spike experiments. Then, we assume that the Thorium Oxide at the surface is not completely crystallized and/or is nano-crystallized. That is the reason why we propose $ThO_x(OH)_y(H_2O)_z$ as possible phase at the surface as described elsewhere ***(Vandenborre et al., 2010)***. Moreover we can observe a dynamic exchange between the ^{232}Th onto the surface with the ^{229}Th in the solution. This dynamic exchange process is based on the increasing concentration values of ^{232}Th and on the decreasing concentration values of ^{229}Th. So, we can conclude that the $ThO_x(OH)_y(H_2O)_z$ phase with the low crystallinity of the surface and then the high kinetic of leaching is reactive versus the isotopic Th exchange.

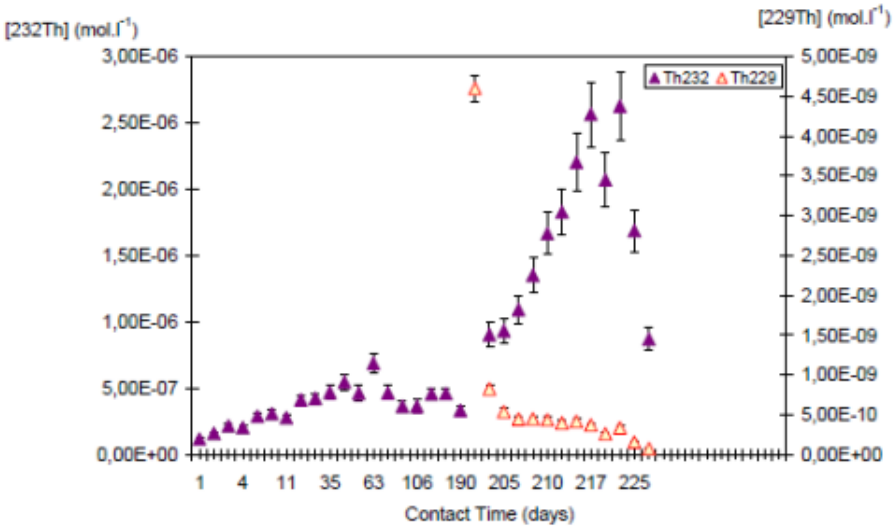

Figure 42: *[^{232}Th] and [^{229}Th] = f(contact time) for Sample (IV) ThO_2 powder synthesized at 700 °C at pH = 3.2, monitored by ICP-MS.*

***Table 11**: Experimental data from the solubility experiments for Sample (IV) with a contact time of 220 days.*

Th isotope	[Th]50d mol/L	Slope (1-10d) mol/L/d	NLR(1-10d) $g/m^2/d$	Slope (200-220d) mol/L/d	NLR(200-220d) $g/m^2/d$
^{232}Th	$4.64\ 10^{-7}$	$1.91\ 10^{-8}$	$2.83\ 10^{-5}$	$1.01\ 10^{-7}$	$1.50\ 10^{-4}$
^{229}Th	×	×	×	$-2.86\ 10^{-11}$	$-4.25\ 10^{-8}$

2.2 Initial ThO_2 spheres (Sample II)

The Figure 43 presents the concentrations of [^{232}Th] and [^{229}Th] as a function of the contact time for Sample (II) Initial ThO_2 spheres at pH = 3.2 and monitored by ICP-MS. The Table 12 presents the experimental data from the solubility experiments of Sample (II). The "×" indicate that ^{229}Th has not been spiked into the solution before a contact time of 200 days. From the results, we can conclude that, in the case of the Initial ThO_2 spheres (II), leaching phenomena did not occur after the ^{229}Th addition. On the contrary, the slow precipitation of one phase mixing ^{229}Th and ^{232}Th is shown with a low kinetic explained by its slow diffusion into the grain boundaries of the solid surface. Nevertheless, the results, presented here for the Initial ThO_2 spheres (II), are not quite determined because the Specific Surface Area can not been measured the classical N_2 adsorption method and we need calculate an assessment of it.

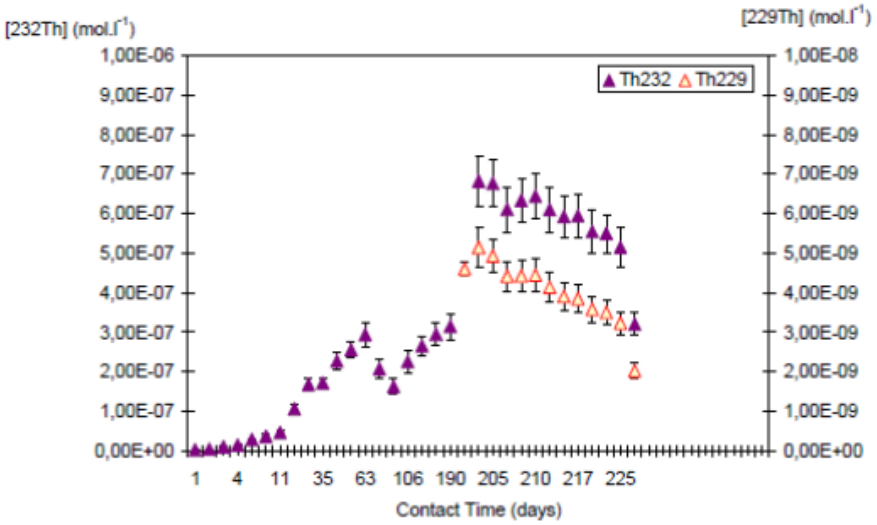

***Figure 43:** [^{232}Th] and [^{229}Th] = f(contact time) for Sample (II) Initial ThO_2 spheres at pH = 3.2, monitored by ICP-MS.*

***Table 12**: Experimental data from the solubility experiments for Sample (II) with a contact time of 220 days.*

Th isotope	[Th]50d mol/L	Slope (1-10d) mol/L/d	NLR(1-10d) g/m^2/d	Slope (200-220d) mol/L/d	NLR(200-220d) g/m^2/d
^{232}Th	2.56 10^{-7}	4.38 10^{-9}	?	-7.76 10^{-9}	?
^{229}Th	×	×	×	-9.65 10^{-11}	?

2.3 Crushed ThO_2 sphere and ThO_2 powder synthesized at 1300 °C (Samples I and III)

The Figure 44 presents the concentrations of [^{232}Th] and [^{229}Th] as a function of the contact time for Sample (I) Crushed ThO_2 sphere and Sample (III) ThO_2 powder synthesized at 1300 °C at pH = 3.2, monitored by ICP-MS. The Table 13 presents the experimental data from the solubility experiments of Samples (I) and (III). The "×" indicate that ^{229}Th has not been spiked into the solution before a contact time of 200 days. As shown in the previous solubility experiments, before the ^{229}Th addition, the behavior versus the leaching phenomena of the surface of the Crushed ThO_2 spheres (I) and of the ThO_2 powder synthesized at 1300 °C (III) is very close. Moreover, the same results are been observed after the ^{229}Th addition: there is no exchange between the two isotopes of the Th (229 and 232) and we observed a quick precipitation and a slower leaching process of the solid surface. Moreover, we can conclude that the leaching rate values for the samples (I) and (III), respectively 2.22 10^{-5} g/m^2/d and 1.62 10^{-5} g/m^2/d, are similar to its of the ThO_2 powder synthesized at 700 °C (I), 2.83 10^{-5} g/m^2/d, which has been described as an $ThO_x(OH)_y(H_2O)_z$ phase. Then, after the ^{229}Th addition, a quick precipitation of the $ThO_x(OH)_y(H_2O)_z$ phase occurs at the surface of the ThO_2 powder synthesized at 700 °C (I) and the slow leaching of this phase is following by the 229 and 232 Th isotopes measurements.

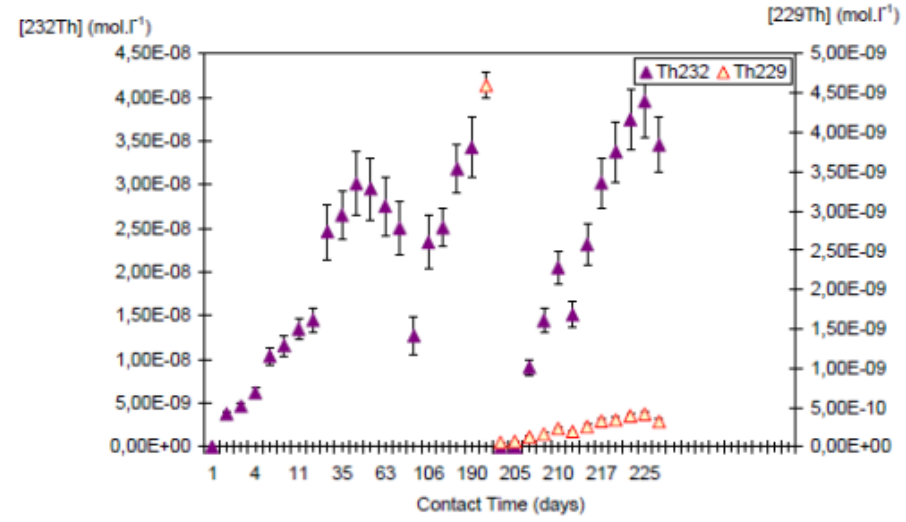

(I)

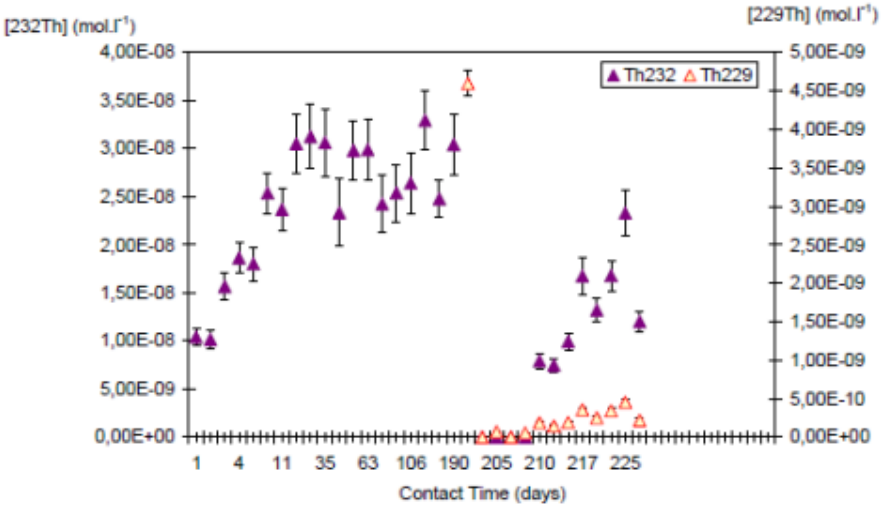

(III)

Figure 44: *[^{232}Th] and [^{229}Th] = f(contact time) for Sample (I) Crushed ThO_2 sphere and Sample (III) ThO_2 powder synthesized at 1300 °C at pH = 3.2, monitored by ICP-MS.*

***Table 13**: Experimental data from the solubility experiments for Samples (I) and (III) with a contact time of 220 days.*

Th isotope	[Th]50d mol/L	Slope (1-10d) mol/L/d	NLR(1-10d) $g/m^2/d$	Slope (200-220d) mol/L/d	NLR(200-220d) $g/m^2/d$
^{232}Th / Ech I	$2.95\ 10^{-8}$	$1.35\ 10^{-9}$	$1.88\ 10^{-5}$	$1.60\ 10^{-9}$	$2.22\ 10^{-5}$
^{232}Th / Ech III	$2.98\ 10^{-8}$	$1.33\ 10^{-9}$	$1.85\ 10^{-5}$	$1.17\ 10^{-9}$	$1.62\ 10^{-5}$
^{229}Th / Ech I	×	×	×	$1.98\ 10^{-11}$	$2.75\ 10^{-7}$
^{229}Th/ Ech III	×	×	×	$2.01\ 10^{-11}$	$2.79\ 10^{-7}$

Conclusions and Future work

We have described the different behaviour of the surfaces of ThO_2 versus the surface crystalline state. The use of the isotopic $^{229}Th/^{232}Th$ exchange assesses the key issue of this Workpackage: the realistic solubility behaviour of the ThO_2 surface. We have classified the 4 sets of solid samples versus the leaching behaviour: (IV) > (II) > (I) = (III) with (I) Crushed ThO_2 spheres, (II) Initial ThO_2 spheres, (III) ThO_2 powder synthesized at 1300 °C, (IV) ThO_2 powder synthesized at 700 °C. Moreover, the behavior of the solid versus the $^{229}Th/^{232}Th$ exchange occurs if the $ThO_x(OH)_y(H_2O)_z$ phase is implied into the solid surface leaching.

The future and complementary works will be performed in order to:

- Determine the specific surface area value for the spheres samples (estimation or measurements)
- Characterize the surface of the leached samples
- Perform desorption experiments after the isotopic exchange steady-state equilibrium reached

Acknowledgement

We acknowledge N. Stephant for SEM measurements from the “Institut des Matériaux Jean Rouxel” laboratory.

The research leading to these results has received funding from the European Union's European Atomic Energy Community's (Euratom) Seventh Framework Programme FP7-Fission-2010 under grant agreement n° 269688 (SKIN project).

References

Heisbourg, G., 2003. Synthèse, caractérisation et études cinétique et thermodynamique de la dissolution de ThO_2 et des solutions solides $Th_{1-x}M_xO_2$ (M = U, Pu), Ph.D. Université Paris XI, Orsay.

Müller, A., 2006. Establishment of the technology to manufacture uranium dioxide kernels for PBMR fuel. Proceedings HTR2006 : 3rd International Topical Meeting on High Temperature Reactor Technology B00000070.

Oktay, E., Yayli, A., 2001. Physical properties of thorium oxalate powders and their influence on the thermal decomposition. Journal of Nuclear Materials 288, 76-82.

Rand, M., Fuger, J., Neck, V., Grenthe, I., Rai, D., 2008. Chemical Thermodynamics of Thorium. North Holland Elsevier Science Publishers B. V., Amsterdam, The Netherlands.

Vandenborre, J., Grambow, B., Abdelouas, A., 2010. Discrepancies in Thorium Oxide Solubility Values: Study of Attachment/Detachment Processes at the Solid/Solution Interface. Inorganic Chemistry 49, 8736-8748.

ON SLOW UO_2 (S) OXIDATION-DISSOLUTION PROCESS AT DIFFERENT REPOSITORY CONDITIONS

Daqing Cui [1,2*], Kastriot Spahiu[3]

[1] Studsvik Nuclear AB (SE)

[2] Stockholm University (SE)

[3]SKB (SE)

* Corresponding author: daqing.cui@studsvik.se

Abstract

The oxidation process of UO_2(s) surfaces at different repository conditions has been investigated. Under air saturated conditions, after 112 days interacting $UO_{2.00}$ powder in a solution containing ^{235}U(VI) (86% enriched) and $NaHCO_3$, the U(VI) concentration increases and ^{235}U/ (^{235}U+^{238}U) ratio decreased. The thickness of dissolved UO_2 from UO_2 particles was 0.3-0.8 nm, and a layer of 0.5-0.6 nm isotope exchangeable layer of UO_{2+x} ($X \leq 0.33$) formed on the surface of UO_2. Under anoxic conditions, the formation of a $UO_{2.27}$ (s) layer on fresh UO_2(s) surfaces is observed as a consequence of U(VI)aq –UO_2(s) interaction. ^{235}U/ (^{235}U+^{238}U) ratio dropped faster than the drop of U(VI) concentration and the thickness of the uranium isotope exchangeable layer $UO_{2.27}$(s) was estimated to be about 1nm. These findings are useful to understand the fate of UO_2 based spent nuclear fuel under repository conditions.

Introduction

The direct disposal of spent nuclear fuel in a deep hard rock repository is being considered in Sweden and several other countries. Corrosion resistant canisters are designed to isolate the spent fuel from the surroundings for very long time periods ***(SKB (1999))***. Thus at the time the groundwater will get in contact with the spent fuel, most γ and β emitters will have decayed and the total dose rate of the spent fuel will have decreased substantially ***(Sunder et al. (1995), Shoesmith et al. (1992))***.

Spent nuclear fuel is largely UO_2(s), with a small fraction (about 4-6 at. %) of fission products and transuranium elements. Most radionuclides are present as solid solution within the fuel matrix and their release rates depend mainly on the rate of dissolution of the UO_2(s) fuel matrix. Hence studies of uranium dioxide dissolution can contribute to an increased understanding of the spent fuel alteration/dissolution process.

There exist a large number of studies on the dissolution of uranium oxide under oxidising conditions. However, deep groundwater is reducing and it has been shown that post-closure oxygen is quickly consumed by reducing minerals ***(Wersin et al. (1994))***, as well as bacteria

(Puigdomenech (2001)). Under such conditions uranium dioxide is stable. The reducing conditions may be disturbed by the production of oxidants through water radiolysis or by the atmospheric oxygen contamination/invasion at accidental situations. It has been shown ***(Spahiu et al. (2000))*** that even small amounts (ppm levels) of oxygen are sufficient to create strongly oxidising conditions, under which $UO_2(s)$ is unstable and undergoes oxidative dissolution. In this case, more oxidised phases of the type UO_{2+x} may form, with stabilities which depend on the pH and the redox potential of the system ***(Shoesmith (2000))***. Electrochemical and X-ray photoelectron spectroscopic studies on the corrosion of $UO_2(s)$ suggest that for corrosion potentials >-100 mV, a surface composition close to $UO_{2.33}$ (corresponding to U_3O_7) is obtained ***(Shoesmith et al. (1992), Shoesmith (2000))***. At higher corrosion potentials, the outer $UO_{2.33}$ layer is subsequently oxidised to soluble U(VI), while the underlying $UO_2(s)$ will be oxidised to $UO_{2.33}$ ***(de Pablo et al. (1996))***. Under oxic conditions, a dynamic equilibrium will build up when the rate of $UO_{2.33}$ layer thickening (UO_2-$UO_{2.33}$) is balanced by the rate of the oxidative dissolution ($UO_{2.33}$ - U(VI)) ***(de Pablo et al. (1996))***.

According to calculations based on published thermodynamic data ***(Grenthe et al. (1992))***, the solubilities of two hyper-stoichiometric uranium oxides $UO_{2.33}$ and $UO_{2.25}$ in near neutral pH solutions are $10^{-7.7}$ M and $10^{-8.1}$ M respectively ***(Grambow et al. (2000))***, lower than $UO_2(OH)_2(s)$ but higher than that of $UO_2(s)$, $10^{-9.4}$ M. The composition of the outer-surface of $UO_2(s)$ depends also on the carbonate concentration of the solution ***(Shoesmith (2000))***, since carbonate forms strong U(VI) complexes and increases the solubility of U(VI) solids. In the absence of carbonate, $UO_2(s)$ corrosion products such as $UO_3.2H_2O$ deposits can accumulate on its surface. For moderate total carbonate concentrations (1-10 mM) the carbonate and bicarbonate ions are kinetically involved in the dissolution process, probably via the formation of surface intermediates ***(Shoesmith (2000))***.

The research work on the corrosion of UO_2 surface and the formation of intermediate corrosion products UO_{2+x} were summarized ***(Shoesmith (2000))*** and a layer of $UO_{2.33}$ is formed on the outer surface of $UO_2(s)$ in a solution with no or lower ($<10^{-3}$ M) $NaHCO_3$.

There is lack of information about the oxidation process of UO_2 at different repository conditions. During the present work, the thickness of UO_{2+x} layer on UO2 which is in dynamic equilibrium with dissolved U(VI) and the interaction between dissolved oxidants, O_2 and U(VI), and freshly reduced $UO_2(s)$ surfaces in solutions with different oxygen contents and pH values were investigated. These observations are useful for understanding the environmental behavior of UO_2 based spent fuel at repository conditions.

Experimental

Materials

UO_2 pellets with natural ^{235}U enrichment (0.72%) were purchased from Westinghouse, Sweden. UO_2(s) fragments from crushed the UO_2 fuel pellets with 2-4 mm size fraction. One mm thick UO_2 slices were sawed from the above mentioned UO_2 pellet and polished. UO_2 powder with natural ^{235}U enrichment was purchased from Westinghouse.

To get freshly reduced $UO_{2.00}$, UO_2 slices and UO_2 powder were pretreated in 5%H_2 atmosphere at 800 ^oC for 20 hours. The newly reduced UO_2 slices had a dark brown color and were stored in Ar filled desiccator before experiments. The oxidation states of uranium in the UO_2 fragments, and freshly reduced UO_2 by H_2 (both slice and powder), determined by Kinetic Phosphorescence Analysis (KPA) method ***(Brina and Miller (1992))*** were $UO_{2.023}$ and $UO_{2.0018,}$ respectively. The specific surface area for the 2-4 mm sized UO_2 fragments and 8 μm sized UO_2 powder as measured by the N_2-BET method were 40 ± 10 $cm^2 \bullet g^{-1}$ and 1.25 m^2/g, respectively,

Argon gas and a gas mixture of 99.97 % Ar + 0.03 % CO_2, both containing less than 2 ppm impurity, were purchased from AGA. All other chemicals were of analytical grade and used as received.

Experimental arrangement

U concentration and $^{235}U/^{238}U$ ratio in solution samples at different time were measured by ICP-MS. The experiments were carried out at room temperature (22 ± 2 ^oC) at the following conditions:

a- Exp A,UO_2 dissolution at air saturated conditions

Three leaching solutions used in the experiment are a) synthetic groundwater, known as Allard water with a composition shown in Table 14, b) 2 mM $NaHCO_3$, 0.1M NaCl and c) 2 mM $NaHCO_3$ 0.1M KCl. In a temperature controlled (23±2 ^oC) laboratory, batch experiments (Exp.A1-A9) were conducted in capped polyethylene bottles with 125 ml air saturated solutions and UO_2 solid, as listed in Table 15.

After the batch experiments the corroded surface of UO_2 slice was rinsed with ethyl alcohol, dried and analyzed. Raman microscope was used to analyze the corroded UO_2 and precipitated particles on it.XPS (X-ray Photoelectron Spectroscopy) was used to analyze the reacted UO_2 surfaces. SEM (Scanning Electron Microscopy)–EDS (Energy Dispersive Spectra) were used to check the microstructure and elemental composition of the corroded UO_2 surface.

TEM (Transmission Electron Microscope)- EDS and Electron Diffraction were used to analyze very small particle precipitated on UO_2 surfaces, and mineral characterization.

Table 14: *The Chemical composition of the synthetic groundwater (Allard water)*

Species	HCO_3^-	SO_4^{2-}	Cl^-	SiO_2	Ca^{2+}	Mg^{2+}	K^+	Na^+
Conc. (mM)	2.01	0.10	0.20	0.2	0.45	0.18	0.10	2.84

Table 15: *Description of Experiment A*

	2mM $NaHCO_3$ Allard water, 125 mL	2mM $NaHCO_3$ 0.1M NaCl 125 mL	2 mM $NaHCO_3$ 0.1M KCl 125 mL
Slice 2 cm^2	Corrosion, Exp.A1	Corrosion, Exp.A2	Corrosion, Exp.A3
Powder 0.25g	Corrosion, Exp.A4	Corrosion, Exp.A5	Corrosion, Exp.A6
Powder 0.25g	isotope exch., Exp.A7 C_0 ^{235}U = 1.6 ppm	Isotope exch. Exp.A8 C_0 86%^{235}U = 1.6 ppm	Isotope exch. Exp.A9 C_0 86%^{235}U = 1.6 ppm

b- Exp. B, interaction between U(IV) and UO_2 (s) at anoxic conditions

The experiment was conducted in a five liter vessel in an argon filled glove bag. The vessel can be tightly capped with help of o-ring and lock and contains a 10 ml reaction bottles and a 50 ml bottle of in-situ oxygen trap with 1g $FeSO_4$, 1g FeS and 1g $CaCO_3$ and 25 mL water ***(Cui and Spahiu (2002))***. The 5 liter vessel was slowly bubbled with Ar + 0.03% CO_2 gas mixture in order to avoid oxygen contamination. 2.6 g newly crushed 2-4 mm sized UO_2 fuel fragments were added in the 10 mL reaction bottles. Several fragments were polished and contained flat surfaces for XPS analysis after being reacted.

1) After a 24 hours of pre-rinsing with the deoxygenated 10 mM NaCl, 2 mM HCO_3^- solution, 2.6 g UO_2 fragments were interacted with 4 mL deoxygenated 10 mM NaCl, 2 mM HCO_3 solution, the U(VI) concentration reached to the value 1.8ppm or $8*10^{-6}$ M after 112 hours.

2) The whole vessel was placed in an ultrasonic bath for 4 hour, the temperature increased to up to 41 ^oC during this period of time. Brown coloured particles suspending in the solution were observed because of the wearing with each other among UO_2 fragments. After the settling down of the particles, 50 μL (≈ 50 mg, weighed by balance) were taken at different times for U(VI) concentration determinations.

3) After three months reaction, the reacted particles were re-suspended by using ultrasonic bath, collected by using a syringe and 0.45 μm filter, dried in vacuum and stored in an Ar-

filled desiccator for KPA O/U ratio analysis, XRD and Laser Raman Spectroscopy analysis.

4) UO_2(s) fragments with polished surface, after being reacted for one day and 90 days, were removed from the reaction bottle in an argon atmosphere and dried in vacuum, then stored in the Ar-filled desiccator for XPS U(VI)/U(IV) ratio analysis.

5) An amount of ^{235}U(VI) solution was added into the reaction vessel with 1.9 g UO_2 fragments to get 11.7 ppm U(VI) and $^{235}U/^{238}U$ ratio of 5.50, and $^{235}U/(^{235}U+^{238}U)$ ratio 0.859. The U(VI) concentrations and uranium isotope ratios were monitored using ICP-MS.

Results and discussion

The consequences of the interaction between oxidants (8ppm dissolved O_2 and $^{235}U(VI)O_2(CO_3)_3^{4-}$) and UO_2(s) in air saturated 2mM $NaHCO_3$ solution were the UO_2 dissolution and the thickening of UO_{2+x} layer on UO_2 surface, as indicated by following reactions,

a) $UO_2(s) + O_2 = UO_2(CO_3)_3^{4-}$ was studied through UO_2 dissolution in Exp A;

b) $UO_2(s) + O_2 = UO_{2+x}(s)$, investigated through XPS surface analysis in Exp B;

c) $2\ UO_2(s) + UO_2(CO_3)_3^{4-} + OH^- \rightarrow 3\ UO_{2.33}(s) + HCO_3^- + 2\ CO_3^{2-}$ followed by U isotope exchange between ^{235}U(VI) in solution and UO_{2+x} on UO_2 surface.

The results of experiments at different conditions are discussed below.

Exp A, UO2 dissolution at air saturated conditions

Uranium concentrations at different reaction times in batch experiments are shown in Figure 45. Even three leaching solutions contain the same concentration of HCO_3^- (2 mM) but UO_2 display different leaching behaviours in these solutions.

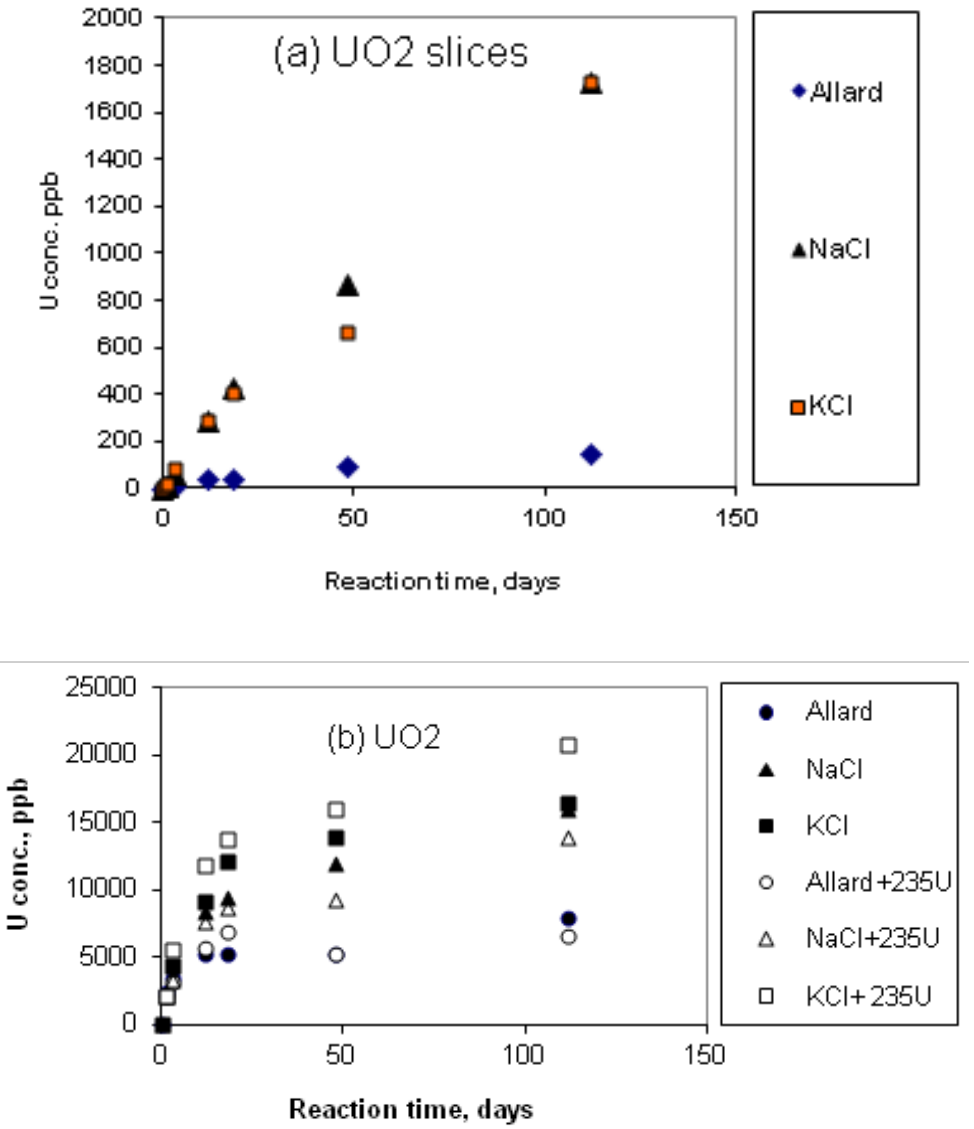

Figure 45: *Uranium concentrations at different times a) 2 cm^2 UO_2 slices b) 0.25g UO_2 powder in Exp A1) –A3) (up) and Exp A4)-A9) (blow)*

The leaching rate of UO_2 slice in 0.1 M KCl was slightly higher than that in 0.1 M NaCl in the first two weeks, but the two leaching rates in the whole period of time were quite similar. The leaching rates of UO_2 powder in 0.1 M KCl are slightly higher than that in 0.1 M NaCl.

The calculated leaching rates in Exp.A2 (0.1 M NaCl), and exp.a3)(0.1 M KCl) during 112 days are similar 0,5±0.1 μg *cm^{-2} *day^{-1}. It is similar with the value obtained in air saturated 0.01 M HCO_3^- solution ***(de Pablo et al. (1996))***. However that in synthetic groundwater in Exp. a1), containing 0.45mM Ca^{2+} and 0.18 mM Mg^{2+}, is 10 times smaller. The leaching rates

of UO_2 in Allard synthetic groundwater are much lower (10 times lower for slice and 2-3 times lower for powder) than the corresponding values in NaCl and KCl solutions.

This indicates that even though the total concentration of HCO_3^- is the same in all solutions, the presence of different cations, Ca(II), Mg(II), Si(IV), and/or anions Cl^- can cause a large difference in the leaching rates.

Even though the concentration of HCO_3^- in Allard water in Exp A1) is 2mM, the same as that in Exp A2 and Exp A3, but the activities of [CO_3^{2-}] in Exp A1 was lower than that in other two experiments. It should be one of the reasons why the dissolution rate of UO_2 is slower in Exp.A1. Another reason might be the incorporation of Ca^{2+} (or Mg^{2+}) ***(Santos et al. (2006a))*** and Si^{4+} ***(Santos et al. (2006b))*** into UO_2 surface is the integral feature of the suppression of the oxidation/dissolution process.

The uranium concentrations in Exp A4 –A9, 6-20 ppm, 2.5-8.4×10^{-5}M were much higher than that in the Exp. A1 –A3. 2.5-8.4×10^{-5}M U(VI) is close to the solubility of U(VI) at the experimental conditions ***(Grenthe et al. (1992))***. This may explain the larger difference between dissolution rates during the initial and final periods in Exp A4-A9 than that in Exp A1 and A3.

The HCO_3^- in leaching solutions after experiments was measured by selective electrode, and no significant difference was found in all experiments 2.30 ± 0.06 mM.

The corroded uraninite surfaces were analysed by several surface techniques. XPS were used to check potential ions co-ordinated on the surface. The information area of XPS is <1mm^2 and depth is about 5 nm. On the surface of UO_2 slice corroded in the Allard water in the present of air, about 2% Ca(atom%) was detected. The solution is under saturated with $CaCO_3$, however, calcite like particles were observed on the surface of UO_2. One hypothesis is that in the solution close to UO_2 surface, the surface complexed OH^-can affect the local chemical conditions, the solubility product of $CaCO_3$ that based on homogeneous bulk soluton chemistry may not be necessary valid. Some compounds containing CaMg-U(VI)-Si, ***(Santos et al. (2006a, 2006b))*** may also hinder the UO_2 dissolution.

By using Raman microscope, corroded UO_2 surfaces from Exp A1, A2 and A3, (samples 1, 2, and 3, respectively), a round 10 μm sized aggregate (sample 1.2) that was found on UO_2 from Exp a1) and unreacted UO_2 were analysed, as shown in Figure 46.

The round aggregate was later found to be uranium rich by SEM-EDS. It may be an altered UO_2, (i.e. UO_{2+x}) and displays similar Raman peak positions to UO_2. Its peak at 444cm^{-1} is narrow and higher, but all other peaks are much smaller than that for sample 1, 2, and 3.

An area (150μm×100μm) around the aggregate (sample 1.2), on UO_2 surface reacted in Allard water Exp.A1 was mapped by Raman microscope at different spectra peak positions (not given here). The result shows that UO_2 surface became heterogeneous. It looks like UO_2

grains with different alignments, or being heterogeneously incorporated with Ca^{2+}, Mg^{2+} and Si^{4+}, have different Raman spectra. More research is needed to understand this phenomena. Comparing peaks of different samples, UO_2 surfaces corroded in Allard water with and without particles have less intensity than that of other peaks, and smaller or no shoulder at 1150cm^{-1} evidenced the existence of $UO_{2.00}$ ***(Manara and Renker (2003))***.

Several Ca-Mg-Si containing particles 10-40 μm sized were observed on UO_2 surface by using SEM-EDS, one of them is shown in Figure 47. Two particles were analysed by TEM-EDS and electron diffraction, the result show that the precipitate on UO_2 surface reacted in Allard water contains 59 % Ca, 37 % Mg and 2 % Si display an electron diffraction patterns that match to calcite related mineral (Mg, Ca)CO_3, with space group R-3 or R-3c. a = 4.8 - 4.9, c = 16-17 Å. Both particles can be indexed as calcite-like minerals using the unit cell parameters given above. Together with the EDS analysis, the particles are confirmed to be a calcite-related mineral. A precipitate containing very rich Si was also detected by SEM-EDS.

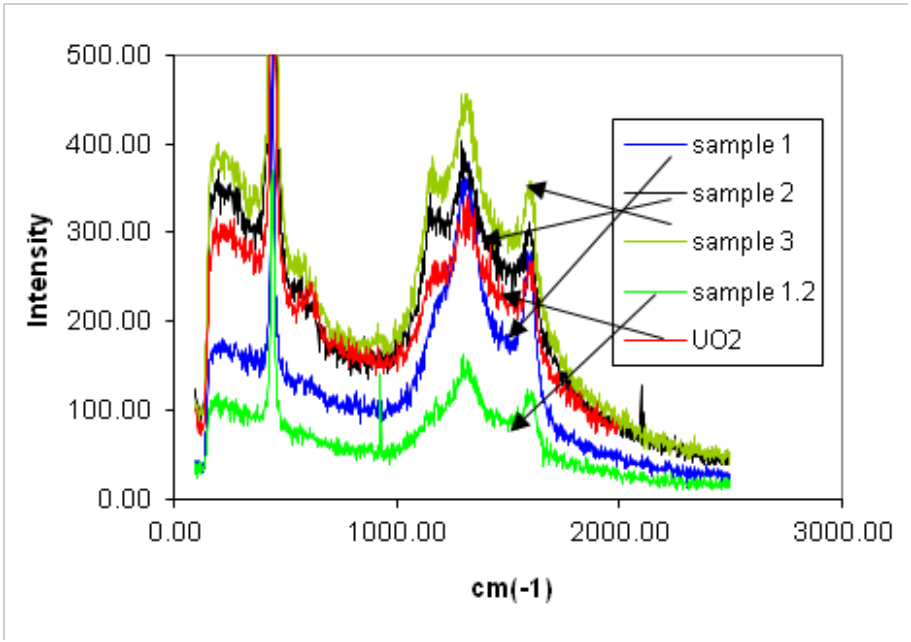

Figure 46: *The Raman Spectra of corroded UO_2 surfaces, sample 1, 2 and 3 from Exp.a1), a2) and a3), respectively. Sample 1.2 is the corroded UO_2 surface including an aggregated particles formed on it from Exp.a 1).*

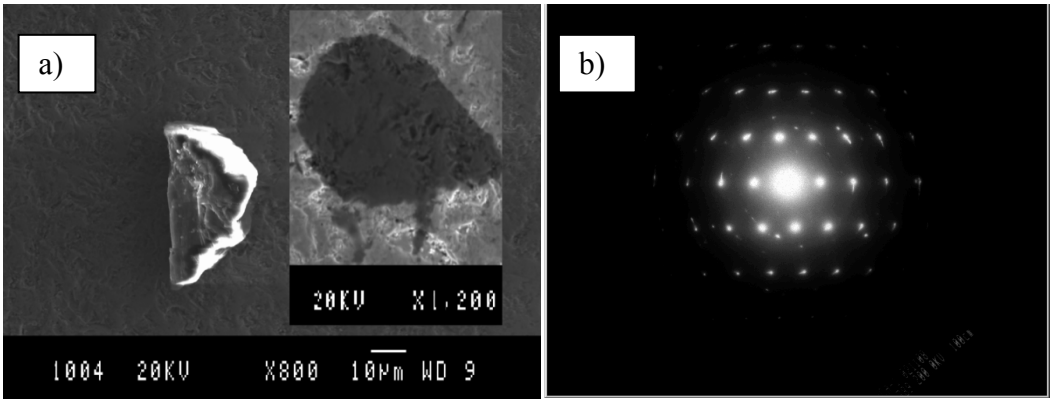

Figure 47: *Calcite like precipitate on corroded UO_2 surface from exp.a1 with Allard water. a) one of precipitated aggregates left UO_2 surface during SEM –EDS analysis and left a black "foot print" behind. SEM-EDS results show it contains 46 % Ca and 36 % Mg. b) TEM and electron diffraction ([100] zone axis)*

Isotope exchange, Exp A-A9

Assuming

a) A certain depth of outer-layer $UO_{2.33}$ that formed on the surface UO_2 powder that is in equilibrium with U(VI) in solution has the same isotope ratio (r_e)) as that in solution after 112 days reaction,

Uranium oxide (UO_2-$UO_{2.33}$) surface area is equal to BET specific area, 12500 cm^2/g,

the depth of the isotope equilibrated outer layer can be roughly estimated according to the mass balance and isotope dilution principles, as shown by the equation 1 to equation 1-5,

$$C_0\ ppm * r_0 = C_e\ ppm * r_e + S_{total}\ ppm * r_e \quad (1)$$

$$M_{total}\ mg = S_{total}\ ppm * v\ ml / 1000\ mL \quad (2)$$

$$M_{UO2.33}\ g = M_{total}\ mg * (238+16*2.33)/238*10^{-3}\ g/mg \quad (3)$$

$$Vuo_{2.33}\ cm^3 = M_{UO2.33}\ g / D\ g*cm^{-3} \quad (4)$$

$$h\ cm = Vuo_{2.33}\ cm^3 / A\ cm^2 \quad (5)$$

where,

C_0 (*ppm*), C_e *ppm*: U concentration when t= 0 or at end of the experiment.

r_0 , r_e: $^{235}U/(^{238}U+^{235}U)$ ratio in solution when t = 0 and at the end of experiment

S_{total} (*ppm)*: relative mass of U in UO_{2+x} that in isotope equilibrium with U(VI) in solution

M_{total} (*mg*): mass of U that in equilibrium with U(VI) in solution

v (*mL*): volume of solution (125 mL)

$M_{UO2.33}$ (*g*): mass of $UO_{2.33}$

D (g/cm^3) density of $UO_{2.33}$, 11 g/cm

V cm^3 volume of $UO_{2.33}$ layer on UO_2

A cm^2: surface area 0.25 g * 12500 cm^2/g (BET) = 3125 cm^2

Under oxic conditions with normal groundwater pH and 2mM $NaHCO_3$, a nm range very thin UO_{2+x} layer was estimated. It is in an agreement with what is expected ***(Shoesmith (2000))***. The results of three batch experiments are summarized in Table 16.

Table 16*: The results of three batch experiment*

	Exp a7, Allard water			Exp a8 , 0.1M NaCl			Exp a9, 0.1M KCl		
t, days	r	C, ppm U	h, nm	r	C, ppm U	h, nm	R	C, ppm U	h, nm
0	0.8595	1.2	0	0.8595	1.2	0	0.8592	1.2	0
1.2	0.8457	--	--	0.8442	--	--	0.8442	--	--
5.2	0.0654	--	--	0.0575	--	--	0.0521	--	--
112	0.0494	6.666	Dissolution h_d=0.28nm, Isotope exchangeable h_{ex}=0.59nm	0.0421	13.87	Dissolution h_d=0.52nm, Isotope exchangeable h_{ex}=0.48nm	0.0291	20.8	Dissolution h_d=0.81nm, Isotope exchangeable h_{ex}=0.59nm

Experiment B, U(VI) –UO_2 interactions at anoxic conditions

a- Gibbs free energies of possible U(VI) –UO_2 interactions

The results show that under anoxic conditions, the concentration of uranyl carbonate species in the solution decreases when contacted with fresh $UO_{2.00}$ surfaces that newly created during four hours of ultrasonic bath, as shown in Figure 48, possibly forming $UO_{2.25}$ or $UO_{2.33}$ as a secondary product, through the interactions (1) and (2) given below. Gibbs free energy values the corresponding these two reactions (ΔG) can be calculated as follow:

i) Assuming the final product is $UO_{2.25}(s)$ or expressed as $U_4O_9(s)$

$$3\ UO_2\ (cr) + UO_2\ (CO_3)_3^{4-} + OH^- \rightarrow 4\ UO_{2.25}\ (s) + HCO_3^- + 2\ CO_3^{2-} \quad (1)$$

ΔG^o =-1031.833×3 -2659.543 -157.2 -1069.125×4 -586.845 -528.1×2 = -7.3 kJ/mol

$\Delta G = \Delta G^o + RT\ Ln\ [(\{HCO_3^-\}\ \{CO_3^{2-}\}^2\ ) /(\{UO_2CO_3)_3^{4-}\}\ \{OH^-\})] \approx$ -16 kJ / mol) ii)
Assuming the final product is β-$UO_{2.33}$ or expressed as β-U_3O_7 (2)

$$2\ UO_2\ (cr) + UO_2\ (CO_3)_3^{4-} + OH^- \rightarrow 3\ UO_{2.33} + HCO_3^- + 2\ CO_3^{2-}$$

ΔG^o =-1031.833×2, -2659.543 -157.2, -1080.572×3, -586.845 -528.1×2= -4.3 kJ/mol

$\Delta G = \Delta G^o + RT\ Ln\ [(\{HCO_3^-\}\ \{CO_3^{2-}\}^2) / (\{UO_2CO_3)_3^{4-}\}\ \{OH^-\})] \approx$ -13.7 kJ / mol

The negative ΔG values for reaction (1) and (2) indicate that both reactions are thermodynamically possible. The nearly linear relationship between $Log[U]_t$ or $-Ln([U]_t/[U]_0)$ and reaction times, t, as that shown in Figure 48, during the first and the second halves of experimental periods (12 days), respectively, indicates that the reaction displays a pseudo first order reaction kinetics during these two periods of time.

One of differences between adsorption and multi-electron redox reactions is that the former often display a faster reaction kinetics, which usually is controlled by diffusion processes, while the latter often display a slower pseudo first order kinetics ***(Cui and Eriksen (1996))***. The experimental results suggest that the reaction between $UO_2(s)$ and uranyl carbonate species is kinetically controlled either by some electron transferring process or solid re-structuring. However this needs to be proved by more experimental evidence.

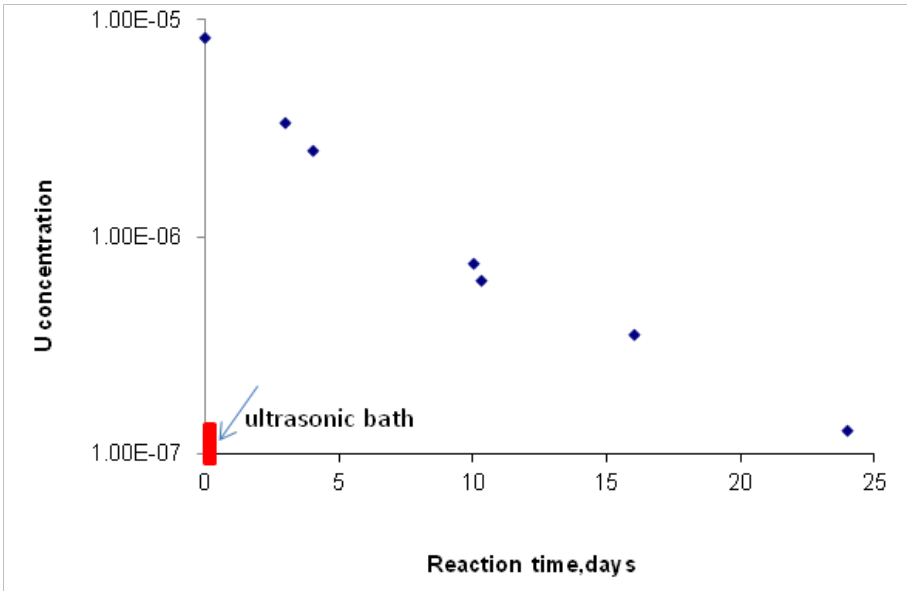

Figure 48: *Logarithmic U(VI) concentrations at different times in the U(VI)-UO_2 experiment with in-situ oxygen trap. During the first 4 hours, ultrasonic bath was applied to generate suspended particles with fresh $UO_{2.0}$(s) surface.*

b- Surface analysis

The U(VI)/U(IV) ratios for both the initial and reacted UO_2(s) surfaces in Exp B were measured by XPS (X-ray photoelectron spectroscopy) method and the calculated x value for UO_{2+x} are given in Table 17. The XPS method is often used to check chemical composition or/and oxidation states of outer-layer in a depth about a 3λ (≈ 3-10 nm), much thinner than that of the information layer analysed by Raman. Even though the uncertainty of single U(VI)/U(IV) measurements by the XPS method is rather high (± 5% in x), the results of the XPS analysis showed that:

- in open atmosphere, there is a pre-oxidised U(VI) layer on the outer surface of UO_2(s) fragments
- the pre-oxidised UO_{2+x} layer is dissolved in a 2 mM HCO_3^- solution and
- under anaerobic conditions, uranyl carbonate may react with fresh $UO_{2.0}$ (s) surfaces and form an UO_{2+x} layer on the UO_2 (s) surface, the final product being most probably $UO_{2.25}$ (U_4O_9).

The results of the analysis of the suspended particles collected and dried under anaerobic conditions are listed below:

- The U(VI)/U(IV) ratio was determined by the KPA method to be 0.162, corresponding a value of x = 0.14 in UO_{2+x}.. It must be noted that the during the sample treatment, the filtrate particles are dissolved in 1 M H_3PO_4, therefore the U(VI)/U(IV) ratio determined by KPA method is an average value for whole particles, instead of the outer-surface

layer. KPA results can only qualitatively show the existence of the hyper-stoichiometric UO_{2+x}(s) on the suspended particles.

- Optical photographs: in comparison with crushed fine particles of the original UO_2 fragments, the reacted fine particles are of lighter colour than the original.
- Laser Raman Spectroscopy: the reacted sample has two new peaks at 1307.7 and 1153.1 cm^{-1}, as compared to the Raman spectra of the original peroxidised fragments. It may be interpreted that the $UO_{2.0}$ below the nm thick U O_{2+x} of the reacted sample contribute more than that in the original pre-oxidised sample, or the x value in the reacted sample is smaller than the x in the originally pre-oxidized sample (As shown in Table 17).
- X-ray diffraction (XRD): the diffraction peaks of the reacted sample are wider than that for the original sample. No shift of the peak positions indicating shorter distances in the reacted sample was observed. Because of the penetration characteristics of X-rays, the results of X-ray diffraction (XRD) can't provide information on outer layers of μm thickness.

Table 17: *The U(VI)/U(IV) ratio of uranium oxide surfaces formed in anoxic solutions initially containing 2 ppm U(VI), 10mM NaCl and 2 mM HCO_3^-, analysed by XPS and calculated x value of UO_{2+x}.*

	Original pre-oxidised	reacted 1 day	reacted 3 months
U(VI)	4.2	0.3	2.70
U(IV)	7.0	5.1	7.20
U(VI)/U(IV)	0.60	0.056	0.375
X in UO_{2+x}	0.38	0.06	0.27

c- Isotope exchange

After removing 0.7 g solid fragments from reaction bottle (for XPS analysis), about 20 μl 170 ppm 87% ^{235}U enriched U(VI) solution with 0.02 N HCl was added into reaction bottles with 1.9 g solid and 3.5 mL liquid. U(VI) concentrations and ^{235}U / ^{238}U ratios are plotted against the reaction time in Figure 49. U(VI) concentration decreased first rapidly and then slowly. From Figure 49 it can be observed that

a) The isotope exchange process is faster than the interaction between U(VI) in solution and UO_2(s) and

b) with the thickening of UO_{2+x} layer, the interaction between U(VI) in solution and UO_2(s) become slower with reaction time.

Unfortunately, the surface area of the small particles generated by using ultrasonic bath was not estimated, therefore the thickness of isotope exchangeable layer could not be estimated in this isotope exchange experiment (Exp. B). It can be improved in our future experiments.

If this hypothesis is true, at anaerobic groundwater conditions, fresh UO_2(s) surface in the central part of spent fuel pellet will react not only with α radiation produced O_2 and H_2O_2, but also with the first amounts of U(VI) that oxidatively dissolved from the spent fuel surface at the rim region (higher α dose rate and more oxidative). In other words, significant dissolution of spent fuel will start only after all outer surface of UO_2(s) is covered by a layer of UO_{2+x}.

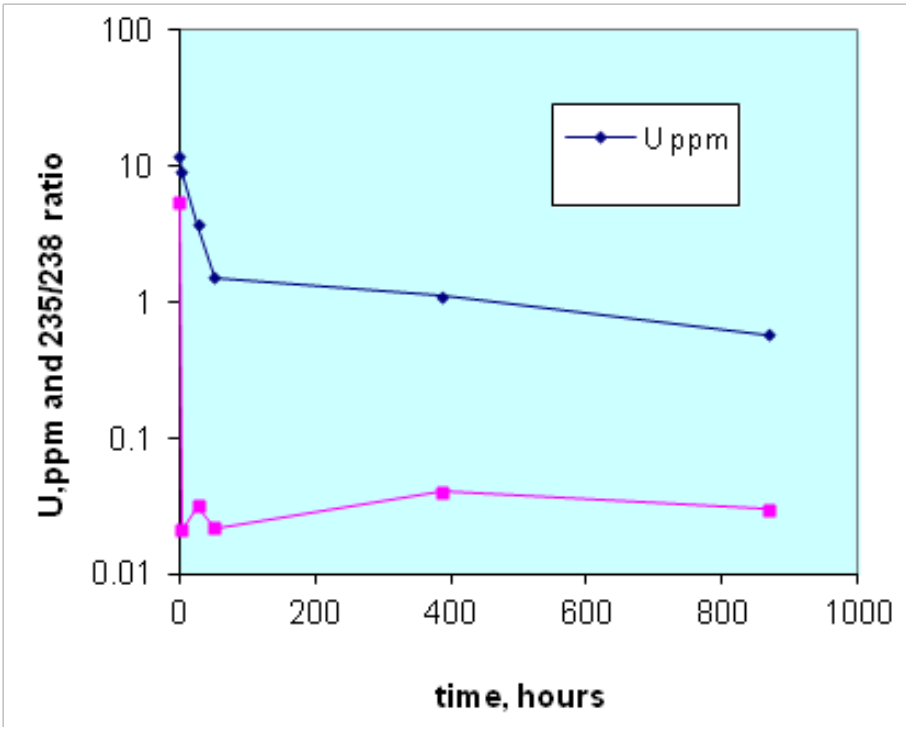

Figure 49: *U(VI) concentrations and ^{235}U / ^{238}U ratios are plotted against the reaction time*

Summary

Through this work, the follow points can be summarised:

The leaching rates of UO_2 in air saturated and pH 8 buffer conditions are not only affected by HCO3- concentrations but also affected by cations, Na^+ , K^+, Ca^{2+} Mg^{2+} and Si(IV), in other words, depends on activities of complex anion CO_3^- for U(VI).

The corrosion of UO_2 is heterogeneous.

Precipitated aggregates with different contents of Ca Mg and Si were observed, and the result of electron diffraction proved they are calcite like minerals such as $Ca_2Mg(CO_3)_3$. An Si rich precipitate (SiO_2) was also observed.

$CaCO_3$ and quarts like precipitates formed on UO_2 surface in a solution below the solubility products of the minerals may in some degree partially block diffusion of oxygen and water molecules to UO_2(s) surface therefore hinder the dissolution of UO_2.

The result of isotope exchange experiment shows the isotope exchangeable $UO_{2.33}$ layer on corroded UO_2 very thin about 1 nm, and similar in thickness of $UO_{2.33}$ with different leaching solutions.

Under the anoxic groundwater conditions with 10^{-3} M carbonate, the concentration of U(VI) (as $UO_2(CO_3)_3^{4-}$) was found decrease substantially when the solution was contacted with fresh UO_2(s) surfaces that generated mechanically by using ultrasonic bath, probably by forming a layer of UO_{2+x} (most possibly $UO_{2.25}$) on the outer-surface of UO_2(s).

ΔG calculations show that the reaction between $UO_2(CO_3)_3^{4-}$) and UO_2 is thermodynamically possible and batch experiments indicate that the reaction can take place.

These findings are useful for understanding the fate of UO_2 based spent fuel at repository conditions.

Acknowledgements

This work was performed at Studsvik Nuclear AB and Stockholm University with support from the Swedish Nuclear Fuel and Waste Management Co. (SKB) and support from European atomic energy community, FP7 fission-2010, SKIN project, grant agreement number 269688.

References

Deep repository for spent nuclear fuel. SR 97 - Post-closure safety, SKB TR 99-06, Stockholm (1999).

Sunder S, Shoesmith D.W and Miller N.M. Mat Res. Symp. Proc. Vol 353 p 617 (1995).

Shoesmith D. W. and Sunder S. J. Nuclear Material Vol 190 p20 (1992).

Wersin P, Spahiu K., and BrunoJ., SKB Technical Report 94-02, Stockholm (1994).

Puigdomenech I., Ambrosi J-P., Eisenlohr L., Lartigue J-E., Banwart S. ., Bateman K., Milodowski A. , West J. Grifault L., Gustafsson E., Hama K., Yoshida H., Kotelnikova S., Pedersen K., Michaud V., Trotignon L., Rivas Perez J. , Tullborg E-L., O_2 depletion in granitic rocks, SKB TR 01-05, Stockholm (2001).

Spahiu K, Werme L., Low J., and Eklund U.B., in Sci. Basis for Nuc. Waste Management XXIII, ed. by R. W. Smith and D. W. Shoesmith, Mat. Res. Soc. Symp. Proc., 608 (2000).

Shoesmith D.W., J. Nucl. Mater.Vol 282 p1-31(2000).

de Pablo J. Casas I, Giménez J. Marti V. and Torrero M.E: J. Nucl. Mater. Vol 232, p138-145 (1996) .

Grenthe I., Fuger J., Konings R. J. M., Lemire R., Muller A. B., Nguen - Trung C., and Wanner H.: Chemical Thermodynamics of Uranium, Elsevier Science Publishers, Amsterdam (1992).

Grambow B., Loida A., Martinez-Esparza A., Diaz-Arocas P. , de Pablo J., Paul J.-L., Marx G., Glatz J.-P., Lemmens K., Ollila K., Christensen H., "Source term for performance assessment of spent fuel as a waste form", European Commission, Nuclear Science and Technology, EUR 19140 EN (2000).

Brina R. , Miller A.G. Analytical Chemistry 64 1413-1418, (1992).

Cui D, and Spahiu K., Radiochim. Acta 90 (2002) 1-6.

De. Pablo J., Casas I., Gimenez J., Torrero M. E. , Journal of Nuclear Material 232 (1996) 138-145

Santos B.G., Noel J.J, Shoesmith D.W., Journal of Nuclear Materials 350 (2006a) 320–331

Santos B.G., Noel J.J, Shoesmith D.W., Corrosion Science 48 (2006b) 3852–3868

Manara D., Renker B., Raman spectra of stoichiometric and hyperstoichiometric uranium dioxide, Journal of Nuclear Materials 321 (2003) 233–237

Cui D., Eriksen .T.E, Environ. Sci. & Technol., Am. Chem. Soc. Vol. 30, p 2259-2262, (1996).

DECOMPOSITION OF ARSENAZO III BY FENTON REACTION INDUCED BY GAMMA IRRADIATION

Z. Zheng [1], M.L. Kang [1], C.L. Liu [1,*], Bernd Grambow [2], Lara Duro [3], Tomo Suzuki-Muresan[2]

[1] Beijing National Laboratory for Molecular Science, Radiochemistry & Radiation Chemistry Key Laboratory for Fundamental Science, College of Chemistry and Molecular Engineering, Peking University, Beijing 100871, China

[2] SUBATECH, Unité Mixte de Recherche 6457, Ecole des Mines de Nantes, CNRS/IN2P3, Université de Nantes, 4 rue Alfred Kastler, BP 20722, 44307 Nantes cedex 03, France

[3] AMPHOS21 , P. Garcia Ifaria49-51, Barcelona, E-08019, Spain

*Corresponding author liucl@pku.edu.cn

Arsenazo III (2,2'-[1,8-dihydroxy-3,6-disulfo-2,7-naphthalene-bis(azo)]dibenzenearsonic acid), an organic compound that gives marked color reactions (violet, blue and green) with a number of elements, is one of the most widely used metal indicator for the photometric determination of uranium, thorium, plutonium, barium, strontium, hafnium, bismuth, manganese, cobalt and the rare earth elements (Savvin, 1963; Zyryanov and Baykov, 2002; Khan et al., 2006; Dedkova et al., 2008). The specificity of this reagent is to form strong and stable metal chelate complexes with the elements mentioned above. This point is important especially for experiments requiring extreme conditions such as very high pH or acidic media where hydrolysis reactions could occur and polynuclear species could be formed. Moreover, the use of color dyes for their spectrophotometric determination and quantification is simple and selective (Rohwer et al., 1997) and arsenazo III is a suitable dye to stabilize the elements with various oxidation degrees as it is the case for uranium and plutonium.

Fenton reaction is well known for their advanced oxidation processes (AOPs) in particular with the organic compound (Bouniol, 2010; Nidheesh and Gandhimathi, 2012). The principle of the Fenton reaction is based on a mixture of dissolved iron (Fe(II), catalyst) and hydrogen peroxide (H_2O_2, Fenton reagent).

This study indicates that, for ordinary solution samples, due to the strong complex ability, Fe(III) can significantly decrease the UV-Vis absorbance of U(VI)-arsenazo III complex, while the influence of Fe(II) to the absorbance is negligible. However, when Fe(II) is present in a gamma irradiated U(VI) solution, it can give rise to Fenton reaction which can decompose the subsequently added arsenazo III, leading to a sharp decrease of the absorbance of U(VI)-arsenazo III complex.

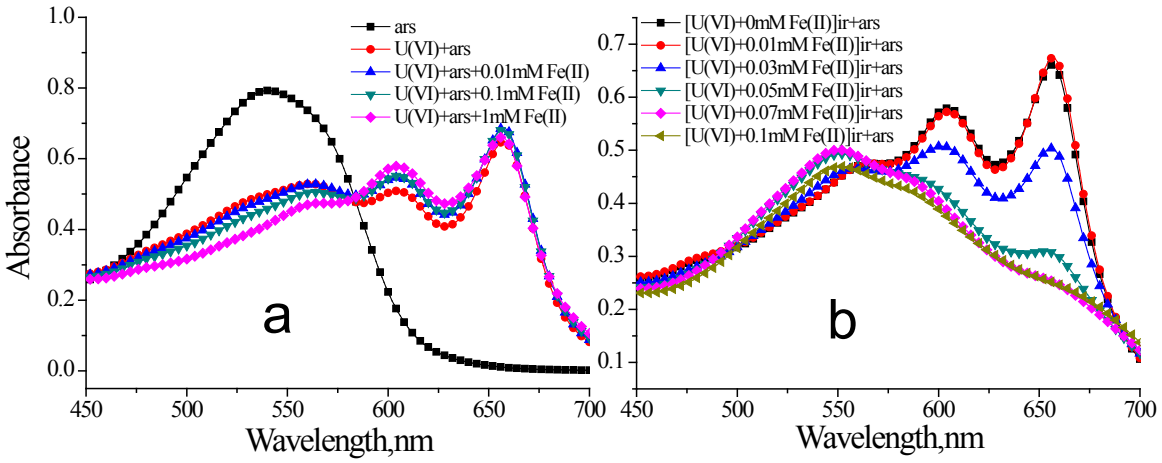

Figure 50. Influence of Fe(II) on the absorption spectra of U(VI)-arsenazo III complex: (a) U(VI)+Fe(II) solutions without gamma irradiation; (b) U(VI)+Fe(II) solutions had absorbed 1.8 kGy gamma irradiation before recording the UV-Vis spectroscopic data.

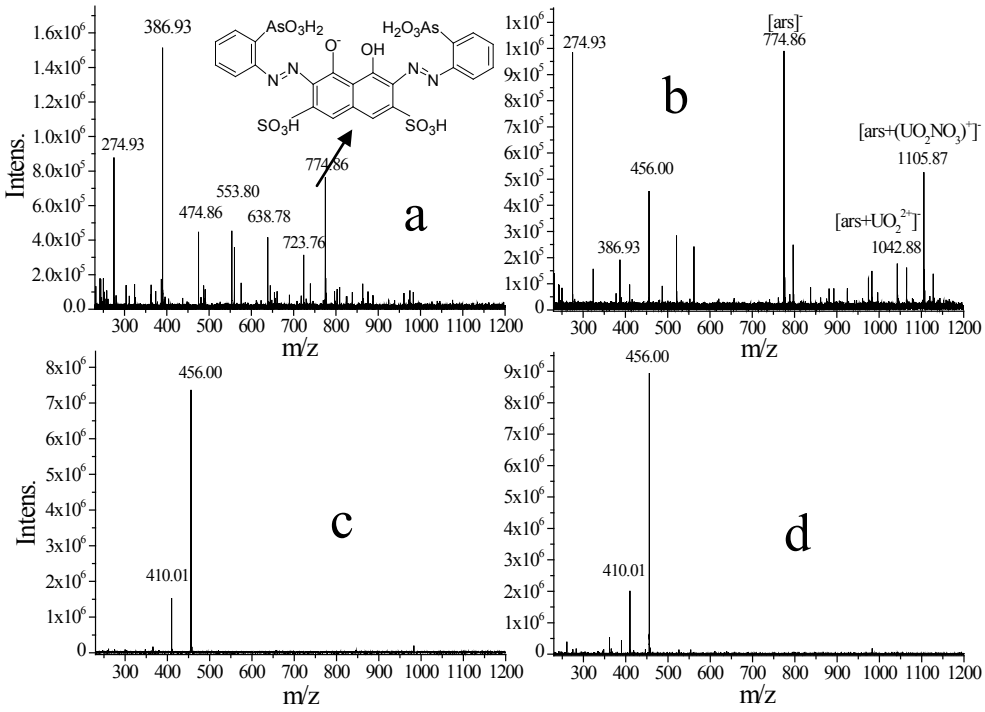

Figure 51. Zoom in the regions of interest for ESI-MS spectra: (a) free arsenazo III solution (0.02%); (b) 0.01 mM U(VI) + arsenazo III (0.02%) solution; (c) irradiated U(VI) solution (0.01 mM) at 1.8 kGy + 0.1 mM Fe(II) + arsenazo III (0.02%); (d) 0.01 mM U(VI) + 0.1 mM Fe(II) + 0.1 mM H_2O_2 + arsenazo III (0.02%) solution.

ADDING UPTAKE KINETICS AND SURFACE ENTRAPMENT TO GEOCHEMICAL MODELS

Bruno M.J. Thien[1*], Dmitrii A. Kulik [1], Enzo Curti[1]

[1] Paul Scherrer Institut (Switzerland)

* Corresponding author: bruno.thien@psi.ch

Abstract

Chemical thermodynamics alone is usually not sufficient to predict trace element partitioning in host minerals, as evidenced by the growth-rate dependency of trace element partitioning occurring in many water-rock systems like nuclear waste repositories. In this context, three uptake kinetic models were tested and unified into a new one suitable for implementation in geochemical modelling codes. The obtained model, implemented as a script in GEM-Selektor code, is also able to predict the effects of variation in solution composition on trace element partitioning, which is not directly possible in three 'parent' models.

Introduction

The objective of Task 4.1 is to develop a new partial equilibrium approach to geochemical modeling of the slow uptake of radionuclides upon (re)precipitation of solid solutions (SS) with host minerals such as calcite. Irreversible trace element uptake in growing minerals cannot be accurately predicted using an equilibrium aqueous solid-solution thermodynamic model alone because the experimentally measured trace element partitioning usually depends on precipitation rates and related kinetic effects. A suitable model has to account for such deviations from 'true' equilibrium. In this contribution, three existing models of trace element uptake in host minerals that take into account kinetic effects were evaluated and compared: the Surface (growth) Entrapment Model (SEMO) (***Watson (2004), Watson and Liang (1995)***), the Surface Reaction Kinetic Model (SRKM) (***DePaolo (2011)***), and the Adsorption Diffusion Desorption Model (ADDM) (***Barrow (1983)***).

1. Methods and models

1.1 Fractionation coefficient

The distribution of a trace element *Tr* between the aqueous solution (or melt) and the mineral (crystalline solid solution) relative to the host component *Hc* is usually described by the fractionation coefficient $\Delta_{Tr,Hc}$:

$$\Delta_{Tr,Hc} = \left(\frac{x_{Tr}}{[Tr]}\right) \Big/ \left(\frac{x_{Hc}}{[Hc]}\right) \quad (1)$$

where *x* are mole fractions for the solid, and [] are molarities or molalities for the aqueous part.

1.2 Growth (Surface) Entrapment Model (SEMO)

The first version of the Growth Entrapment Model was originally proposed by ***Watson and Liang (1995)*** and later improved by ***Watson (2004)*** to account for the surface depletion of some elements and the depth variability of the diffusivity in calcite. The main assumption of SEMO is: "*a growing crystal takes the composition of its surface, unless diffusivity in a thin near-surface region is effective during growth*." In other words, there is a competition between precipitation rate and diffusivity, where diffusivity is here a generic term describing compositional homogenization within a thin (some nanometer-thick) layer directly beneath the mineral surface. In general, the equilibrium concentration of a trace element adsorbed on the mineral surface (i.e. $\Delta_{Tr,Hc,ads}$) will be different than its concentration in solid solution in equilibrium with the same aqueous electrolyte phase (i.e. $\Delta_{Tr,Hc,eq}$). If mineral growth is faster than the diffusion of the trace element within the aforementioned few nanometer-thick layer then the bulk solid will tend to acquire the trace element concentration established by the fast adsorption equilibrium on the mineral surface. If the "diffusion" flux is faster than the mineral growth rate, the trace element content in the solid will approach that of a solid solution in equilibrium with the aqueous phase.

In other words, the progressing precipitation tends to 'entrap' the surface composition, whereas the diffusivity drives the sub-surface layer to take a composition closer to that in a (hypothetical) equilibrium between aqueous electrolyte and solid solution. Since the mineral continues to grow, the trace elements in 'older' layers become isolated from the aqueous solution and are, in principle, in metastable equilibrium. This irreversible process of enrichment or depletion in trace element relative to the expected aqueous-solid or melt-solid equilibrium concentration is called "surface entrapment".

The general reactive-transport equation of the SEMO model is:

$$\frac{\partial C}{\partial t} = \frac{\partial}{\partial h}\left[D\frac{\partial C}{\partial h} \right] + \left[V - \frac{\ln(F)}{l} D \exp\left(\frac{h}{l}\right) \right] \frac{\partial C}{\partial h} - \frac{\ln(F)}{l} C \exp\left(\frac{h}{l}\right) \frac{\partial D}{\partial h} - D\frac{\ln(F)}{l^2} \exp\left(\frac{h}{l}\right) C \quad (2)$$

$$\text{with } D(h) = D_l \left\{ \left(\frac{D_s}{D_l} \right)^{\exp\left(\frac{h}{ml}\right)} \right\} \quad (3)$$

where C is the relative *Tr* concentration (normalized to that in the bulk mineral assuming an equilibrium between aqueous and solid solution), t is the time, h is the mineral depth (from 0 at the surface, to negative values toward the bulk), D_l is the lattice diffusion coefficient, D_s is the surface diffusivity, V is the linear growth rate, F is the relative surface enrichment factor ($= \Delta_{Tr,Hc,ads} / \Delta_{Tr,Hc,eq}$), l is the half-thickness of the surface enriched layer, and m is the multiplier linking l to the maximal thickness of the diffusivity region. Equations (2) and (3) can be solved by a Qbasic reactive-transport code (courtesy of *E.B.Watson*). The code calculates the relative trace-element concentration profile as a function of the depth from the mineral surface at a given time point.

A limitation of SEMO is that the variation of aqueous solution composition and speciation is not accounted for (e.g. V is considered by SEMO as a constant). However, embedding SEMO into a geochemical modeling code that can be run sequentially in reaction-path calculations could circumvent this limitation. Another important limitation is that some parameters are not measurable and must be fitted by the inverse modeling (e.g. D_s, l, m).

1.3 Surface Reaction Kinetics Model (SRKM)

The Surface Reaction Kinetics Model **(*DePaolo (2011)*)** is based on the concept of dynamic precipitation-dissolution close to equilibrium. The model was originally developed to interpret the fractionation of calcium isotopes in calcite, and later on adapted to describe Sr incorporation in calcite. The Mesoscopic Kinetic Theory **(*Grmela and Laidlaw (1983)*)** states that mineral-aqueous equilibrium is a dynamic process, in which precipitation and dissolution rates are equal and compensate each other. In aqueous medium, any mineral is affected by simultaneous dissolution and precipitation, which can be parameterized by a "gross forward precipitation rate" R_f (related to a kinetic rate constant k_f), and a "gross backward dissolution rate" R_b (related to a kinetic constant k_b). The net (macroscopic) precipitation rate R_p is the difference between R_f and R_b. At equilibrium, R_b is exactly balanced by R_f so that R_p=0.

Using relations between forward rates and kinetic rate constants, and considering that the amount of *Tr* is negligible compared to the amount of *Hc*, one can obtain the model equation:

$$\Delta_{Tr,Hc} = \frac{\alpha_f}{1 + \frac{R_b}{R_b + R_p}\left(\frac{\alpha_f}{\alpha_{eq}} - 1\right)} \quad (4)$$

where R_b and R_p are rates related to the *Hc*, α_f is the fractionation coefficient due to the gross forward precipitation rate (maximum fractionation coefficient), and α_{eq} is the fractionation coefficient at equilibrium. Note that if R_p=0, $\Delta_{Tr,Hc}=\alpha_{eq}$; if R_p is high, $\Delta_{Tr,Hc}$ tends toward α_f. There is a growth rate dependency that is qualitatively similar to that produced in the SEMO.

The main advantage of SRKM is that because (4) is rather simple, $\Delta_{Tr,Hc}$ can be calculated without a sophisticated computer code. The depletion of *Tr* in aqueous solution can be accounted for sequentially, by considering at each step the growth of a next thin layer. There are nevertheless open questions; for instance, is the concept of gross backward rate R_b physically realistic? There is also no consensus in the literature about how to obtain a proper value of rate *Rb*.

1.4 Adsorption-Diffusion-Desorption Model (ADDM)

This model was originally proposed by ***Barrow* (*1983*)** to describe sorption and desorption of phosphate by soils. It was later improved in ***Barrow and Bowden* (*1987*)**. In the present context, the main assumption of ADDM is that the adsorption or desorption of *Tr* creates a diffusion gradient for sorbed *Tr* to/from the mineral interior. This model does not account for precipitation or dissolution of the host mineral. The ADDM consists of two parts: adsorption and in-diffusion. At present, the adsorption model part is no longer of interest because several well-developed surface complexation models are available, supported by computer codes (see overview in ***Kulik (2009)***).

In the ADDM model, the increase of the *Tr* surface activity triggers a diffusion gradient. But, contrary to the SEMO model, it excludes mineral growth and thus excludes any macroscopic mass transfer under such conditions. This is the main difference to SEMO, which assumes a non-zero mineral growth rate. According to ***Crank* (*1964*)**, the amount of material transferred to the interior of the mineral (mol/m^2) as function of time and considering a semi-infinite medium is:

$$n(t) = 2C_{Tr,s}\sqrt{D_k f t / \pi} \quad (5)$$

where $C_{Tr,s}$ is the concentration of *Tr* at the surface of the mineral assumed to be constant (at constant composition of aqueous solution) in mol/m^2, D_k is a coefficient (time^{-1}) (a diffusion coefficient divided by the square of the adsorbed layer thickness), *t* is the time, and $f = 1/(1-\theta)$ is close to 1 in trace concentration region. Here, θ is the mole fraction of adsorbed *Tr* at the

surface. In reality, the surface concentration of *Tr* is not necessarily constant due to possible changes in the aqueous phase composition during the reaction progress; thus, eq (5) needs to be integrated over sufficiently small time steps.

The ADDM allows explaining the frequently observed hysteresis between adsorption and desorption steps. This hysteresis means that the previously sorbed *Tr* amount is not fully desorbed after a certain ageing time. For instance, it was observed and successfully modeled that the longer the ageing time the more pronounced the hysteresis for phosphates on soils **(*Barrow (1983)*)** and for Zn on goethite **(*Barrow et al. (1989)*)**. ***Strauss et al.* (*1997*)** observed that the sorption of phosphate, and the hysteresis increases with the specific surface area of goethite. This kind of retention is explained in ADDM by the in-diffusion –like phenomena of adsorbed *Tr* on the rough mineral surface.

Compared to the other two models, the limitation of the ADDM is that the growth of the mineral is not considered. In addition, the diffusion is only allowed into the bulk mineral. In contrast, the SEMO considers diffusion both into and out of the mineral, whereas the SRKM does not explicitly consider diffusion processes. Nevertheless, the in/out diffusion effects at zero growth may be very relevant for the long-term processes considered in the SKIN context; therefore, they cannot be ignored. This is a matter of further investigations.

1.5 Gibbs Energy Minimization (GEM)

GEM is a procedure that finds equilibrium phase assemblage and speciation in a chemical system (GEM primal solution) defined by *T, P*, bulk composition, standard molar Gibbs energies of all components in all phases g^o, and parameters of mixing and non-ideality in solution phases. Simultaneously, GEM calculates the chemical potentials of elements and charge (the dual solution, ***Kulik et al. (2013)***, http://gems.web.psi.ch). Mathematically, GEM minimizes the total Gibbs energy of the system computed from species amounts and chemical potentials.

2. The unified model

2.1 Model comparison

Comparative modelling exercises were performed for Sr and Cd uptake in calcite at 25°C, the systems where the most experimental data were available. Comparing SEMO and SRKM implies to make a hypothesis that $\Delta_{Tr,Hc,eq} = \alpha_{eq}$ and $\Delta_{Tr,Hc,sorp} = F \cdot \Delta_{Tr,Hc,eq} = \alpha_f$, which is quite reasonable. Because there is a lack of R_b and D_s values in the literature, we tried different values in order to obtain the best fit at various experimental conditions.

As seen on Figure 52, both SEMO and SRKM predict similar trends and describe qualitatively the experimental results, although the slopes of data and model curves do not coincide. Significant deviations between the data and the model curves are observed, in particular, for the data of ***Tesoriero and Pankow* (*1996*)**. Obtaining the modelling parameters from experimental data seems to be more difficult for Cd than for Sr. This example highlights that the implementation of uptake kinetics models in a geochemical code is necessary.

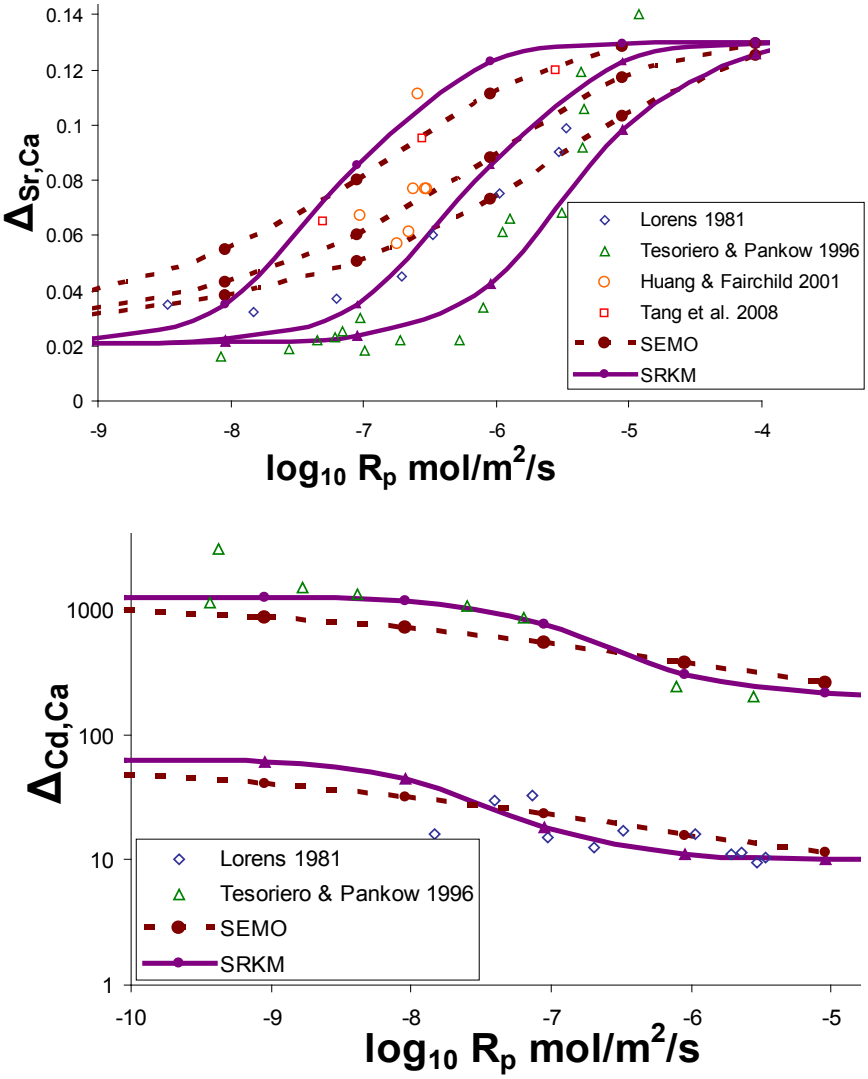

Figure 52: *Fractionation coefficients of Sr and Cd in calcite as a function of growth rate. Comparison between SEMO and SRKM vs selected experimental data. Modelling parameters are given in Table 18.*

Table 18: *Parameters of the unified model related to Figure 52.*

Element	$\Delta_{Tr,Ca,eq}$	F	m	l (nm)	D_s (nm^2/s)*	R_b (mol/m^2/s)*
Sr	0.021	6.2	6	0.5	0.01; 0.06; 0.2	$5\cdot10^{-9}$; $1\cdot10^{-7}$; $6\cdot10^{-7}$
Cd ***(Lorens, 1981)***	63	0.16	6	0.5	0.06	$1\cdot10^{-7}$
Cd ***(Tesoriero and Pankow, 1996)***	1240	0.16	6	0.5	0.2	$6\cdot10^{-7}$

* From left to right.

2.2 Merging the models

The experimental data can be modelled reasonably well with either SEMO or SRKM. The common outcome from both models is that the fractionation coefficient $\Delta_{Tr,Ca}$ varies between two limits, $\Delta_{Tr,Ca,eq}$ and $\Delta_{Tr,Ca,ads} = F\cdot\Delta_{Tr,Ca,eq}$. This suggests that SRKM might be considered as an integrated form of SEMO (which is a reactive transport model), and raises the question whether the two uptake models could be merged into a generalized one, allegedly having the physics of SEMO and the simplicity of the SRKM.

In both concepts, high precipitation rates constrain the composition of the newly grown incremental layer, with *Tr* content greater than expected from Aq-SS equilibrium if *Tr* is incompatible (i.e. hardly accommodates) with the host mineral structure ($F > 1$), and less than that ($F < 1$), if *Tr* is compatible (i.e. it easily fits into the host mineral lattice). In both models, this enrichment or depletion can be counterbalanced by a release of entrapped *Tr* back to aqueous solution. This release is assigned to a dissolution phenomenon in SRKM and to an out diffusion phenomenon in SEMO, although it must not necessarily be regarded as a "true" diffusion. Regarding this, we assumed that D_s in SEMO is equivalent to R_b in SRKM. Thus, we propose to introduce in SEMO a new quantity V_b (in m/s), which can be regarded as a 1-D analogue of the surface diffusivity:

$$V_b = \frac{D_s}{ml} \tag{6}$$

Considering that the same phenomenon triggers D_s and R_b, we further assume:

$$\frac{R_b}{R_p} = \frac{V_b}{V} \tag{7}$$

By combining eq (4) with eqs (6-7), one obtains ***(Thien et al. (2012))***:

$$\Delta_{Tr,Hc} = \frac{F \cdot \Delta_{Tr,Hc,eq}}{1 + \frac{\left(\frac{D_s}{ml}\right)}{\left(\frac{D_s}{ml}\right) + V}(F-1)} \tag{8}$$

This equation has a mathematical form similar to eq (4), yielding a very similar curve shape. A limitation of this merged model is that the lattice diffusion (present in SEMO and, as in-diffusion parameter, in the ADDM) is not accounted for, although at very long reaction time, the effect of lattice diffusion may be significant. Further improvement of the merged model should account for the in-diffusion phenomenon (see Section 1.4).

2.3 Current implementation in GEM-Selektor

The 'merged' model equation was provisionally implemented as a script in the GEM-Selektor "process simulator" module. In such simulations, the time evolution of a geochemical thermodynamic system can be represented as a sequence of partial equilibrium states. In a partial equilibrium system, at least one phase is kept out of equilibrium with the rest of the system by the additional "metastability constraints" ***(Karpov et al. (2001), Kulik et al. (2012))***. For instance, precipitation of calcite can be simulated over time steps as a sequence of partial equilibrium states controlled according to a kinetic rate law (e.g. ***Wolthers et al. (2012)***) that includes the saturation index and the evolving surface area of the mineral.

Because the fractionation of *Tr* depends on the host mineral growth rate, it becomes possible to calculate $\Delta_{Tr,Hc}$ and thus control the metastable amount of trace end member ($SrCO_3$) from the current aqueous speciation and the increment of mole amount of the host end member (calcite) at a given time step.

3. Modelling trace element content in growing calcite

3.1 Modeling examples

The merged uptake model implemented in GEM-Selektor was tested against experimental data on Sr, Cd, Co, Mn co-precipitation with calcite from ***Lorens (1981)***. Figure 53 shows that our model is able to describe satisfactorily the growth-rate dependency of the measured

$\Delta_{Tr,Hc}$. The parameters F, D_s, and ml were taken from literature, whereas $\Delta_{Tr,Hc,eq}$ is calculated from a solid-solution model (e.g. ***Kulik et al. (2000), Kulik et al. (2010)***).

3.2 Solution depletion effects

We extended the simulation time of the previously modeled systems to 10^5 s in order to reach significant depletion of *Tr* in the aqueous solution and assess the effects of long reaction times on trace element partitioning. The depletion is likely to decrease the host mineral precipitation rate. This will consequently reduce $\Delta_{Tr,Hc}$ for incompatible elements, and increase $\Delta_{Tr,Hc}$ for compatible elements. These effects are shown on Figure 54. In addition, we can see that the higher the initial growth rate is, the more the depletion effects are important.

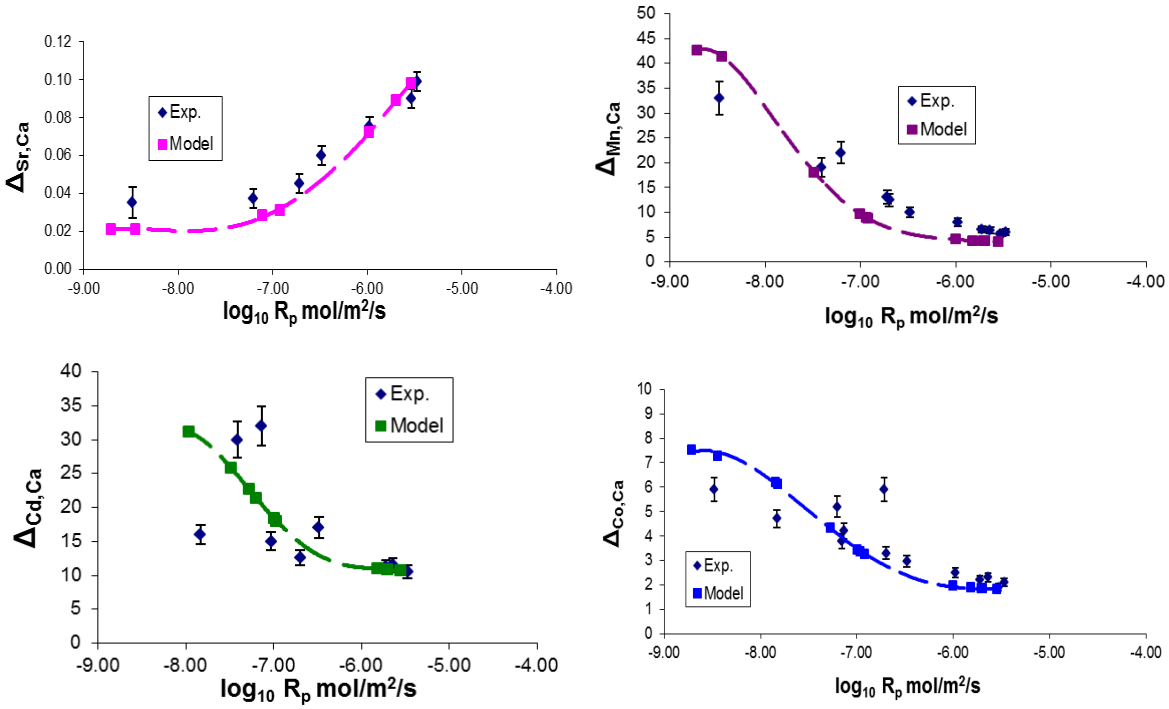

Figure 53: *Fractionation coefficient as a function of growth rate for Sr, Cd, Co, and Mn in calcite. F=6.2, 0.3, 0.22, 0.9 (from Sr to Mn); D_s=0.06 nm^2/s, l=0.5nm, m=6 for all cases. $\Delta_{Tr,ca,eq}$ curves were calculated in GEM-Selektor.*

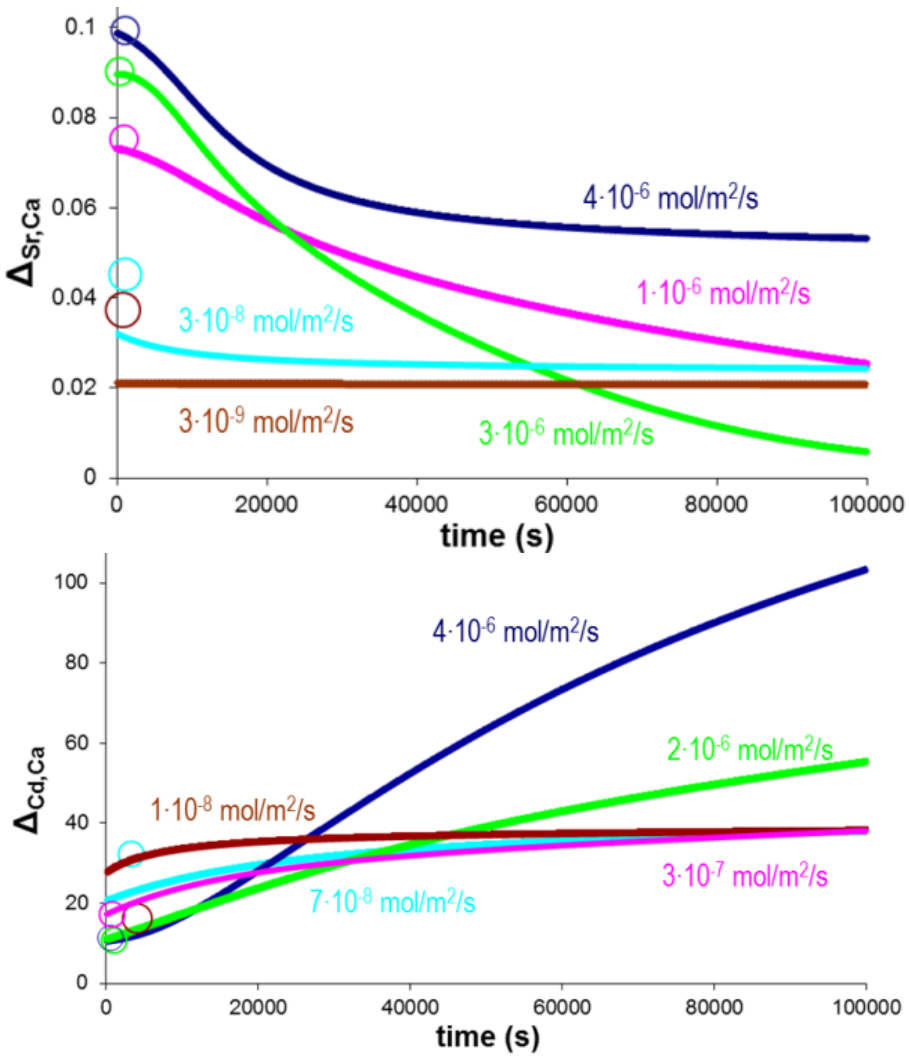

Figure 54: *Hypothetical* $\Delta_{Tr,Hc}$ *variations as function of time for the calcite-"strontianite" (a) and calcite-otavite (b) systems. Circles correspond to the experimental results shown in Figure 53.*

Interaction with experimentalists

The unified uptake model implemented in GEM-Selektor v.3 code was tested against experimental data on Sr, Cd, Co, Mn coprecipitation with calcite in section 3. Although we would like to test our model for other *Tr*/*Hc* pairs of interest, frequently the necessary experimental values of $\Delta_{Tr,Hc}$ as a function of growth or recrystallization rate are not known. Trace elements and solids of interest are for instance lanthanides/actinides in HFO, clays, and

C-S-H; Ra/Cs(K)/Mn in barite, celestite, goethite, and C-S-H; U/Ni/Mn/Cs(K) in calcite or aragonite.

Moreover, the fact that a model describes faithfully experimental data does not mean that this model is physically realistic and that the mechanisms implied by the model are real. Therefore, microscopic and/or spectroscopic data (e.g. surface dynamics by AFM, binding of *Tr* via XPS, GIXAFS) would also be welcome to identify the relevant growth and binding mechanisms.

In the same way that experimentalists could help us, we could help them. Our model may be useful to plan experiments and to optimize parameters. It also can be used to interpret results in terms of thermodynamics and kinetics. The ultimate goal is the application to performance-assessment scenarios.

Conclusions and future work

Two existing uptake kinetic models were merged into a 'generalized' one suitable for implementation in a geochemical modelling code. This model can be used to describe trace element uptake during mineral growth in aqueous solutions with changing composition, provided that a few parameters specific to trace element/host mineral combinations are known. This model could be useful for understanding long-term systems with high solid/water ratio, which are likely to be affected by solution depletion effects. The effect of specific surface area or surface roughness on the sub-surface diffusivity parameter seems to be significant, and requires further investigations. Possible in-diffusion phenomena must also be accounted for. We plan to 'hard-code' this unified model to make it usable in geochemical reactive-transport codes coupled with the GEMS3K kernel (***Kulik et al. (2013)***) of GEM-Selektor package.

Acknowledgements

The research leading to these results has received funding from the European Union's European Atomic Energy Community's (Euratom) Seventh Framework Programme FP7/2007-2011 under grant agreement n° 295722 (SKIN project). We would like to thank E.B. Watson for providing his SEMO code.

References

Barrow, N. J. (1983). A mechanistic model for describing the sorption and desorption of phosphate by soils. Journal of Soil Science 34, 733-750.

Barrow, N. J. and Bowden, J. W. (1987). A comparison of models for describing the adsorption of anions on a variable charge mineral surface. Journal of Colloid and Interface Science 119, 236-250.

Barrow, N. J., Gerth, J., and Brummer, G. W. (1989). Reaction-kinetics of the adsorption and desorption of nickel , zinc and cadmium bu goethite .2. Modeling the extent and rate of reaction. Journal of Soil Science 40, 437-450.

Crank, J., (1964). The Mathematics of Diffusion. Oxford University Press, Oxford.

DePaolo, D. J. (2011). Surface kinetic model for isotopic and trace element fractionation during precipitation of calcite from aqueous solutions. Geochimica et Cosmochimica Acta 75, 1039-1056.

Grmela, M. and Laidlaw, W. (1983). Mesoscopic kinetic theory. Journal of. Chem. Phys. 78, 5151.

Huang, Y. and Fairchild, I. J. (2001). Partitioning of Sr^{2+} and Mg^{2+} into calcite under karst-analogue experimental conditions. Geochimica et Cosmochimica Acta 65, 47-62.

Karpov, I.K., Chudnenko, K.V., Kulik, D.A., Avchenko, O.V. and Bychinsky, V.A. (2001). Minimization of Gibbs free energy in geochemical systems by convex programming. Geochemistry International 39(11), 1108-1119.

Kulik, D.A., Kersten, M., Heiser, U., and Neumann, T. (2000). Application of Gibbs energy minimization to model early-diagenetic solid-solution aqueous-solution equilibria involving authigenic rhodochrosites in anoxic Baltic sea sediments. Aquatic Geochemistry 6, 147-199.

Kulik, D.A. (2009): Thermodynamic concepts in modeling sorption at the mineral-water interface. In: Thermodynamics and Kinetics of Water-Rock Interactions (Eds. E.H.Oelkers, J.Schott), Reviews in Mineralogy and Geochemistry 70, 125-180.

Kulik, D.A., Thien, B., and Curti, E. (2012). Partial-equilibrium concepts to model trace element uptake. Mineralogical Magazine 75, 1959.

Kulik, D.A., Wagner, T., Dmytrieva, S.V., Kosakowski, G., Hingerl, F.F., Chudnenko, K.V., and Berner U. (2013). GEM-Selektor geochemical modeling package: Numerical kernel GEMS3K for coupled simulation codes. Computational Geosciences 17, 1-24.

Lorens, R. B. (1981). Sr, Cd, Mn and Co distribution coefficients in calcite as a function of calcite precipitation rate. Geochimica et Cosmochimica Acta 45, 553-561.

Strauss, R., Brummer, G. W., and Barrow, N. J. (1997). Effects of crystallinity of goethite .2. Rates of sorption and desorption of phosphate. Eur. J. Soil Sci. 48, 101-114.

Tang, J., Köhler, S. J., and Dietzel, M. (2008). Sr^{2+}/Ca^{2+} and $^{44}Ca/^{40}Ca$ fractionation during inorganic calcite formation: I. Sr incorporation. Geochimica et Cosmochimica Acta 72, 3718-3732.

Tesoriero, A. J. and Pankow, J. F. (1996). Solid solution partitioning of Sr^{2+}, Ba^{2+}, and Cd^{2+} to calcite. Geochimica et Cosmochimica Acta 60, 1053-1063.

Thien, B., Kulik, D.A., and Curti, E. (2012). Adding uptake kinetics and surface entrapment to geochemical models. Mineralogical Magazine 75, 2452.

Watson, E. B. (2004). A conceptual model for near-surface kinetic controls on the trace-element and stable isotope composition of abiogenic calcite crystals. Geochimica et Cosmochimica Acta 68, 1473-1488.

Watson, E. B. and Liang, Y. (1995). A simple model for sector zoning in slowly grown crystals; implications for growth rate and lattice diffusion, with emphasis on accessory minerals in crustal rocks. American Mineralogist 80, 1179-1187.

Wolthers, M., Nehrke, G., Gustafsson, J. P., and Van Cappellen, P. (2012). Calcite growth kinetics: Modeling the effect of solution stoichiometry. Geochimica et Cosmochimica Acta 77, 121-134.

SOLID SOLUTION THERMODYNAMICS

Enzo Curti[1,*]

[1] Paul Scherrer Institut (Switzerland)

* Corresponding author: enzo.curti@psi.ch

Abstract

This contribution presents the progress made in this task until November 2012. The experimental data produced at FZJ on Ra uptake during the recrystallization of two commercial barites (Sachtleben and Aldrich) were modelled using a combined kinetic and thermodynamic approach. The evaluation of the available data shows that after a first kinetic step (120-180 days) with growth rates similar to those observed in previous published experiments, the growth rate suddenly increases to values of up to 400 μm $m^{-2}d^{-1}$. This two-step kinetics suggests the sudden nucleation of a new Ra-barite phase from supersaturation after an initial phase of slower recrystallization under close-to-equilibrium conditions. In contrast to previously published experiments, the data indicate formation of solid solutions close to ideality or even with negative interaction parameters. In order to reduce uncertainties in the modelling, a review of published data on the solubility product of $RaSO_4$ has been carried out. The review shows that the currently used value is sufficiently precise and accurate ($\log K^0_{sp}$= -10.26 ± 0.1).

Background and objectives

It is well known that the formation of dilute solid solutions leads to a decrease in the solubility of the minor component. This effect could be particularly beneficial to the safety of nuclear waste sites whenever safety-relevant nuclides released from radioactive waste form solid solutions with host minerals residing in the near-field of such repositories. Under such circumstances, radionuclide solubility is strongly reduced compared to solubility control by pure solids. In the case of radium, formation of solid solutions with barite, $(Ra,Ba)SO_4$, by reaction of sulphate solutions with Ba isotopes from the waste is considered to be likely. This process would reduce the concentration and thus the mobility of dissolved radium by orders of magnitude compared to the case of solubility controlled by pure radium sulphate. Eventually, the ^{226}Ra contribution to radiological doses would decrease to levels largely below those predicted assuming that a pure solid (e.g. $RaSO_4$) controls Ra solubility.

A thorough understanding of the mechanisms leading to Ra-barite formation and the careful quantification of related thermodynamic data (non-ideality parameters, end-member solubility products) is a prerequisite to reliably predict the contribution of ^{226}Ra to radiological doses in safety assessments calculations. In this work package, the main objectives are: (1) to model experimental data provided by other SKIN partners on the uptake of Ra during barite recrystallization in terms of solid solution thermodynamics (determination of interaction parameters) and kinetics (growth rates of radiobarites); (2) to review available data on $RaSO_4$ solubility product, in order to verify the reliability of the values currently used in thermodynamic databases.

Modelling of FZJ data

Extensive Ra uptake experiments were and are being carried out at FZJ. In these experiments, conducted at room temperature (RT) and 90 ^{0}C, two commercial barite powders (Sachtleben® and Aldrich®) were aged in 0.1 M NaCl + 5 μM $RaBr_2$ solutions during more than 200 days. The dissolved Ra concentration was measured by gamma spectrometry at regular intervals.

The data of two representative experiments carried out at RT with the two barites under identical conditions are illustrated in Figure 55 together with several model curves. Continuous lines represent ideal solid solutions, whereas broken lines represent non-ideal solid solutions with the non-ideality parameters set to $a_0 = 1.0$ and $a_0 = -0.8$, respectively.

The Ra concentration data were fitted using the following two-step procedure:

(a) Calculation with the GEM-Selektor (GEMS) code of a series of equilibrium states as a function of the increasing amount (n) of $(Ra,Ba)SO_4$. This yields the equilibrium Ra concentrations as a function of n up to the total amount of barite used in the experiments and for the selected solid solution model (ideal or non-ideal).

(b) Determination of the reaction time t as a function of n, the initial specific surface area σ (m^2/g), the solution volume V (L), the particle concentration S/L (g/L) and a recrystallization rate R (mol m^{-2} d^{-1}) normalized to the initial mineral surface:

$$t = \frac{n}{\sigma V (S/L) R}$$

For each value of n calculated with GEMS, a reaction time can be determined from the equation above. Because the GEMS calculations include the concentrations of Ra at equilibrium with the selected solid solution, each $t(n)$ value can be readily associated to the corresponding equilibrium Ra concentration, [Ra](n). Since there is no independent

determination of the recrystallization rate in these experiments, *R* was used as adjustable parameter to fit the Ra concentration data.

The comparison of data and model curves in Figure 55 shows the following features:

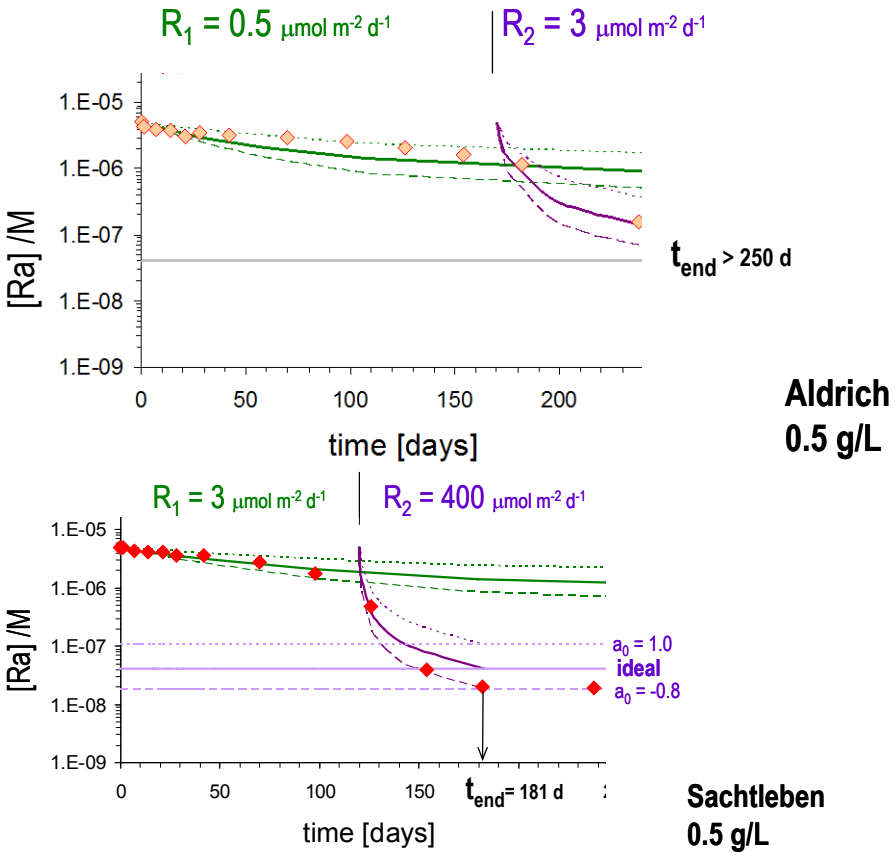

Figure 55: *Experimentally determined Ra concentrations for typical barite recrystallization tests conducted at FZJ at room temperature and 0.5 g/L. The data are compared with modelling curves and can be explained by two-steps kinetics (see text for explanation).*

(a) In both cases two kinetic rates (R_1 and R_2) are required to fit the experimentally determined Ra concentrations: after a first period (120-180 days) of slow recrystallization, the growth of Ra-barite suddenly accelerates by 1-2 orders of magnitudes. The very high value inferred for the second step in the experiment carried out with Sachtleben barite (400 µmol m^{-2} d^{-1}) can hardly represent a recrystallization reaction and rather points to sudden nucleation of a new Ra-barite phase from supersaturation.

(b) The growth rates of Sachtleben Ra-barite appear to be considerably faster than for Aldrich barite. This result is at first sight surprising. However, one should realize that because the rates are normalised to the initial surface area, our model is insensitive to possible variations of this parameter. Indeed, SEM images reveal that the fine-grained Aldrich barite (1.7 m^2 g^{-1}) undergoes substantial coarsening during the recrystallization reaction (*Brandt*, pers. comm.), while such effects were not observed for Sachtleben barite (0.17 m^2 g^{-1}). Taking into account the surface area reduction of Aldrich barite would lead to higher recrystallization rates, i.e. shift the calculated rates towards the values determined for the tests with Sachtleben barite.

(c) Our modelling results point to formation of an ideal solid solution (Aldrich) or even a non-ideal solid solution with negative enthalpy of mixing (Sachtleben). This latter result is not consistent with the findings of earlier experiments described by ***Curti et al.* (*2010*)** and ***Bosbach et al.* (*2010*)**, who indicate (Ra,Ba)SO_4 solid solutions with positive Guggenheim parameters.

Re-evaluation of $RaSO_4$ solubility product

The solubility product of pure $RaSO_4$ was measured in two independent investigations by ***Lind et al.* (*1918*)**, and by ***Nikitin and Tolmatscheff* (*1933*)**. In both studies, the so-called *emanation method* was used, based on scintillation counting of gaseous ^{222}Rn produced by ^{226}Ra.

***Lind et al.* (*1918*)** carried out their solubility measurements both from undersaturation (dissolution) and supersaturation (precipitation). Four determinations at 25^0C were conducted in sulfuric acid (0.01 M or 0.1 M). The average of these determinations consistently yields $\log K^0_{sp}$ of -10.25 +/- 0.07, a value very close to that used in our calculations (-10.26) based on the thermodynamic data compiled in the Nagra/PSI database **(*Hummel et al., 2002*)**. However, the solubility product measured in pure water was about two orders of magnitude lower than in sulphuric acid, whereas in 0.1 M Na_2SO_4 it was about one order of magnitude higher.

***Nikitin and Tolmatscheff* (*1933*)** noted that ***Lind et al.* (*1918*)** did not take properly into account the effects of Ra sorption on filter and glassware, suggesting that they anomalous results may derive from such artefacts. In their study, ***Nikitin and Tolmatscheff* (*1933*)** took great care to correct for Ra losses in the filter, glassware, emanation apparatus and even in the pipette used to sample the solutions. The technique used was to sample successive aliquots of aqueous solution equilibrated with $RaSO_4$ and measure the Ra concentration for each aliquot until Ra sorption on filter and pipette was found to have reached equilibrium (i.e., the solution analyses yielded constant, asymptotic values). The results obtained were quite consistent, independently of the technique used to separate the aqueous phase from the solid (filtration or

centrifugation). From their data, we calculate $\log K^0_{sp}$ = -10.41 ± 0.10 at 20 ^{0}C and -10.29 ± 0.10 after extrapolation to 25^{0}C using Van't Hoff equation and $\Delta_r H^0$(diss.) = 9.3 kcal/mol given by ***Langmuir and Riese* (*1985*)**. We obtained identical values using either Davies or Debye-Hückel approximation.

Our extrapolation to zero ionic strength of the original data (at 20 ^{0}C), yields a somewhat lower solubility product and is statistically less accurate than the values given by ***Nikitin and Tolmatscheff* (*1933*)** (-10.37 ± 0.02) obtained using the activity coefficients tabulated by ***Lewis and Randall* (*1927*)**. These authors give a generic value (applying to all divalent cations) for the activity coefficient of Ra^{2+}. Although it is quite surprising that Lewis and Randall's method performs better than more modern methods of ionic strength corrections, one has to acknowledge this as a fact. However, both methods yield almost equivalent results for the value of the $RaSO_4$ solubility product, and we see no need for a modification of the value used so far ($\log K^0_{sp}$ = -10.26). This result reasonably agrees with the evaluation of the same data made by ***Paige et al.* (*1998*)**, who obtained $\log K^0_{sp}$(25 ^{0}C) = -10.21 ± 0.06 using the Pitzer model.

Taking into account the new evaluations, one can now assign an uncertainty range of ± 0.1 logK units to the solubility product of $RaSO_4$. Using the temperature dependence equation of ***Langmuir and Riese* (*1985*)** one then derives $\log K^0_{sp}$ = -10.4 ± 0.1 for experiments carried out in a laboratory environment thermostated at 20 ^{0}C. This puts a lower solubility limit at $\log K^0_{sp}$= -10.5 for the experiments carried out at FZJ, which could help explaining the low Ra concentrations found in some experiments (leading to negative interaction coefficients when using $\log K^0_{sp}$= -10.26).

References

Bosbach D., Böttle M. and Metz V. (2010). Experimental study on Ra^{2+} uptake by barite ($BaSO_4$). Technical Report TR-10-43, Swedish Nuclear Fuel and Waste Management Co (SKB), Stockholm, Sweden.

Curti E., Fujiwara K. et al. (2010). Radium uptake during barite recrystallization at 23 ± 2 ^{o}C as a function of solution composition: An experimental ^{133}Ba and ^{226}Ra tracer study. Geochim. Cosmochim. Acta 74, 3553-3570.

Hummel W., Berner U., Curti E., Pearson F. J., and Thoenen T. (2002) Nagra/PSI Chemical. Thermodynamic Data Base 01/01. Nagra Technical Report NTB 02-16, Nagra, Wettingen, Switzerland and Universal Publishers/uPublish.com, Parkland,Florida, ISBN 1–58112–620–624.

Langmuir D., Riese A.C. (1985). The thermodynamic properties of radium. Geochim. Cosmochim. Acta 49, 1593-1601.

Lewis G.N., Randall M. (1927). Thermodynamik und die Freie Energie Chemischer Substanzen. Wien, J. Springer, 1927.

Lind S.C., Underwood J.E. and Whittemore C.F. (1918). The solubility of pure radium sulfate. J. Am. Chem. Vol. XL, No. 3, 465-472.

Nikitin B. and Tomatscheff P. (1933). Ein Beitrag zur Gültigkeit des Massenwirkungsgesetzes II. Quantitative Bestimmung der Löslichkeit des Radiumsulfats in Natriumsulfatlösungen und in Wasser. Zeitschrift für Physikalische Chemie, A167, 260-272.

POSTER

Slow processes in close-to-equilibrium conditions for radionuclides in water/solid systems of relevance to nuclear waste management

A 7th FRAMEWORK PROGRAMME COLLABORATIVE PROJECT (2008-2012)

Pr. Bernd Grambow, Coordinator
Subatech Laboratory, 4 rue Alfred Kastler, 44307 Nantes, France; grambow@subatech.in2p3.fr

Presentation

SKIN is a 3-years collaborative project focused on the study of very slow processes that can impact on the mobility behaviour of radionuclides from the source term, the near field and the geosphere

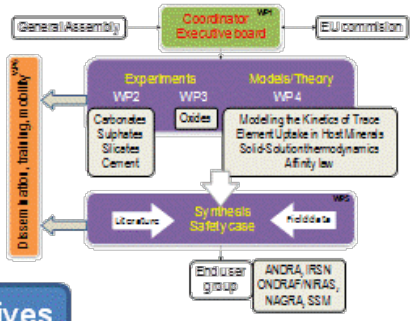

Partners

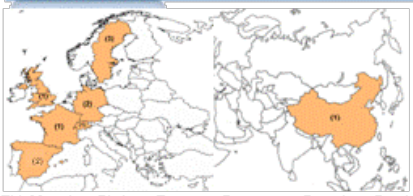

5 EU Member States: France, Germany, Sweden, Spain, United Kingdom
1 Associated Country: Switzerland
1 Other Country: China
1 associate group: Spain
End user group : ANDRA, ONDRAF/NIRAS, NAGRA, SSM and IRSN

Objectives

- **To assess** the use/misuse of solubility data of sparingly soluble tetravalent actinides
- **To understand** the coupling of major and trace element chemistry in RN migration behavior considering the extremely large exchange pool of natural minerals present in the disposal sites
- **To include** irreversibility in models on the mobility of RN in the repository environment
- **To assess**, in PA to what degree the ignorance/non-inclusion of these studied slow processes leads to over-conservative evaluations, or in few cases, even too optimistic evaluations

Compartmental modelling approach

Irreversible processes

New solubility
Sorption data

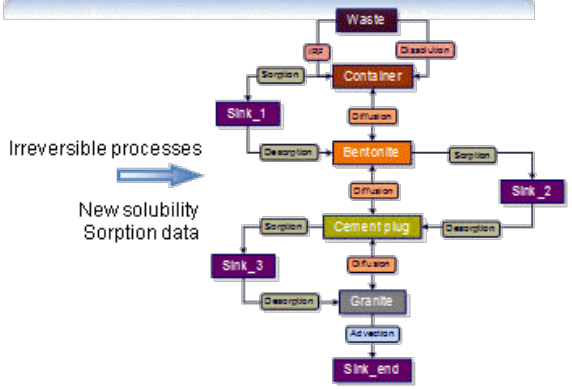

Determining the impact of the studies done in the frame of the SKIN project over the calculations that support safety assessment procedures.

Programme structure and Activities

- *Identification of*
  - the substitution scheme for complex metal ion substitutions
  - ion binding (precipitation, co-precipitation, surface uptake) in complex cement related systems
- *Questions of reversibility*
  - solid/solution interaction with clays
- *Assessment of*
  - the kinetics of dissolution of tetravalent oxides under quasi-equilibrium conditions
  - the impact of major systems present in the repository environment on the rate of dissolution of matrix-related material and retention/release of radionuclides.

Present status

Start of the project: January 1st, 2011
Kick-Off Meeting: February 1st, 2011, France
1st annual workshop: November 17th-18th, 2011, AMPHOS 21
2nd annual workshop: November 21th-22th, 2012, PSI
1st Proceeding: http://www.emn.fr/z-subatech/skin
Publication: Holliday et al. Dalton Trans., 2012, 41, 3642-3647
Participation to conferences: NUWCEM'11, Migration'11, Goldschmidt'12

Jül-4364
Juli 2013
ISSN 0944-2952